



**UNIVERSITÀ
DEGLI STUDI
DI TRIESTE**

**UNIVERSITÀ DEGLI STUDI DI TRIESTE
XXXIV CICLO DEL DOTTORATO DI RICERCA IN
NANOTECNOLOGIE**

Borsa MIUR/Ateneo cofinanziata dal Dipartimento di Fisica su fondi CNR-IOM

**Nanomechanical structures for the detection
of living cells**

Settore scientifico-disciplinare: **FIS/03**

DOTTORANDA

Martina Conti

COORDINATORE

PROF. Alberto Morgante

SUPERVISORE DI TESI

DOTT. Marco Lazzarino

CORRELATORI

DOTT.ssa Laura Andolfi

DOTT. Simone Dal Zilio

ANNO ACCADEMICO 2020/2021

Table of Contents

Acknowledgments	1
Abstract	3
Introduction	5
Cell migration and cancer: a physical perspective	7
1.1. Cell migration	7
1.2. The role of forces in cell migration	9
1.3. Cancer cell migration and invasion	12
1.4. The role of forces in cancer cell migration	14
1.5. Dimensionality in cell migration	18
1.5.1. Investigation of the effect of topography on cell migration	23
Chapter 2	26
Cell migration assays on 2D and 3D platforms	26
2. Introduction	26
2.1. Two-dimensional (2D) assays to study single cell migration	27
2.1.1. Wound-healing assay	27
2.1.2. Single cell motility assay	28
2.1.3. 2D cell tracking assay	29
2.2. Three-dimensional (3D) assays to study cell migration	30
2.2.1. Three-dimensional matrix invasion assays	31
2.2.2. Spheroid migration assay	32
2.2.3. Trans-well migration assay	32
2.2.4. 3D cell tracking assay	33
Chapter 3	34
The investigation of forces in cell biology	34
3. Introduction	34
3.1 Assays for the study of forces	35
3.1.1. Traction force microscopy	35
3.1.2. Micropatterned substrates-based TFM	36
3.1.3. Molecular sensors	37
3.2. Mechanical biosensors	39

3.3. Cantilever-based micro- and nanomechanical sensors	42
3.4. Materials and manufacturing processes	44
3.4.1. Silicon-based cantilevers	44
3.4.2. Polymeric-based cantilever	45
3.5. Operation modes of nanomechanical biosensors: static and dynamic mode	46
3.6. Actuation of cantilever-based sensors	50
3.7. Read-out principles	51
3.8. Functionalization processes for biological purposes	53
3.9. Real-time and end-point assay detection for biosensing	55
3.10. Nanomechanical sensors for biological detection	57
3.11. Challenges in the use of nanomechanical sensor for biological application	59
3.12. Nanomechanical sensors to detect forces exerted by cells	62
Chapter 4	65
Half-wet nanomechanical biosensors to investigate cancer cells adhesion and migration dynamic	65
3. Introduction	65
4.1. Design of HWN sensors	67
4.2. Fabrication of HWN cantilevers	68
4.3. Development of a chamber of measurements for HWN sensors ..	71
4.4. Nanomechanical characterization of HWN sensors	72
4.5. Application of the HWN sensors to the detection of cancer cells ..	77
4.5.1. Cantilever functionalization	77
4.5.2. Cell lines and cell cultures	81
4.5.3. Experimental setup for living cells analysis	82
4.5.4. Mass measurements of living cells on HWN sensors	84
4.5.5. HWN sensor to investigate cancer cell motility and exerted forces	85
4.5.6. Analysis of the variance as a function of cell position along the cantilever	91
4.5.7. Macro- and micro-oscillation analysis	94

Chapter 5	97
Half-wet micropatterned substrates for the investigation of cancer cell migration	97
5. Introduction	97
5.1. Design and fabrication of half-wet micropatterned substrates	98
5.2. Experimental set-up for cancer cell migration analysis on HW micropatterned substrates	101
5.3. Live-cell migration tracking	105
5.3.1. Single-cell tracking analysis	106
5.4. Cell density on micropatterned substrates	109
5.5. Morphological characterization of cells as a function of gap size 111	
5.6. Cytoskeleton and nuclei adaptation	115
5.7. Orientation of cells along the micro-gaps	117
5.8. ECM deposition on micro-gaps during cell migration	119
Conclusion and future perspectives	123
Appendix	125
“Patterned carboxymethyl-dextran functionalized surfaces using organic mixed monolayers for biosensing applications”	126
Introduction	126
1. Carboxymethyl-dextran (CMD) patterned surfaces for biosensing application	128
1.1. Design and fabrication of OTS/APTES patterned surfaces	130
1.1.1. Characterization of OTS/APTES patterned surfaces.....	132
1.2. Fabrication of Carboxymethyl-dextran (CMD) patterned surfaces 134	
1.2.1. Characterization of carboxymethyl-dextran (CMD) patterned surfaces 135	
1.3. Validation of the CMD-based patterned platform for biosensing application	137
1.3.1. Fabrication parameter can affect the yield of immobilization protein 138	
1.3.2. Chemiluminescence assay to validate the signal read-out on CMD patterned SiO ₂ surfaces.....	140

1.3.3. Validation of specificity of the luminescence readout on CMD patterned SiO ₂ surfaces.....	141
1.3.4. Binding assay on patterned surfaces compared to ELISA standard plate-based assay	143
1.3.5. Carboxymethyl-dextran functionalization of glass coverslip allows to use fluorescence imaging as readout of binding assays	144
2. Conclusions	147
3. Methods	148
References	152
Ringraziamenti	166

Acknowledgments

I would like to thank for the financial support the *Doctoral School of Nanotechnology* of the *University of Trieste*, the *Nano-Region Interreg V-A Italy-Slovenia 2014-2020 strategic project* and the *Istituto Officina dei Materiali - Consiglio Nazionale delle Ricerche (CNR-IOM)* of Trieste.

Thanks to Professor Vincent Torre for giving me the opportunity to use the Live-Cell Imaging Instrumentation and to Dott. Pietro Parisse for the AFM imaging analysis (shown in the Chapter 5 of this thesis).

I would like to express my deepest gratitude to my supervisor, Dott. Marco Lazzarino, and to my tutors, Dott. Laura Andolfi and Dott. Simone Dal Zilio. Your rich experience, continuous support, valuable advice, and fruitful conversations have been with me throughout my PhD. I will cherish for the future the passion and enthusiasm you have instilled in me during these years, and I think that is one of the best gifts I will take away from this experience.

Thanks to all my colleagues with whom I have shared this beautiful PhD journey and to all my collaborators.

Abstract

Cell migration is a multistep process that is critical for the control and maintenance of tissue homeostasis, and its dysregulation can lead to cancer development and progression. Understanding the mechanisms underlying cancer cell migration is fundamental to developing new diagnostic and therapeutic approaches to combat this disease.

Mechanical and topographical features determine the ability of cancer cells to migrate through the extracellular matrix and increase their metastatic potential. In this work, a novel nanomechanical sensor was developed with a special configuration: a micrometer gap around a suspended cantilever enables to operate the sensor at the liquid-air interface while keeping one face dry and the other in contact with a liquid solution.

This design improves the mechanical performance of the sensor in liquid and allows to discriminate the metastatic potential of different cancer cell lines, such as MDA-MB -231 and MCF -7, by determining the forces exerted by the migrating cells on the sensor.

The same configuration was used to develop a 2D assay based on substrates in which micro-gaps were patterned on a silicon nitride membrane. The special adaptation at the liquid-air interface allows the creation of 3D features useful for studying the effects of topography on cancer cell migration.

Introduction

Cell motility and migration are highly integrated, multistep processes crucial for creating and maintaining the proper organization of multicellular organisms. They are key phenomena of embryonic morphogenesis, tissue regeneration, wound healing, and immune response.

This process plays a key role in cancer development and progression. In fact, metastasis, a hallmark of cancer, the second leading cause of death worldwide, is the result of uncontrolled cell migration. During metastasis cancer cells migrate from the primary tumor to reach target organs where they continue to grow, a process known as *tumor invasion*. For cancer cells to metastasize, they must have the unique ability to adapt to different environmental conditions by adopting different morphologies and migratory characteristics to promote their motility.

The study of cancer cell migration requires the investigation of various physical and topographic features that determine the modes of migration and invasiveness of cancer cells through the microenvironment. Indeed, during invasion cells must squeeze through extracellular matrix exerting forces and experiencing different physical confinements.

Understanding the mechanisms underlying cell migration is important to define new diagnostic markers and therapeutic approaches for cancer. Despite recent advances in the field of mechanobiology, many dynamics underlying cancer migration and metastasis development remain unclear to date, and many questions remain unanswered: What is the role of mechanics in migration processes, cancer development and tumor metastasis, and what topographical aspects characterize tumor development and progression. In this work, the mechanisms of cell migration are analyzed from a physical perspective, together with some innovative approaches to study the forces exerted by cells during migration and the effects of topographic features on the behavior of migrating cells. These tools may be useful both to better understand

the dynamics of mechanobiology and to complement computational modeling techniques that address the simulation of these dynamics. In addition, the ability to distinguish tumor cell types with different invasive capabilities based on forces and responses to topographic features could be an important tool for developing diagnostic techniques.

Chapter 1 of this thesis provides an overview of cell migration and how the aspects related to the interaction of cells with the surrounding microenvironment can determine the migration mode: from the forces that cells perceive and exert to move and migrate, to the dimensionality and topography of the extracellular matrix, both in physiological and pathological contents, such as cancer.

Chapter 2 highlights features and limitations of current 2D and 3D assays used to study different aspects of cell migration, from phenotypical to quantitative assays for the investigation of forces exerted by the cells and microstructured surfaces to analyze the effects of topography. Chapter 3 provides a detailed overview of micro- and nanomechanical sensors and their use as biosensors and the challenges for the investigation of biological phenomena.

Chapter 4 describes the advantages of using nanomechanical sensors as platform for investigation of forces exerted by cancer cell during migration. This platform has enabled to distinguish the metastatic potential of two different cancer cell lines by detecting the forces exerted by moving cell on the sensor.

Chapter 5 analyzes the use of micro- and nanostructures to study the effects of topography on cell behavior and present an innovative platform that uses the meniscus created at the liquid-air interface of micro- structured gaps to study the behavior of migrating cells as a function of topography and confined space perception.

In the *Appendix*, the results of a work carried out in collaboration with the Karolinska Institute are reported. Wherein this case a novel platform for immobilizing proteins was designed and developed for use as a bioassay platform.

Chapter 1

Cell migration and cancer: a physical perspective

1.1. Cell migration

In humans, as well as within most living forms, the role played by cell migration begins shortly after conception, follows us throughout our adult lives, and may even contribute to our death¹. Indeed, cell migration regulates morphogenesis throughout embryonic development and during gastrulation large group of cells migrate together in the form of sheets to create the three-layered embryo. Then, cells migrate from the various epithelial layers to their target sites where they differentiate into the specialized cells of the various tissues and organs¹. In the adult, migration contributes to several physiological and pathological processes from vascular disease, chronic inflammatory disease, and cancer. Therefore, understanding the mechanisms of cell migration promises effective therapeutic approaches for the treatment of disease and the production of artificial tissue¹.

Cell migration is defined as the actual movement of individual cells, cell sheets, and clusters from one location to another. The term “cell motility” is often used interchangeably, but may technically imply a less coordinated and purposeful movement of cells^{2,3}. Cell migration through the tissue is the result of a continuous cycle of interdependent steps. During the first step, the moving cell becomes polarized and expands (Fig. 1.1A). Then, the expansion of the leading edge of the cell, which adheres to the extracellular matrix (ECM) substrate, forms cell protrusions such as lamellipodia, filopodia, pseudopodia, or invadopodia. These protrusions are usually driven by actin polymerization and stabilized by adhesion to the ECM or to neighboring cells via transmembrane receptors associated with the actomyosin cytoskeleton (Fig. 1.1B). Although many different receptors are involved in the migration of different cell types,

integrins represent the most important family of migration-promoting receptors. These receptors act as the "feet" of a migrating cell by assisting adhesion to the ECM and by connecting to actin filaments within the cell via adapters. In the third step, these adhesions serve as traction for migration as the cell moves forward over them (Fig. 1.1C), and they are broken down on the backside of the cell, allowing it to detach (Fig. 1.1D). Thus integrins connect the ECM to the cytoskeleton and serve also as *mechano-sensors* modulating the dynamics of the cytoskeleton^{1,4,5}.

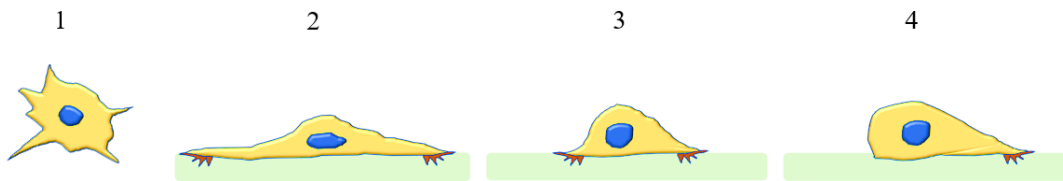


Figure 1.1: The first step of cell migration involves the polarization and the formation of protrusion in the direction of migration; in the second step, these protrusions adhere to the extracellular matrix via transmembrane receptors. In the third step, the cell body shrinks, and the previously formed adhesions serve as traction sites for migration as the cell moves forward over them. In the last step, the cell degrades the adhesions at the back of the cell, allowing it to detach and then proceed to the next cycle.

1.2. The role of forces in cell migration

The role of forces in biological processes has been subject of a great interest in the last decades, as mechanics plays an important role in many biological processes from physiological to pathological states⁶.

Mechanobiology is concerned with how physical forces affect the shape, fate, and behavior of cells. Although mechanobiology is widely considered as an emerging discipline, its concept was proposed more than a hundred years ago by mathematical biologist D'Arcy Wentworth Thompson. In his 1917 book "On Growth and Form"⁷, he imagined that life forms reflected physics and mathematical principles⁸. Since then, mechanobiologists have attempted to transform cell and developmental biology into a field of quantitative science and technology⁹.

Cells perceive mechanical stimuli through localized mechanoreceptors and translate the force by modulating their behavior through a process called "mechanotransduction."

Cells are not only passive force receivers, but also dynamically adapt to externally applied forces or stiff matrices generating a proportional force. Cells adjust their tension force when exposed to a continuous force by initiating cellular machinery that modulates a reciprocal actomyosin-cytoskeleton-dependent tension in a process called "mechanoreciprocity." This process in turn stimulates matrix remodeling and stiffening and alters cell-cell adhesion until cells reach a state of tension homeostasis. This reciprocal force response can strongly influence cell behavior by promoting cell spreading, growth, survival, and motility^{7,9}.

In order to migrate, the cell body must change shape and acquire a spatial asymmetry that allows it to convert intracellular generated forces into a net displacement of the cell body and increase stiffness to interact with surrounding tissue structures⁴.

During the first steps of cell migration, a protrusive force is required to extend membrane protrusions. Subsequently, areas of the leading edge or the entire cell body contract, creating a contractile or traction force that leads to a gradual forward sliding of the cell body and its trailing edge structures^{4,5}(Fig. 1.2). Moreover, the integrin receptors, which assists cell during the process, connect the ECM to the intracellular cytoskeleton and serve both as traction sites over which the cell moves and as mechanosensors that can alter the dynamics of the cytoskeleton.

The force transmitted to the adhesion sites from the interaction of myosin II with actin filaments that adhere to these sites. Adhesion transmit driving force and serve as traction points which the cell moves¹. The migration cycle is complete when the adhesions dissolve and the backside retracts¹.

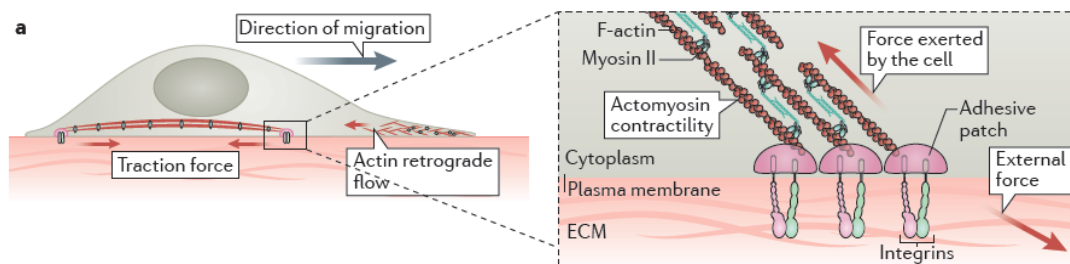


Figure 1.2: Single cells move by exerting traction forces driven by actomyosin contractility on the extracellular matrix (ECM) at integrin-based adhesions on both the front and the back. The protrusive activity at the front is driven by actin polymerization and retrograde actin flows (Ladoux et al.,2017).

Depending on group morphology and tissue context, different types and patterns of migration are involved. Cells move as sheets adhering to the extracellular matrix during epithelial morphogenesis and wound healing, but cells often can migrate as 3D strands or clusters within the tissue network during development and cancer invasion. Because of the complicated interplay between mechanical and molecular signals involved in this process, the mechanism underlying 3D cell migration within a tissue is still largely unknown.

Over the past decade there have been significant advances in the understanding of 2D sheet migration⁸ thanks to the development of biophysical tools, such as traction force microscopy, which has allowed to create a spatiotemporal force cartography of the epithelium⁸.

1.3. Cancer cell migration and invasion

Cancer is a disease that results from uncontrolled cell growth. The capability of cancer cells to activate invasion and metastasis as dysregulation of the migration process is one of the hallmarks of cancer and it is indicative for poor prognosis of patients (Fig. 1.3) ^{10,11}.

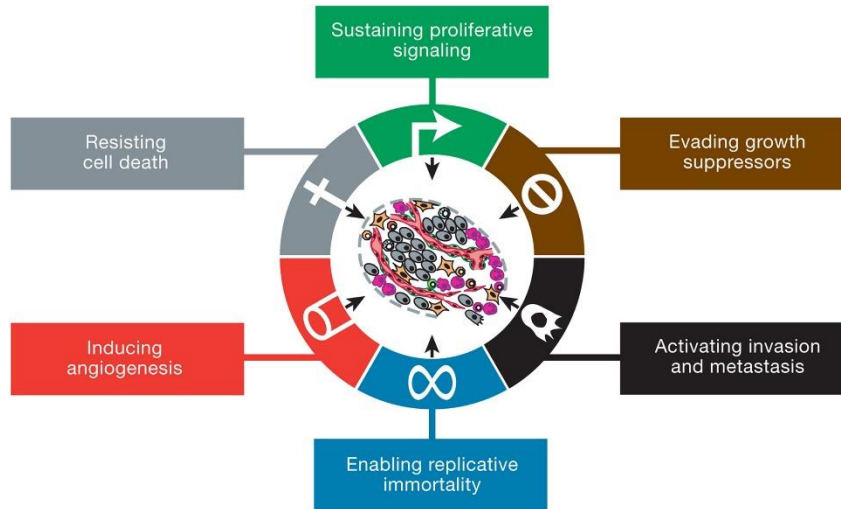


Figure 1.3: The hallmarks of cancer include six biological skills that are acquired during the development of cancer in humans. Among them, the activation of invasion and metastasis is associated with uncontrolled cell migration and involves alteration of molecular and biophysical properties that allow cells to remodel the microenvironment and invade tissues¹¹ (Hanahan e Weinberg, 2011).

Migration is often used in biology as a generic term for any directed cell movement within the body. Migration and invasion are clearly separate concepts in experimental biology. *Migration* is defined as the directional movements of cells on a substrate such as basal membranes, ECM fibers, or plastic plates. *Invasion* is defined as cell movement through a 3D matrix and its continuously remodeling. In order to move through the matrix, a cell must change its shape and interact with the ECM, which on one hand provides a barrier for the moving cell body. Invasion involves adhesion, degradation of ECM, and migration. For cells that migrate in 3D without remodeling of 3D matrix, as leukocytes, it is used the term 3D migration. The ability to migrate is a prerequisite for invasion, but a cell can migrate without invasion¹⁰.

Metastasis is caused by the invasion of the primary tumor cells and involves several processes such as infiltrative growth through the ECM, cell migration through blood or lymphatic vessels, and the formation of distant colonies¹⁰. Several models of tumor invasion and metastasis have been proposed. In general, epithelial cell transition from a mesenchymal state to adopt a migratory phenotype, a process referred to as epithelial-mesenchymal transition. The migratory mechanism adopted by cells after this transition can be divided into two broad categories: single cell and collective migration¹². Single cell migration allows cells to position themselves in tissue or secondary growths or to migrate through tissues, as is the case in morphogenesis and cancer¹³. Collective migration is defined as the coordinated movement of a group of cells that are physically connected and maintain their intercellular connections and collective polarity².

Single cells use two main modes of migration, amoeboid and mesenchymal. Amoeboid migration is characterized by blebbing, weak adhesions, and rapid motility, while mesenchymal migration is characterized by strong stress fibers, cellular polarization, and a leading and trailing edge. It is noteworthy that certain cell types can switch between different migration modes at different times as they move through different microenvironments. The migration mode used by a cell is mediated in part by its adhesion to the matrix, which in turn is controlled by the chemical and mechanical properties of the ECM. For example, cellular actomyosin activity is responsible for generating mechanical signals from the ECM to the cell. It leads to the generation of a contractile force within the cytoskeleton, which is transmitted to adhesion complexes that connect cells to their environment to facilitate movement through the matrix. These adhesion complexes are critical for mesenchymal migration¹². There is great interest in understanding the basic principles underlying the steps of metastatic spread for potential therapeutic treatment.

1.4. The role of forces in cancer cell migration

In normal tissues, such as epithelium, cells can perceive forces from their neighbors and extracellular matrix through specific mechanoreceptor. Cells may also be subjected to nonspecific forces that affect the entire tissue, such as interstitial pressure, compression, and shear flow, and it works continuously to achieve the balance to maintain the homeostasis (Fig. 1.4a). Dysregulation of forces at the cellular and tissue levels can trigger mechano-signals that compromise tissue integrity and function and promote disease progression⁶. Cancer cells exist in a mechanically and chemically heterogeneous microenvironment which undergoes dynamic changes throughout neoplastic progression¹⁴. These cells have the unique ability to adapt to different environmental conditions by adopting different morphologies and migratory features to promote their motility¹⁵. During invasion a tumor cell continues to experience mechanical forces, including traction forces associated with locomotion and protrusive forces from the cell's leading edge. The metastatic cascade begins with a change in motility within a subpopulation of cancer cells in a solid primary tumor, a process known as tumor invasion (Fig. 1.4b). Single or collective cancer cells migrate through the barrier of the primary solid tumor mass (Fig. 1.4c). After they are passively transported by vascular flow throughout the body to target sites suitable for metastasis. Shear forces have been shown to activate gene programs associated with cytoskeletal remodeling and altered cell-cell adhesion. When they reach these target regions, the cancer cells have become even more motile after transmigration through confluent endothelial monolayers (Fig. 1.4d). In addition, the mechanical properties of motile and invasive cells have been shown to be altered. Transformed cells also show impaired mechano-reciprocity, so they often exert abnormally high forces in response to compliant matrix. These increased cell-generated forces disrupt the integrity of cell-cell- junction, compromise tissue polarity, promote survival independent of anchorage, and enhance invasion. All

of these steps in the metastatic pathway appear to involve mechanical interactions between cancer cells and their microenvironment^{16,17}.

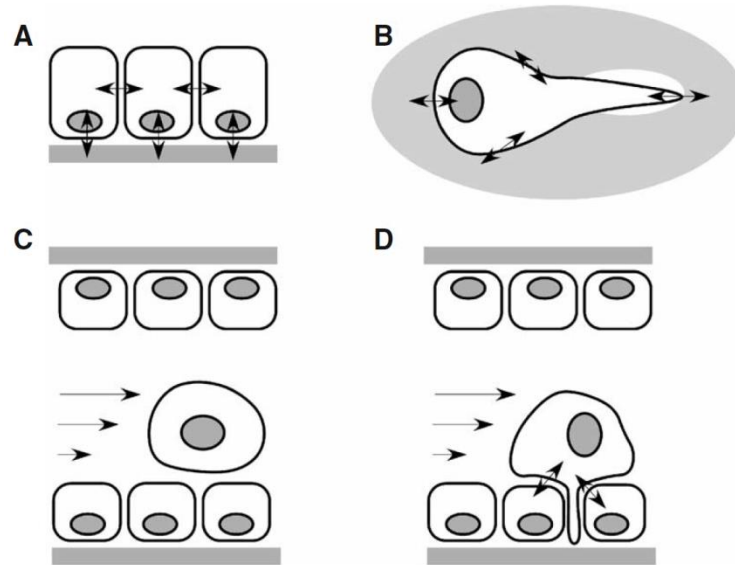


Figure 1.4: a) In normal tissue, cells sense and exert mechanical forces from their neighbors and the extracellular matrix, as well as interstitial pressure and shear flow; b) When a tumor cell detaches from the primary tumor, there continues to be an exchange of forces, such as traction forces associated with locomotion and protrusion; c) When a tumor cell escapes the primary tissue shear forces have been shown to activate gene programs associated with cytoskeletal remodeling; d) To metastasize, the cell must mechanically interact with other cells to invade the tissue (Kumar and Weaver, 2009).

Breast cancer, for example, is characterized by changes in cellular rheology and tissue-level forces, tissue stiffening, and progressive loss of stress homeostasis, which has been used to identify tumors⁹.

The developing breast is subjected to a number of forces that support its normal function. During lactation, for example, the normal breast is subjected to compressive stress on the luminal epithelial cells and basement membrane due to milk accumulation and alveolar expansion. After suckling and stimulation by oxytocin, contraction of the myoepithelium puts the epithelial cells under tensile stress to push the milk out of the alveoli (Fig. 1.5a). In the absence of this stimulus, the milk accumulates in the acinus and eventually exerts an outward compressive force on the surrounding epithelium. This compressive force is balanced by a compensatory, inwardly directed resistive force. The combination of these two forces eventually compromises the integrity of the tight junctions between alveolar cells. The transformation of breast cells (Fig. 1.5b) leads to uncontrolled proliferation and increased survival of luminal epithelial cells within the ductal tree and compromises normal ductal architecture. With continued growth and abnormal survival, the abnormal pre-neoplastic luminal mammary epithelial cells eventually expand and fill the mammary ducts. The expanding luminal epithelial mass exerts outwardly increasing compressive forces on the basement membrane and adjacent myoepithelium. These forces are opposed by an inwardly directed resisting force.

The desmoplastic stroma, characterized by dramatic changes in extracellular matrix (ECM) topology and stiffens over time. This rigid parenchyma exerts an increasingly strong inward resistance force on the expanding pre-neoplastic duct. Over time, the number of myoepithelial cells surrounding the preneoplastic mass decreases and the basement membrane becomes thinner, and the interstitial fluid pressure increases, reflecting a leaky vasculature and impaired lymphatic drainage. In response to their genetic alterations and the altered material properties of the matrix, the pre-neoplastic luminal epithelial

cells exhibit altered stress tension homeostasis and respond to the combination of forces and stromal cues by invading the mammary parenchyma⁹.

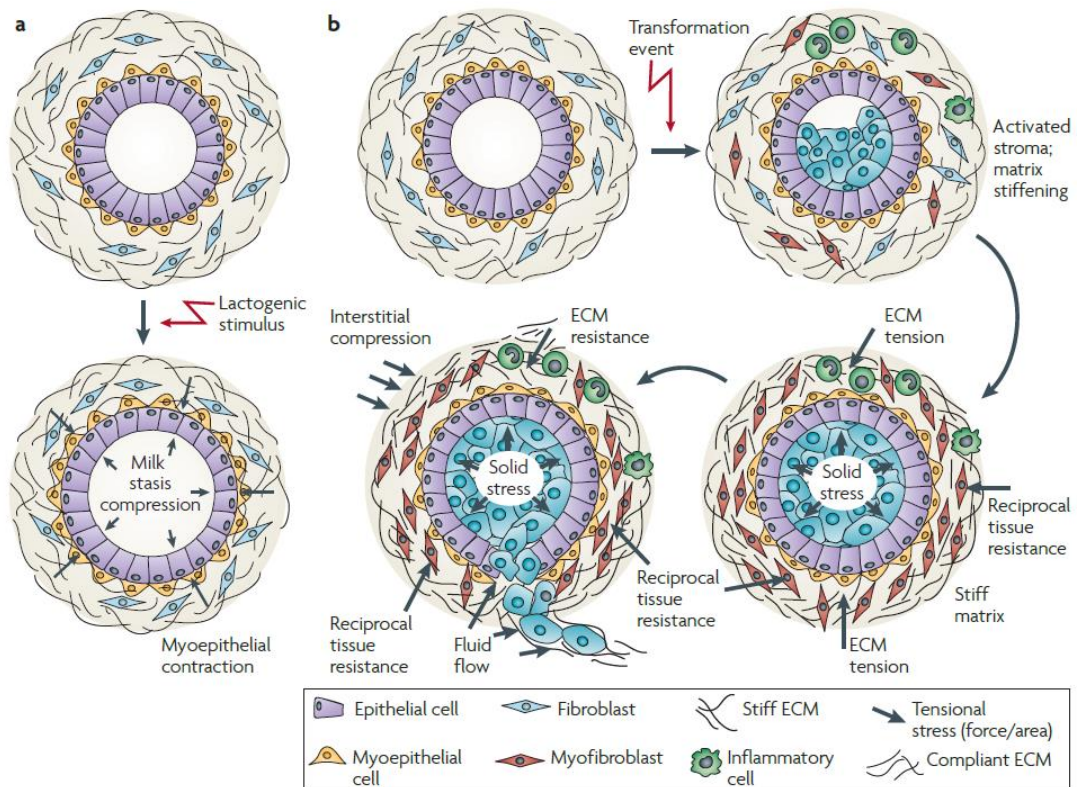


Figure 1.5: Example of how normal tissue, in this case epithelial breast tissue, can turn into cancer due to dysregulation of forces within the normal tissue and the ability of breast cells to expand. A) The normal breast tissue that transforms into homeostasis during lactation. B) The steps that lead to the transformation and invasion of cells into the tissue due to transformed forces (Butcher et al., 2009).

1.5. Dimensionality in cell migration

Three classes of dimensionality are involved in cell migration: the 1D aligned fibers, the 2D planar substrates classically used in cell culture, and the 3D matrix (Fig. 1.6). The shape and migration mode of a cell are determined by three main parameters: adhesion to a substrate, actin protrusion, and actomyosin contraction. These parameters depend on cellular factors such as gene expression and environmental cues, which can be divided into chemical, mechanical, such as the forces experienced by the cell derived by the mechanical properties and geometric factors (topology and pore size) of the ECM¹⁸.

The studies about cell migration on two-dimensional standard flat tissue cultures have revealed many important molecular mechanisms.

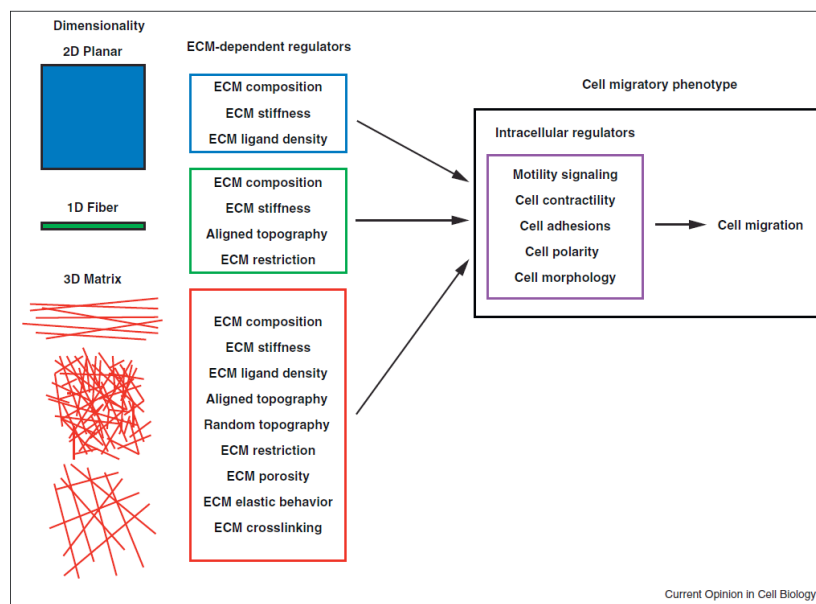


Figure 1.6: Dimensional regulation of cell migration. Illustration of the numerous unique ECM-dependent regulators (center column) associated with 2D, 1D, and 3D migration. These microenvironmental regulators in turn influence intracellular regulatory pathways that govern the migratory phenotype (right panel) and determine how cell migration proceed (Yamada, 2019).

In a standard 2D migration model, ECM molecules are presented to cells as a flat layer of globular molecules with no appreciable fibrillar structure. This flat

ECM topography promotes a spread cell morphology, and fibroblasts acquire a "hand mirror" (Fig. 1.7a) with apical/basal polarity in the cell adhesions and much of the contractile apparatus associated with the 2D surface¹⁹.

In 2D cell migration cycle used by cells moving across a flat 2D substrate, cells undergo cycles of repeated protrusion, adhesion, and contraction that occur as a continuum or even simultaneously rather than as discrete and separate steps¹⁸. The 2D migration is by far the best understood form of cell migration and has been extensively studied in cell cultures. Although in normal physiology migration along surfaces is the exception rather than the rule, there are cases where cells migrate in two dimensions. For example, epithelial cells that close skin wounds undergo a form of collective 2D migration, as do cells that migrate on bone.

The 1D migration models mimic single fibers in aligned native 3D ECMs and have highlighted the important role of topography and contact guidance during migration. The 1D ECM constrains cell shape by preventing lateral spreading of cells and promoting a uniaxial phenotype (Fig. 1.7b)¹⁹.

The 1D migration along aligned extracellular matrix fibers is referred to as 'contact guidance' and has been documented both *in vitro* and *in vivo*. In the context of cancer, linear collagen fibrils running perpendicular to invasive human breast cancers are a prognostic marker for poor cancer survival^{20,21}. Moreover, modeling studies show that tumor and cancer stem cells, as well as some leukocytes, preferentially migrate along such linear collagen arrangements¹⁸.

Over the past decade, modeling of cell motility in three-dimensional (3D) ECM models that mimic more physiological *in vivo* conditions has revealed significant differences between 2D and 3D cell migration. It is now clear that a variety of properties of the ECM microenvironment such as topographic cues can directly influence these intracellular regulatory mechanisms to control the nature and rate of cell migration^{19,22,23}.

In 3D ECM (Fig. 1.7c, d, e), the fibrillar topography and pore size reduce lateral spreading and do not impose apical/basal polarity on either the adhesions or the actin cytoskeleton¹⁹.

Migration through 3D environment is challenging for cells as they must squeeze through complex or dense extracellular structures. This requires specific cellular adaptations to the mechanical properties of the ECM or its remodeling. In addition to navigating through different ECM environments and overcoming extracellular barriers, cells often interact with neighboring cells and tissues through physical and signaling interactions¹⁸.

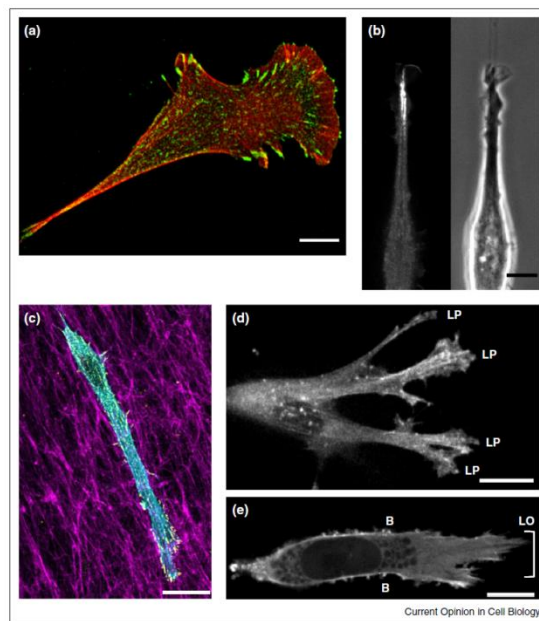


Figure 1.7: a) NIH/3T3 fibroblast demonstrating a classic hand-mirror morphology on a 2D substrate; b) eGFP-VASP (left) and phase contrast (right) image of a NIH/ 3T3 fibroblast migrating along a 1D micropatterned line; c) NIH/3T3 fibroblast within a 3D-CDM showing staining for F-actin (phalloidin, cyan), paxillin (yellow), and fibronectin (magenta); d) eGFP-actin expressed in a human foreskin fibroblast illustrating lamellipodia in non-linear 3D collagen.; e) Lobopodia (LO) and lateral blebs (B) shown by eGFP-actin as a human foreskin fibroblast migrates through a linear-elastic 3D-CDM. Scale bars: 10 μm ¹⁹.

As shown in the Figure 1.6, one of the ECM-dependent regulators in the 3D environment is the “confinement” that cells experienced. Indeed, the

extracellular microenvironment contains confining pores and channel-like pathways based mainly on collagen (Fig. 1.8a,b)²⁴. These microtracks, which cells follow to migrate, can also occur in vascular tissue, within and around blood vessels (Fig. 1.8c). *In vivo*, cells can also migrate through longitudinal 3D pathways with adjacent 2D interfaces, i.e., channels, between connective tissue and the basement membrane of muscles, nerves, and epithelium (Fig. 1.8d)^{25,26}. In many tissues, cells can also undergo surface curvature such as in alveoli, in intestinal villi, or in mammary glands^{23,27}.

Several *in vivo* studies performed using intravital microscopy have shown that an important mode of migration is the passage through confined spaces such as pores or tunnel-like tracks²⁸.

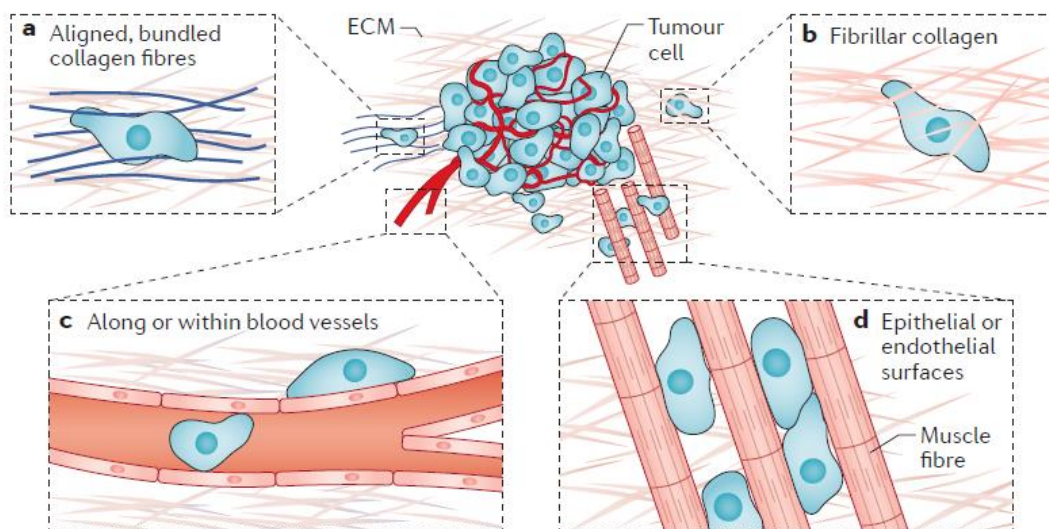


Figure 1.8: Confined cell migration in extratumoral microenvironment a) Alignment and bundling of collagen fibers at the tumor periphery provide cues for directed migration; b) Cells may also migrate through unbundled extracellular matrices (ECMs); c) Microtracks also occur both intravascularly and perivascularly; d) Cells can also migrate between epithelial or endothelial surfaces, such as those found between muscle and nerve fibers. (Paul, 2017)

There is increasing evidence that physical confinement alters the mechanism of cell migration²⁸. Cancer cells migrate *in vivo* by gradually degrading the surrounding ECM to create their own migration tracks²⁹, by following “leading”

cancer cells that open pathways for migration , or by moving through pre-existing channel-like tracks created by anatomical structures²⁵. In breast cancer, for example, local cell invasion has been found to occur predominantly along specifically aligned collagen fibers, suggesting that radial alignment of collagen fibers relative to the tumor facilitates invasion²⁰. Although research is still in its infancy, the effects of topographical architectures on cell behavior and migration have been studied using a variety of micro-structured surfaces such as microgrooves, micropillars, and microfluidic channels³⁰⁻³². Such studies have paved the way for a better understanding of the mechanisms behind cell migration and the development of cancer metastasis.

1.5.1. Investigation of the effect of topography on cell migration

Current 2D and 3D migration assay (thoroughly described in the next chapter) do not consider the important role of topography and physical confinement as main regulators of migration modes. For this reason, there has been a great deal of interest in recent decades in technological advances that allow us to precisely design substrate surfaces to control interaction. Advances in material sciences have enabled the possibility to elicit desired cellular responses on biomaterials in order to resemble different structures in 3D microenvironments. Advanced methods in material science have enabled the fabrication of nanoscale and microscale substrate features that can control adhesion, migration, and differentiation of living cells³³.

These models have been used to systematically investigate the effects of *in vivo-like* tissue geometry and curvature on cell fate²⁷, and the mechanisms of cell motility through confined spaces as they occur *in vivo*. For example, *in vitro* experiments using protein tracks, micro/nanoengineered *grooves* and *ridges* and microfluidic channels have convincingly shown that migration of adherent cells is controlled by anisotropic topographic features of the substrate a phenomenon known as "contact guidance". In such studies, nanostructures were developed to aligned collagen fibers to study cancer cell migration²¹, demonstrating that length-scale biological topographical features corresponding to those of the native basement membrane features can significantly influence epithelial cell behavior³¹(Fig. 1.9a). Using microfluidic channels several studies have shown that MDA-MB-231 cancer cells choose a wider channel when seeded in 2D printed lines, but they choose to branch regardless of the width when the channel is edged, because cells respond to a topographic cue and align based on the contact between their membrane and the wall of the confined structure(Fig. 1.9b)³².

Another example of confined spaces that cells can perceive *in vivo* are the curved surface. Indeed, many epithelial tissues exhibit complex morphology,

usually dominated by curved surfaces, as found in alveoli and intestinal villi²⁷ or blood vessel walls²³. The profound effect of surface curvature on cell behavior has only recently been recognized²³. Park *et al.* observed that cells seeded on polydimethylsiloxane (PDMS) membranes with concave or convex spherical structures actively migrate out of concave wells but settle and proliferate on convex structures³⁴ (Fig.1.9c).

In addition, adherent cells may avoid convex regions and position themselves in concave valleys during migration, and the nucleus acts as a mechanical sensor that directs the migrating cell toward concave curvatures³⁰. Interestingly, the rate of cell migration was found to be significantly higher on concave spherical surfaces than on convex spherical surfaces²³. Luciano *et al.* showed that lamin expression, chromatin condensation, and cell proliferation rate were modulated by substrate curvature, suggesting that multiple mechanotransduction pathways modulate the perception of curvature in cell assemblies³⁵.

The results are important for understanding cell organization in complex geometric environments and may inspire new strategies for geometric design of scaffolds for tissue engineering, particularly for controlling directional cell migration²³. Moreover, such studies have provided important insights into the fundamental mechanisms of cell migration that contribute to our understanding of morphogenesis and disease development, such as cancer metastasis²³.

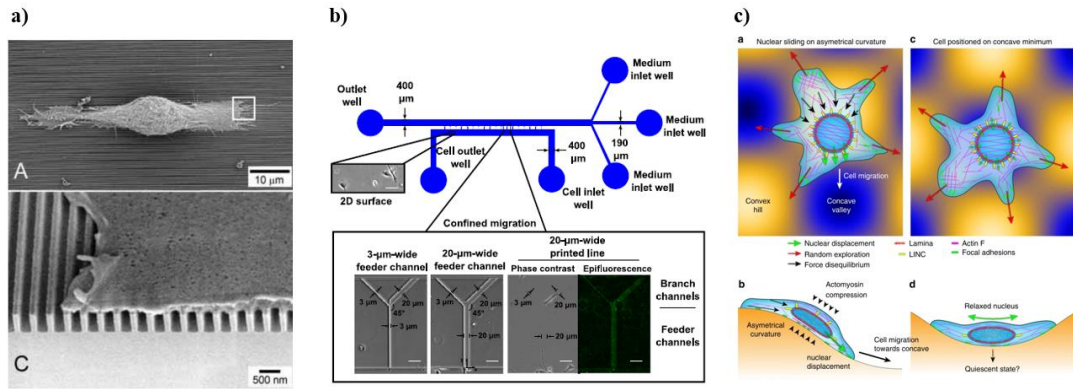


Figure 1.9: a) An examples of nanostructured surfaces that demonstrates as length-scale biological topographical features corresponding to those of the native basement membrane features can significantly influence epithelial cell behavior (Teixeira, 2013); b) cancer cells in microfluidic channels respond to a topographic cue and align based on the contact between their membrane and the wall of the confined structure (Colin, 2016); c) the migration mode and rate of cells seeded on polydimethylsiloxane (PDMS) membranes with concave or convex spherical structures change as a function of the topographical features (Park, 2009).

Chapter 2

Cell migration assays on 2D and 3D platforms

2. Introduction

For a complete study of cell migration, it is necessary to consider all aspects related to the interaction of cells with their microenvironment: from the aspect of dimensionality and the influence of the topography of the extracellular matrix on migration modes, to the forces that cells perceive and exert to move and migrate in different physiological and pathological contexts. Although these aspects have been recognized and studied separately, to date there are no essays that provide a generalized but quantitative evaluation of the migration process as a whole. Even more complicated is the study of cancer cell migration during metastasis, which involves changes in the mechanical properties, velocity, and forces required to overcome microenvironment barriers and reach distant tissues. *In vitro* metastasis assay is far from technically feasible in the near future¹⁰. Our current understanding of cell migration is based on single cell migration studies, performed using *in vitro* assays in two-dimensional (2D) and three-dimensional (3D) cell culture techniques. Below, I describe the most commonly used 2D and 3D platforms for studying migration of normal and cancer cells, such as the invasive assay.

2.1. Two-dimensional (2D) assays to study single cell migration

The 2D assays are routinely used for migration studies, but they have significant limitations because migration *in vivo* usually occurs in a 3D space. Since topography and size play a critical role in determining the behavior of cells during migration, the traditional assays have been combined with micro-structured 2D surfaces and tunable 2D substrates (such as polyacrylamide or collagen gels)¹². The most commonly used migration assays are described below.

2.1.1. Wound-healing assay

The most commonly used 2D *in vitro* model to study cell migration is the wound-healing assay (also called, scratch assay) (Fig.2.1). The basic steps involve creating a “scratch” in a confluent cell monolayer, capturing the images at the beginning and at regular intervals during cell migration to close the scratch, and comparing the images to quantify the migration rate of the cells².

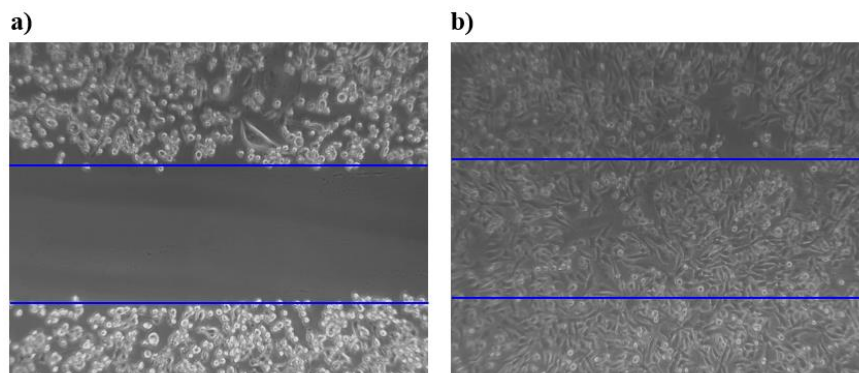


Figure 2.1: Wound-healing assay for MDA-MB-231. A scratch was made on a confluent cell monolayer by a micro-pipette tip and images were acquired at $t=0$ (a) and after 24 h (b). The images show that after 24h the MDA-MB-231 cells cover completely the entire scratch.

2.1.2. Single cell motility assay

The *single cell motility assay* measures migration on the single cell level by coating with gold particles the surfaces where cells are seeded. The migrating cells phagocytize the gold colloidal particles, and the results is the formation of black tracks over an initial uniform brighter surface (gold particles). An example of this technique is described in the Figure 2.2 ³⁶.

Also time lapse cell tracking can be used to study the migrating cells by obtaining information about total movements length and velocity¹⁰.

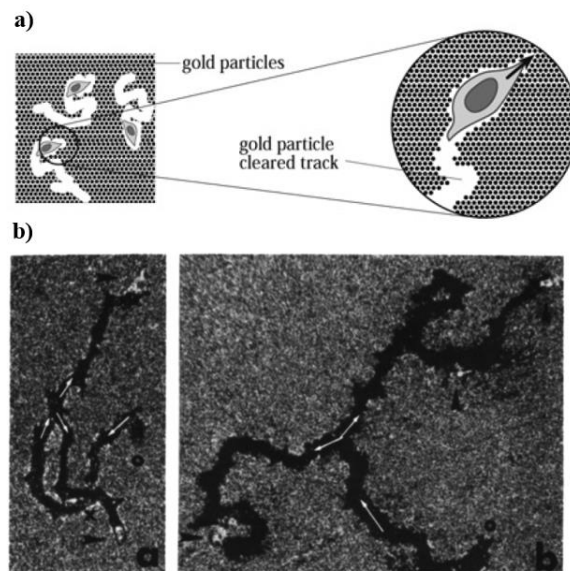


Figure 2.2: a) Schematic of a common single cell motility assay (Kramer, 2013); b) Example of tracks (black) indicated by which arrows formed by cells of 3T3 on a surface covered by gold nanoparticles (brighter colored) (Guenter Albrecht-Buehler, 1997).

2.1.3. 2D cell tracking assay

In this case the tracking of cells is performed by video microscopy in time-lapse experiments, by using a live-cell imaging instrumentation³⁷. Cell selection and tracking can be done either manually, semi-automatically, or fully automatically. For automatic cell tracking, many algorithms have been developed that can record the migration path of several dozen cells simultaneously¹⁰. Recently, optical microscopes with an environmental chamber have been improved and represent a significant development in dynamic cell imaging. Such instruments include software for remote control, image acquisition, and filter optics configuration. The system is optimized for long-term kinetic studies on living cells thanks to monitoring of temperature and CO₂ of the environmental chamber³⁸.

2.2. Three-dimensional (3D) assays to study cell migration

3D platforms reproduce better the *in vivo* behavior of cell migration. 3D *in vitro* assay can be obtained by overlaying 3D ECM scaffold with cells or by implanting multicellular spheroids. In these assay, collagen and hydrogels based on polyethylene glycol (PEG) are commonly used to mimic the microenvironment, thanks to the possibility to tune their stiffness, porosity and density¹⁰.

2.2.1. Three-dimensional matrix invasion assays

The 3D matrix invasion assay is commonly used as platform to investigate the invasiveness of cancer cells. The cancer cells are placed on a grid based on matrix proteins which may also contain chemoattractant. The measure of invasiveness is established by the depth of penetration determined by image analysis (Fig. 2.3a). Such system can be also transplanted into animals *in vivo* where cancer cells can continue to invade and then can be examined by immunochemistry after explant (Fig. 2.3b)³⁹.

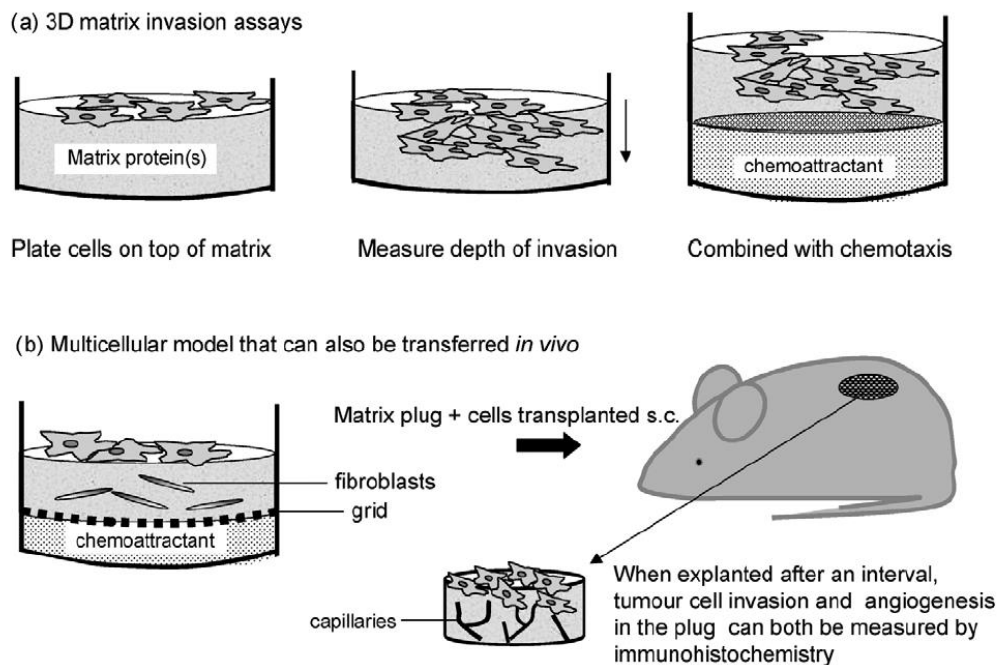


Figure 2.3: a) An example of a 3D invasion assay that allows *in vitro-in vivo* transfer. Specifically, tumor cells are placed on a matrix which may contain chemoattractant. b) once established, the entire plug (matrix + cells) can be transplanted subcutaneously into animals where tumor invasion can continue and then can be examined by immunochemistry after explant (Eccles, 2015).

2.2.2. Spheroid migration assay

In the “spheroid migration assay”, after attachment of the multicellular tumor cell spheroids to the plastic surface of a 2D platform, the cells start to migrate, and the area of attachment is increased as cells move out. This assay is only possible if cells are capable to form spheroids¹⁰. *In vivo* assay are usually performed by injecting 3D spheroids into the tissue matrix¹³.

2.2.3. Trans-well migration assay

Another 3D platform is the *trans-well assay* is based on two chambers containing a medium and separated by a porous membrane through which the cells transmigrate (Fig. 2.4). It is important to choose a pore diameter which allows only active transmigration i.e., smaller than the cell diameter to avoid passive diffusion of the cells across the membrane. Membranes are available with pore diameters between 3 and 12 μm . Cells are seeded in the upper part and can migrate through the pores to the lower part containing a medium with an attractant, then they are fixed and visualized^{10,39}.

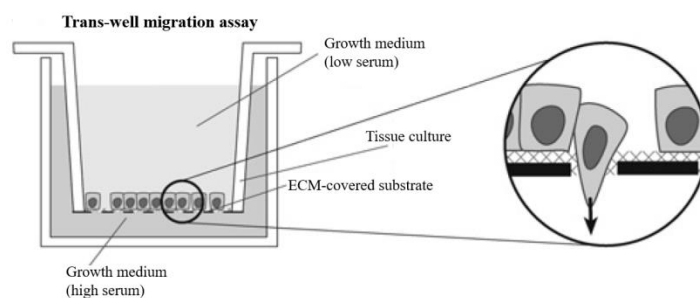


Figure 2.4: *Trans-well migration assay in which extracellular matrix (ECM) has closed the pores at the interface between the two chambers. The higher the invasion potential, the higher the number of cells that can transmigrate through the pores by degradation of the ECM. (Image modified by Kramer2013).*

2.2.4. 3D cell tracking assay

As described for 2D cell tracking, the *3D cell tracking assay* uses time-lapse video microscopy for automated image analysis to track the path of moving cells. Since it is difficult to track single cell in a 3D environment over a long period of time, many strategies have been developed from confocal or multiphoton microscopy to digital holography microscopy. All these strategies require expensive instrumentations and advanced data processing analysis, moreover only a limited number of cells can be analyzed simultaneously¹⁰.

Chapter 3

The investigation of forces in cell biology

3. Introduction

Mechanical stimuli play an important role in cell functions. The study of cell stiffness measured by atomic force microscopy, optical tweezers, and micropipette aspiration revealed to be a promising biomarker in cancer research¹². For example, metastatic cells in breast, prostate, and lung cancer models develop higher traction forces compared with non metastatic cells⁴⁰. These results underscore the need to focus more on accurate assays when studying the mechanics of cell migration and the importance of mechanics for cancer diagnosis and therapy¹². There is a great interest about forces generated by cells and how cells can translate it in signals that can modulate adhesion and migration. Indeed, as described in the Chapter 1, cells use traction forces to explore their environment, move, and remodel the matrix. Moreover, several studies have shown that measuring the forces exerted by cells during migration can be used to assess the degree of malignancy of cancer cells. In this Chapter, the most common assays for studying the forces exerted by cells are presented. Since in this thesis I will present a novel nanomechanical sensor that can detect the forces exerted by cancer cells during migration, a detailed overview of micro- and nano- mechanical sensors, their advantages and challenges for use in biological applications will also be described below.

3.1 Assays for the study of forces

3.1.1. Traction force microscopy

The most used method to measure the forces involved in the migration is the traction force microscopy (TFM). Traction forces are measured by plating cells onto soft, deformable gels in which fluorescent microbeads are embedded. As a cell adheres and migrates, the displacement of these markers is translated into cell-mediated stress (Fig. 3.1a)¹².

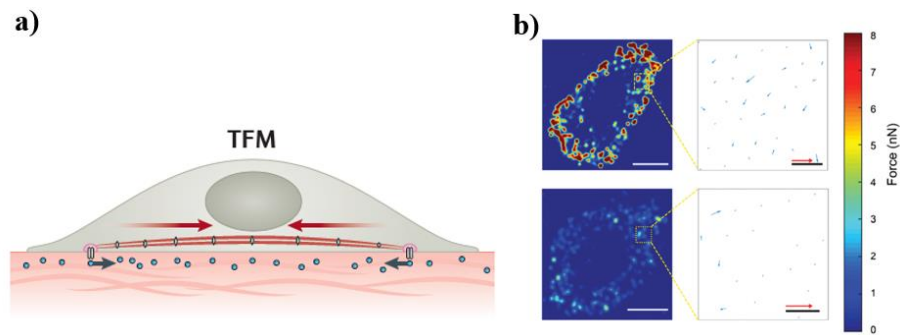


Figure 3.1: a) Schematic of TFM cells are plated on deformable gels into which small markers (e.g., beads) are embedded to track deformation patterns. The arrows indicate the direction of traction forces (Ladoux, 2017); b) Traction force heat map obtained by analyze the displacement of beads (Li, 2017).

The experiment involves the optical imaging of the distribution of beads in the unstressed and stressed state after cell migration (Fig. 3.1b). Silicone and polyacrylamide (PA) are typically used as substrate materials. To promote cell adhesion both surfaces must be conjugated with ECM, and it could be difficult to reproduce in different experimental conditions⁴¹. Several studies have been performed to study the differences in traction force exerted by metastatic and non metastatic cells. More aggressive cells generate higher traction forces compared with less or not metastatic cells^{14,40}. This method can be modified for use in 3D microenvironment by performing experiments using confocal microscopy¹⁰. The most commonly used ECM material for 3D culture is

reconstituted collagen type I hydrogel⁴¹. Although TFM is the gold standard method for measuring cellular forces, it is experimentally complex, and force reconstruction is a mathematically unsolved problem. This means that a small amount of noise in the displacement field will produce a large error in the calculated force field⁴². These factors have prevented the widespread use of TFM in non-specialist laboratories and ultimately its use as a useful diagnostic tool⁴¹.

3.1.2. Micropatterned substrates-based TFM

An alternative method is based on the growth of cells on micropatterned substrates. Micromachining methods allow the fabrication of cell substrates based on patterned arrays of elastic micropillars, usually in polydimethylsiloxane (PDMS) or polyacrylamide (PA). The influence of the geometry of the micropillars on the substrate stiffness allows the creation of heterogeneous mechanical environments without changing the material properties. If cells are grown on these substrates the deflection of the micropillars gives direct information about local forces exerted by cells^{43,44} (Fig. 3.2).

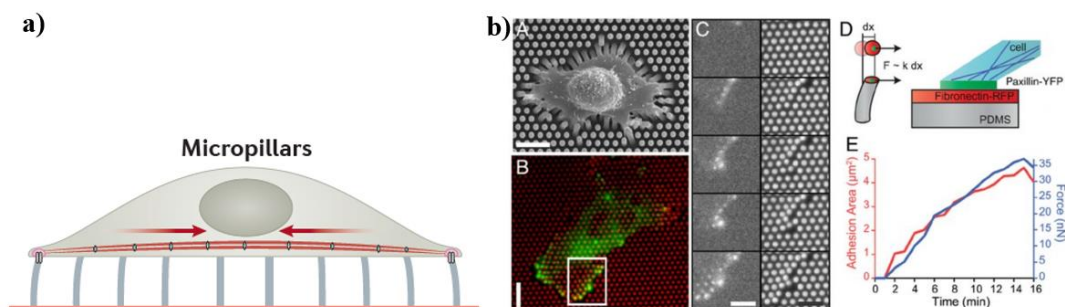


Figure 3.2: a) As an alternative method, cells are grown on arrays of micrometer-sized flexible polydimethylsiloxane (PDMS) pillars, whose displacement provides direct information about the local forces exerted by the cells (Ladoux,2017); b) The images show the dynamics of focal adhesion and traction forces generated by cells and on the right the schematic of pillars displacement and focal adhesion formation (Trichet,2012).

This approach has several advantages over TFM methods such as the ability to compute displacements without the need for a reference image. However, due to the limited stiffness range of the substrates and the low adhesion of the cells, it is far from mimicking *in vivo* conditions⁴⁵.

The methods described above rely on analysis of substrate deformation due to cell movement and require very expensive equipment that is not affordable to all laboratories, as well as sophisticated data analysis. These factors hinder the widespread use of TFM in non-specialist laboratories and ultimately its use as a useful diagnostic tool. Some studies have considered the possibility of improving such a system by using MEMS technology to create microarrays and provide multiplex platforms⁴⁶ but they always rely on the microscopic traction method with micropillars fabricated on the surface of *microPAD*.

3.1.3. Molecular sensors

The conventional methods described above for studying cell traction forces are performed by measuring the deformations of synthetic substrates. The same principle can be applied at the nanoscale to measure the force exerted by a given molecule. If the mechanical properties of a material can be evaluated at the molecular level, the deformations of individual molecules can be converted into forces⁴². This principle has been used to develop a wide range of sensors for measuring molecular forces⁴⁷. In a common setup, a mechanically calibrated linker (using atomic force microscopy or optical tweezers) flanked by two different fluorophores is encoded into a protein of interest. A force applied to the molecule causes the linker to stretch, changing the fluorescence resonance energy transfer (FRET) between the two fluorophores. The sensitivity and force range of the sensor, typically between 1 and 10 pN, are determined by the mechanical properties of the linker and the FRET range of the fluorophore pair.

Direct fluorescence measurement instead of ratiometric measurement (as in FRET) can dramatically increase sensitivity.

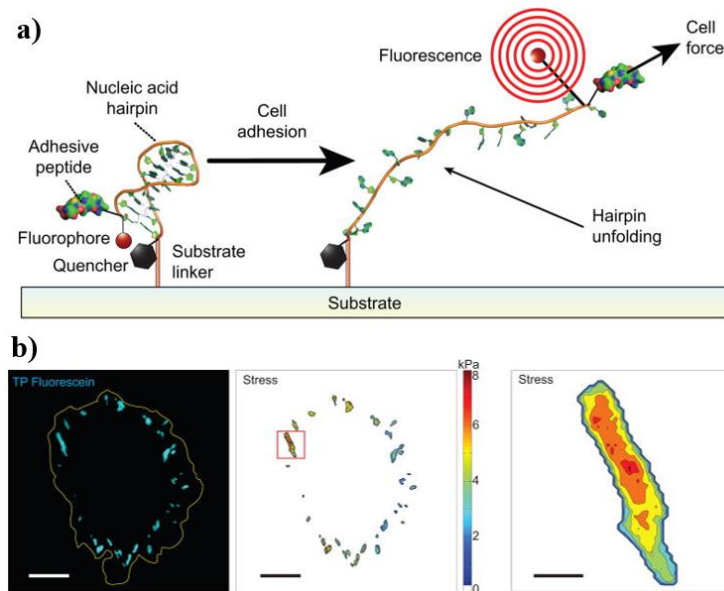


Figure 3.3: a) Schematic representation of molecular tension probes using a DNA hairpin. When sufficient force is applied to unfold the hairpin, the fluorophore separates from the quencher and fluoresces; b) Image of cells on tension probes-coated substrate and analysis of stress (Blakely, 2015).

As an alternative to protein domains, DNA hairpin linkers, whose force threshold can be controlled by tuning the DNA sequence, allow measurement of forces up to the 100 pN range (Fig. 3.3)⁴⁸. As with all fluorophore-based sensors, there are limitations to their use and calibration due to fading and optical sensitivity. Unlike TFM-based methods, these methods provide only the magnitude and not the direction of the forces⁴¹.

3.2. Mechanical biosensors

In recent years, rapid advances in the design and fabrication of micro- and nanostructures have opened up great opportunities to develop new devices coupled with functional cells and molecules that improve the performance of cellular and molecular biosensors.

The field of biosensing has grown exponentially since the first report of their application⁴⁹. The term “biosensor” was coined by Camman⁵⁰ and defined by the IUPAC as: “A device that uses specific biochemical reactions mediated by isolated enzymes, immune systems, tissues, organelles or whole cells to detect chemical compounds usually by electrical, thermal or optical signals.”^{51,52} Biosensors are used not only to detect the presence and amount of an analyte, but also to study various other phenomena, such as the effect of drugs on living cells, cell physiology and also cell mechanics, including the even whole cells and microorganisms investigation^{51,53}.

Biosensors are essentially composed of three units, namely a biorecognition element (BRE), a transducer, and an amplifier and processor (Fig. 3.4). The BRE detects the analyte of interest, the transducer converts the biological detection event into a measurable signal, that is further processed by a processor and amplifier to provide an output signal.

Based on the transducing method, biosensors can be divided into^{51,52}:

- *Optical* biosensors which can be colorimetric, fluorescent, luminescent, and interferometric, such as ELISA and SPR assay.
- *Mechanical* biosensors, such as MEMs and NEMs, also used to investigate biological processes in micro and nano-scale.
- *Electrochemical* biosensors (amperometric, potentiometric, and conductometric).

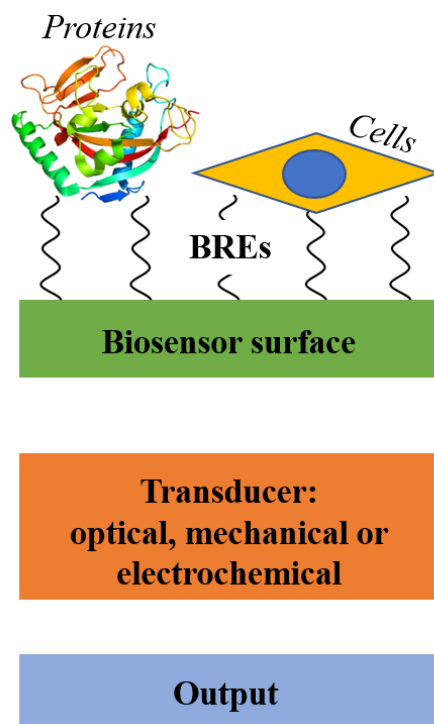


Figure 3.4: The schematic shows the basic structure of a biosensor with the three main components, i.e., biorecognition elements (BREs), transducer and processor to obtain the output signal. Based on the transducer, biosensors can be classified into optical, mechanical, and electrochemical. The BRE is represented by analytes (proteins) or cells whose dynamics can be analyzed.

As mature, versatile, and well-established technologies, electrical and optical biosensors dominate global research in biological detection. However, the mechanical nature of many fundamental biological processes paved the way for the development of mechanical biosensors⁵⁴.

Indeed, recent experimental evidence demonstrates the role of mechanics involved in biological processes: the role of forces involving proteins in molecular recognition events⁵⁵, the importance of the mechanosensitive (MS) ion channel in the perception of mechanical stimuli by different cell types^{56,57}, and the forces acting on the membrane surface in the curvature perception^{35,58,59}. Thanks to their small size and high sensitivity, mechanical sensors based on microelectromechanical systems (MEMS) technologies can be easily integrated into portable “lab-on-chip” platforms for the investigation of mechanics

involved both in physiological and pathological processes, and to perform “point-of-care” analyses⁶⁰. Their manufacturing approaches include reliability and mass production with consequently cost reduction. In the next sections, we will focus on the description of mechanical biosensors based on micro- cantilevers, and their use for the study of cellular and molecular dynamics.

3.3. Cantilever-based micro- and nanomechanical sensors

Among mechanical sensors based on MEMS, microcantilevers are the most promising devices for biosensing applications⁶⁰. These devices, developed as the sensing part of an atomic force microscope, have also proven to be useful as stand-alone sensors, thanks to their ability to measure changes in surface tension, adsorbed mass, and thermal dispersion. MEMS based on cantilever consist of a cantilever probe, a mechanical transducer, and the processor. They were originally focused on materials science⁶¹, but they have been extended to chemistry, biology, medicine, and clinical diagnostic applications^{62,63}. Mechanical biosensors offer several advantages: they achieve exceptional mass resolution that can detect minute amounts of analytes⁶⁴ or the mass of living cells⁶⁵; they can be used to quantify forces at the cellular level⁴¹. These devices open up possibilities for novel label-free detectors with high sensitivity and very high multiplexing levels can perform local, high-resolution, and label-free molecular recognition measurements (Fig. 3.5)^{60,66}. Although MEMs devices have a characteristic length scale between 1 mm and 1 μm ⁶⁷, if used in biological application, because of their ability to detect features at the nanometer scale, such as nanomotion or nanoforces, they are called nanomechanical sensors^{54,68,69}. Such systems can quantify the motions, forces, and masses of living cells, providing insight into mechanical properties involved in biomolecular interactions and fundamental biological processes. Nanomechanical biosensors can be broadly classified according to the basic functionality of the devices: they can measure or detect the presence of a particular analyte in solution; measure particular physical property of the analyte; or to study and characterize a particular biological process⁷⁰. The first application of a cantilever-based sensor for chemical detection dates back to 1994, when Gimzewski et al. showed that the static bending of a cantilever was capable of detecting heat changes on the order of picojoules to perform sensitive photothermal spectroscopy⁷¹.

In the same year, Thundat and co-workers showed that a cantilever could be used to monitor very sensitive temperature changes⁷². Subsequently, the scope of cantilever-based sensors was extended to various sensing applications, from chemistry to biology, proteomics and genomics^{54,62,63,70}. The change in the static deflection of the cantilever or the change in the amplitude of oscillation, is most commonly detected by the optical lever technique used by the atomic force microscopy (AFM). Essentially, a laser is reflected from the back of the cantilever onto a position-sensitive diode^{54,62}.

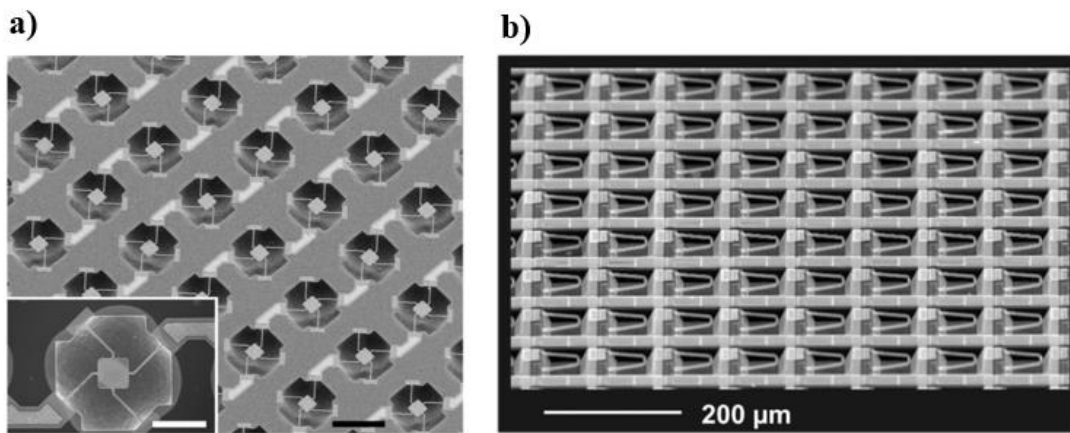


Figure 3.5: Examples of multiplexed cantilever-like micromechanical sensors. a) a sensor array developed for the measurements of adherent cell mass growth (Park, 2010); b) the image shows a “Millipede” cantilever array developed for thermomechanical local-probe technique (Waggoner,2010).

3.4. Materials and manufacturing processes

3.4.1. Silicon-based cantilevers

Generally, cantilevers are made from either silicon-based or polymer-based materials. Regardless of the material, there are some requirements for the final cantilever structure: the cantilever should be as thin and long as possible to increase sensitivity to surface stress; the cantilever clamping should minimize clamping losses and the geometry should allow for a high Q-factor; the surface of the cantilever must be reflective for optical readout; the cantilever should ideally have no initial bending.

Since most research published to date uses an external optical readout to measure the cantilever's deflection, the micromachining processes have focused on fabricating simple, free-standing beams suitable for optical readout, i.e. silicon-based⁶². Originally developed by IC industry in the 1960s, silicon microfabrication has become a widespread technology. Well characterized and long-term stable, materials such as silicon, silicon nitride and silicon oxide can operate over a wide temperature range and under many environmental conditions. Since the manufacturing process require precision machining, clean-room based processes are used in which cantilevers are fabricated by patterning in a silicon wafer. A typical strategy for fabricating silicon-based cantilevers consists of three main steps: coating of the substrate with material layers needed for lithography processes, patterning of the cantilever and release of the device⁶². This approach, in which the suspended structures are defined by etching from the back side throughout the wafer, is called bulk micromachining⁷³. The process results in free-standing cantilevers that are accessible from both sides of the wafer.

3.4.2. Polymeric-based cantilever

Since the late 1990s, the production of polymer-based cantilevers has been increasingly reported. The main motivation for the introduction of polymers is that the Young's modulus is typically two orders of magnitude lower than conventional silicon-based materials. Consequently, the stiffness of the cantilevers is lower and the sensitivity increases. The fabrication of polymer-based micromechanical devices is still at an early stage, and many issues need to be solved before robust and stable cantilevers can be routinely fabricated. One of the major challenges in using polymer chips as mechanical sensors is the stability of the devices during measurements: the adsorption of moisture in liquids or degassing in vacuum will cause the output signal to drift; the long-term stability of such cantilevers can be affected by creep deformation, ageing, or bleaching. Since the reflectivity of thin polymer cantilevers is insufficient for optical readout, metal coating is required. However, laser reflectivity can be provided by integrating a small metal pad at the tip of the cantilever^{81,101,102,95,109–111}, as in some biosensors application⁷⁴. To avoid this problem, many studies determine the deflection of the beam by taking time-lapse images, but this reduces the sensitivity of the force analysis.

3.5. Operation modes of nanomechanical biosensors: static and dynamic mode

In sensing application, the microcantilever deflection can be divided into two modes of detection: static and dynamic. The static mode of deflection occurs when an adsorbed species causes differential surface stresses on the opposite surfaces of the microcantilever. Static deflection is used to determine the amount of material adsorbed onto a microcantilever⁷⁵. Molecules that adsorb on a cantilever do not only add a mass but also generate a surface stress due to interactions between the molecules and the cantilever surface⁶². Molecular recognition induces surface stress on one side of a nanomechanical system and leads to bending of the system. The bending results from the change in surface energy of the active surface, which is minimized by elastic expansion or contraction with respect to the opposite surface⁵⁴. This effect is the basis for a variety of label-free transductions of ligand-receptor interactions, such as nucleic acid hybridization and antibiotic-bacterial interactions⁷⁶. In the dynamic mode of detection, the frequency of vibration of the beam changes as species are adsorbed onto the cantilever⁷⁵. In dynamic mode, the resonance frequency of the cantilever is related to the added mass on the surface of the sensor, in particular the resonance frequency decreases with increasing mass^{62,63}. By implementing an optomechanical or electromechanical transduction scheme, both dynamic and static modes are suitable for quantitative measurements^{77,78}.

A microcantilever can be modeled as a cantilever beam (thickness, t ; width, w ; and length, L) that is built in (fixed) at one of its ends⁷⁵ (Fig. 3.6).

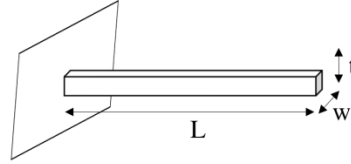


Figure 3.6: Schematic of a simple rectangular cantilever geometry with a fixed end: L , length; w , width; t , thickness.

The change in surface stress of a cantilever as result of biomolecular adsorption can be mathematically explained by applying Stoney's equation:

$$R = 6 \frac{Et^2}{6\Delta s(1 - \nu)}$$

which establishes a linear relationship between the change in stress surface (Δs) and the change in curvature (R). Where E is the modulus of elasticity, ν is the Poisson's ratio, and t is the beam thickness. This equation assumes that the beam is isotropic and homogeneous, that the beam thickness is small compared to the lateral dimensions, and that the strains and torsions are small. This is reasonably consistent with the most commonly used micro-toggle beams, but this equation applies only to plates that are unrestrained along the edges and have uniform curvature. In 1966, Stoney's formula was modified to be applicable to cantilever that are clamped to one side. Thus, the surface stress (Δs) is related to the cantilever deflection (Δz), via the length of the cantilever, L :

$$\Delta z = \frac{3(1 - \nu)L^2}{Et^2} \Delta s$$

Here it can be seen that the deflection can be optimized by reducing the thickness and increasing the length of the cantilever. Although Stoney's equation is still used today, the origin of surface stress and

its relationship to force transmission is controversial. A first attempt at an explanation was proposed by Fritz et al. according to which the hybridization of DNA strands on the cantilever could cause a compressive stress on its surface^{62,77}.

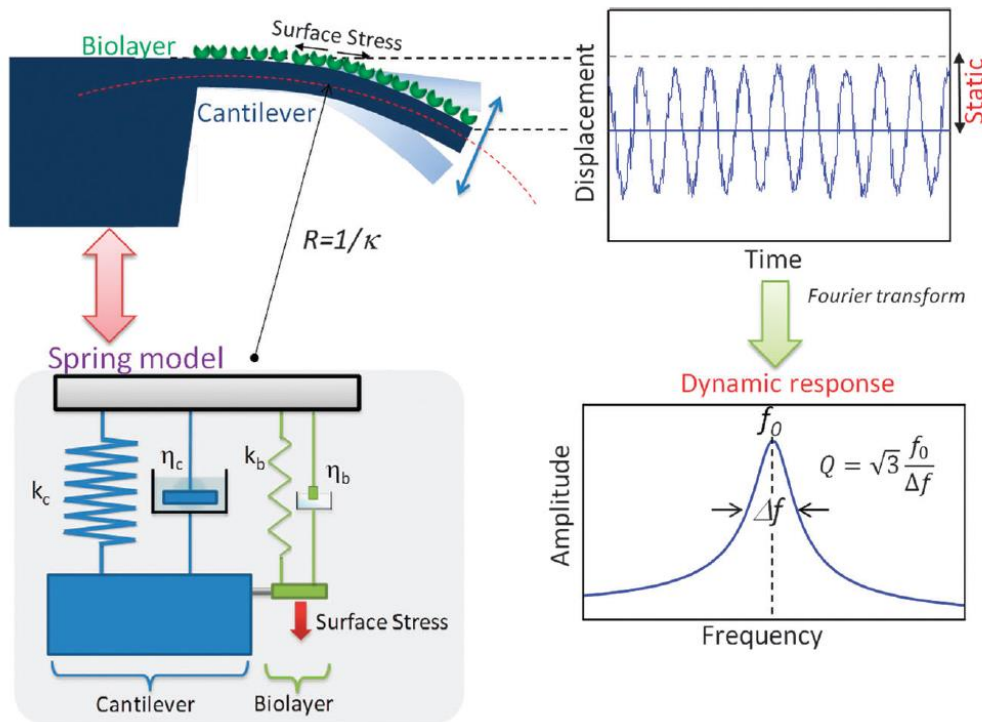


Figure 3.7: Schematic of mechanical effect (surface stress) induced by biological adsorption on the response of a nanomechanical system. The elasticity and mechanical losses of the cantilever can be modeled by a spring model that take into account a static and dynamic response (Tamayo, 2012).

It is possible to model the elasticity and mechanical losses of a cantilever by a spring and a damper with the spring constant k_c and the damping coefficient η_c , which are related to the flexural rigidity and the quality factor of the cantilever, respectively (Fig. 3.7). The biological layer acts in parallel as a spring and damper with a spring constant k_b and damping coefficient η_b . The biomolecules on the top of the cantilever generate surface stresses that

produce a static mechanical bending (obtained as mean displacement signal) with curvature R . The oscillation can also be analyzed in the frequency domain to determine the resonant frequency and quality factor (Q) of the cantilever⁵⁴.

Since the resonance frequency of the cantilever decreases with increasing mass^{62,63}, it is possible to estimate the change in mass from atto- to zeptogram range, by measuring the negative shift in its frequency⁶⁴. The mass sensitivity of a cantilever-base mass sensors can be improved reducing the dimension of the sensor. For a thin beam, assuming a linearly elastic material and small deflection, the equation of its motion is given by the Euler-Bernoulli beam equation. From this equation, it follows that a beam has certain vibration modes, each with particular spatial shape. The vibration frequency of each mode shape is called the eigenfrequency⁶².

The resonance frequency depends on the geometry, size and clamping configuration. The flexural resonance frequencies of a beam with rectangular and uniform cross section are given by this formula:

$$f_n \cong \frac{\beta_n^2}{21.7656} \left(\frac{E}{\rho}\right)^{0.5} \left(\frac{t}{L^2}\right)$$

Where E is the Young's modulus, ρ is the material density, t is the beam thickness, L is the beam length and β_n is the eigenvalue. In dynamic mode, an important parameter is the mechanical quality factor⁷⁹. Indeed, this parameter characterizes the shape of its resonance frequency curve near each resonance mode⁷⁵ and is defined as the ratio of the resonance peak at a certain resonance mode to the full width at the half-maximum (FWHM) of the same resonance peak⁷⁵.

The quality factor Q is defined by:

$$Q = \sqrt{3} \frac{f_0}{\Delta f}$$

Where f_0 is the resonance frequency, and Δf is the half-width resonant peak frequency or full-width at half maximum. The quality factor depends on the geometry of the cantilever and dissipative forces acting on it, usually globally referred as damping. Damping depends on the cantilever material, its geometry, and the composition of the environment in which it oscillates. When immersed in a viscous medium, like the cellular culture medium, the high damping causes the broadening of the resonance peak reducing the minimum detectable frequency change⁶². Therefore, fully immersing the cantilever in a liquid environment makes accurate measurements of mass difficult due to the viscous damping.

3.6. Actuation of cantilever-based sensors

To measure frequency changes of cantilever-based sensors, the cantilever must be driven by an external actuator. In most commercially available scanning probe microscopes (e.g., AFM), this is accomplished by an external piezo drive mounted near the cantilever⁸⁰.

In most experimental configurations, the cantilever is driven by an external piezoelectric platform on which the cantilever chip is mounted. This actuation method is also referred to as mechanical excitation. Alternatively, the actuator can be integrated into the sensors. There are a variety of techniques for actuating cantilever-based sensors, depending on the actuation principle used: electrostatic actuation, thermal actuation, and magnetomotive actuation⁶². For biosensing, cantilever-based sensors in liquids are often driven by mechanical or magnetic excitation methods. The mechanical method also excites unwanted resonances from the fluid, making it difficult to detect the resonance inherent in the cantilever. Magnetic excitation is accomplished by coating the cantilever with a ferromagnetic layer and applying a sinusoidal magnetic field. However, magnetic coatings are often corroded in liquids and can lead to undesirable

bending of the cantilever. To overcome these limitations, photothermal excitation was developed to improve sensitivity in liquids⁸¹. In photothermal actuation, a metal-coated cantilever is irradiated with a power-modulated excitation laser focused near the cantilever's clamping area. The thermal expansion caused by the excitation laser on the metal coating leads to mechanical stresses in the cantilever, which trigger the cantilever vibration⁸².

3.7. Read-out principles

A common method for measuring the deflection of a cantilever is the *optical lever technique*, in which a focused laser diode beam (Fig. 3.8a) is reflected from the free end of the cantilever onto a photodiode or position-sensitive detector. When the cantilever bends, the reflected light moves on the surface of the photodetector and this movement is proportional to the deflection of the cantilever (Fig. 3.8b). An alternative approach uses *piezoresistive cantilevers*. Changes in the electrical conductivity of the piezoresistive material that is placed under voltage can be used to monitor the stress and thus the bending of the cantilever.

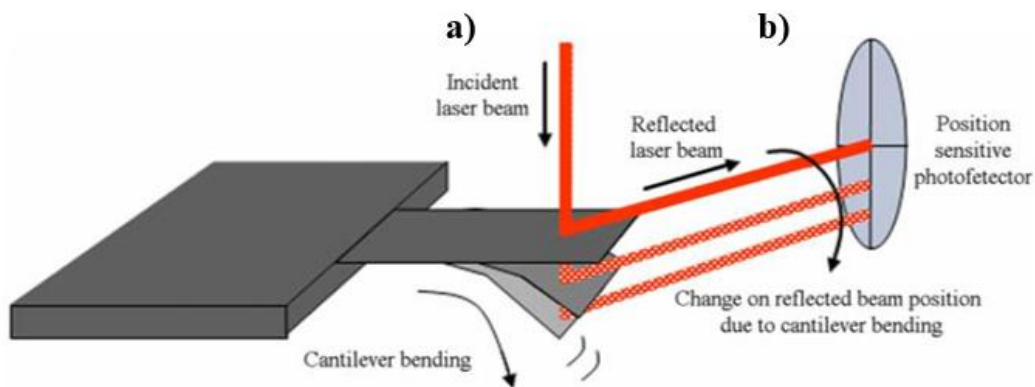


Figure 3.8: Schematic of the optical lever technique, the most used read-out principle for measuring the deflection of a cantilever. The incident laser beam is reflected on the surface of the sensor (a) and the reflected light moves on the photodiode (Carrascosa, 2006).

Another method is based on the *interference* that occurs between a reference laser beam and the reflection of the cantilever. Other methods use interdigitated cantilevers as *optical diffraction gratings*. The reflected laser light forms a diffraction pattern in which the intensity is proportional to the deflection of the cantilever⁸⁰. When a cantilever is placed near a parallel electrode, the deflection of the cantilever results in a capacitance change. This method is called *capacitive read-out*. Detection of resonant frequencies of nanoscale cantilevers has been performed by tunneling and by hard contact read-out⁶². Other innovative approaches came from the use of polymeric resins tailored by a thermomechanical process⁸³.

3.8. Functionalization processes for biological purposes

For a cantilever-based sensor to detect the presence of analytes, the conformational changes of protein or DNA molecules^{75,77}, the surface stress induced by the interaction of living cells on the surface of the cantilever^{84,85}, it must be coated with specific molecules that allow the adhesion of analytes and cells to the surface of the sensor.

While both sides of the cantilever can be functionalized for measuring mass, it is important for surface stress measurements that only one side of the cantilever is coated, since equal generation of surface stress on both side of the cantilever will not cause the cantilever deflection⁶².

The immobilization of bioreceptors on the sensor surface strongly affects the quality of microcantilever analyzes because it influences not only the efficiency of protein and DNA binding, but also the degree of nonspecific binding and accessibility to targets. The immobilization process should avoid any change in the mechanical properties of the cantilever, be uniform to maximize surface stress and allow accessibility to target⁶⁰.

The most commonly used technology for coating cantilevers is to first coat the cantilever on one side with a thin layer of gold (20-100 nm), which provides an excellent opportunity for self-assembling monolayer (SAM) thiol chemistry^{60,62}.

Silane coupling chemistry is commonly used for silicon and silicon nitride surface. The presence of silanol group (Si-OH) on the surface of silicon oxide allows silanization methods⁵⁴ to be carried out using silicon-oxygen-silicon-carbon bonds that are thermodynamically and hydrolytically stable. The final organosilicon molecules consist of an organic group such as methyl, a reactive group such as ethoxy, and a terminal group such as amino or carboxyl, which give the modified surface the desired properties⁵⁴.

The silanization reaction is usually performed by immersing the surfaces in a solution containing the organosilicon molecule. Since both side are modified in

this way, this method is more suitable for biosensors based on nanomechanical resonators that do not require the asymmetry of functionalization needed for surface stress measurements^{54,62}. In addition, new methods have been developed for polymer cantilevers, such as the use of epoxy groups on the surface of SU-8⁶². The use of the cantilever both as a probe for AFM-based techniques (such as single cell force spectroscopy and nanomotion analysis) and as a mechanical biosensor to study the behavior of living cells in different environments paved the way for the development of new strategies and protocols to promote the attachment of living biological samples. For example, when studying the correlation between the nanomotion signal or the stress changes induced by the presence of cells on the cantilever in real time, the main purpose of this preparatory procedure is to ensure the firm adhesion of the sample to the surface of the cantilever and to avoid the loss of the cells during the experiments⁸⁶. Several protocols based on the use of chemical cross-linkers such as (3-Aminopropyl)triethoxysilane (APTES), glutaraldehyde, poly-L-lysine, fibronectin, concanavalin A, and collagen provide good adhesion for living cells⁸⁶⁻⁸⁸. In most cases, the cantilever is immersed in the solution containing the functionalizing agent, which covers both sides of the sensors. Functionalization of both sides does not affect the result of nanomotion analysis per se (laser refraction) but is quite difficult to interpret in real-time measurements about dynamics of biological processes. For this reason, recent work has explored the possibility of functionalizing the cantilever with a pattern of SAMs to target only one side of the cantilever and achieve the placement of cells on the most sensitive part of the sensor using microcontact printing technology⁸⁹. Although this strategy could be an interesting alternative to the conventional functionalization, it is still difficult to reproduce and perform in standard laboratories.

3.9. Real-time and end-point assay detection for biosensing

In biosensing application, experiments with nanomechanical sensors can be designed to follow the mechanical response of the analyzed biological process in real-time or by end-point detection, both in static (Fig.3.9a) and dynamic (Fig.3.9b) mode.

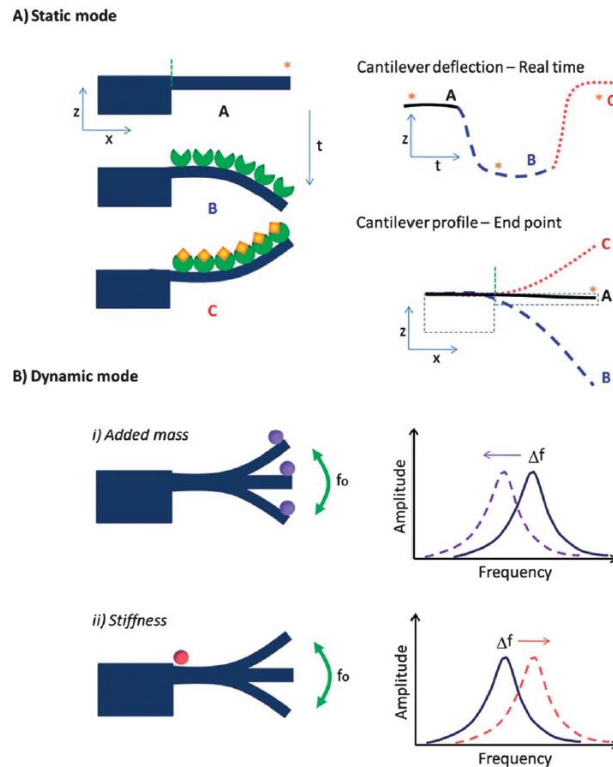


Figure 3.9: Main operating modes of nanomechanical sensors: a) static and b) dynamic. Both modes can operate in real-time or as end-point detection tests. In static mode, the end-point measures the entire cantilever profile or at least a referenced z-position. In dynamic mode, changes in added mass or stiffness can be tracked (Calleja,2012).

Real-time detection provides information on the kinetics of biomolecular interactions, whereas end-point detection is limited to detecting the variation of mass added (analyte or cells) on cantilever after the experiment. Nanomechanical sensors operating in static mode have been widely used for real time detection in fluids⁷⁰. In dynamic mode, end-point analysis is preferred and most experiments must be performed in air or humid environments due to

the viscous drag of the fluids^{79,90}. In addition to their ability to detect binding events⁹¹ and adsorbate masses, nanomechanical biosensors have been successfully used to follow dynamic processes such as conformational changes⁷⁰, as real-time formation of a self-assembled monolayer (SAM)⁹¹ or hybridization of DNA molecules⁷⁷ as a result of a change in surface stress⁶². Moreover, cantilevers allowed real-time measurement of ATP-induced conformational changes in the terminase of bacteriophage T7⁸⁴. Since their ability to detect mechanical changes, cantilever-base sensors have shown great interest in the study of biological processes involving whole living cells attached to their surfaces, such as mass changes. A first attempt to use micro-mechanical cantilever as sensors to analyze the growth of living cells was made by Prescesky in 1992. Then, the detection of bacteria and viral particles was performed only in dry environment^{92,93}.

In 2005, Gfeller et al. performed the analysis of growing bacteria attached on the cantilever surface, by incubating the sensor in humid environment⁹⁴. In all these experiments, the analysis was performed in dynamic mode by an end-point evaluation of the mass changing after the attachment of living organism on the surface of the cantilever.

3.10. Nanomechanical sensors for biological detection

The first time that a cantilever was used to calculate the mass of single living cells in fluids was performed by Park *et al.*⁹⁵ in 2008 using a living cantilever array. After 2 years, they repeated the attempt to obtain a more sensitive sensor with uniform mass to obtain a more accurate measurement of mass change of live Hela cells during growth in real-time⁶⁵. We will have to wait until 2017 for Muller *et al.* to study the mass of single cells in fluid with a conventional cantilever, in real time⁹⁶. They have developed a picobalance in which cells are attached to the surface of a commercial cantilever and a low-power intensity-modulated blue laser is focused on the base of the sensor. The motion, amplitude, and phase of the cantilever were read-out optically with an infrared laser. In addition to the opportunity to follow changes in resonance frequency due to mass loading of adherent cells on the cantilever surface, nanomechanical sensors have been demonstrated to be able for real-time investigation of vibrations of living microbial cell^{97,98}. By using their sensitivity and versatility, Longo *et al.* in 2013 developed a diagnostic tool based on cantilevers that detect in real-time the fluctuation by using the AFM-optical detection system (Fig. 3.10).

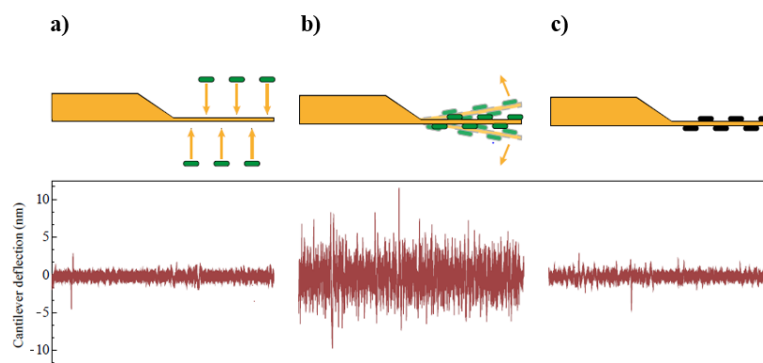


Figure 3.10: Schematic of a nanomechanical detection experiment (top) and the corresponding cantilever deflection curve (bottom): a) before live specimens are attached to the sensor, the fluctuations are small; b) when the specimens are immobilized on both sides of the sensor, the fluctuations increase; c) when microorganisms are killed by a chemical or physical agent, the sensor returns to small fluctuations (Kasas, 2015).

This new application is called as AFM nanomotion detection⁹⁹ and uses the high sensitivity of nanomechanical sensors to transduce the movements that characterize living systems. The displacement of nanomechanical sensors ranges from angstrom to hundreds of nanometer⁵⁴. This technique can detect nanometer-scale vibrations from living cells attached to commercial cantilevers. Their presence on the surface of the cantilever leads to dynamic deformations that can be recorded in time. The time evolution of this motion can be correlated with the viability and metabolic state of the living samples¹⁰⁰. Subsequently, nanoscale vibrations have been observed in various cells such as bacteria⁶⁹, plant and mammalian cells⁹⁹, and also as a fast approach to determine the antibiotic susceptibility against agents of bloodstream infections⁶⁸.

3.11. Challenges in the use of nanomechanical sensor for biological application

Conventional cantilevers used as nanomechanical biological sensors must be soaked in a physiological medium, mostly a water-based medium. This condition does not significantly affect their response when operated in static mode, such as when measuring the deflection induced by a molecular recognition⁷⁷, but it becomes a serious obstacle when operated in dynamic mode. For instance, the molecular mass deposited on a cantilever can be evaluated by measuring the resonance frequency variation. In this case, the viscous damping of the medium significantly broadens the frequency response and reduces the sensitivity of the frequency shift⁶⁶.

A first attempt to minimize the effect of immersion in liquid was proposed by Melli et al.¹⁰¹. They used a superhydrophobic surface to limit the interaction of the sensor with the biological solution, but they were still able to detect the mass change in vacuum (Fig. 3.11a).

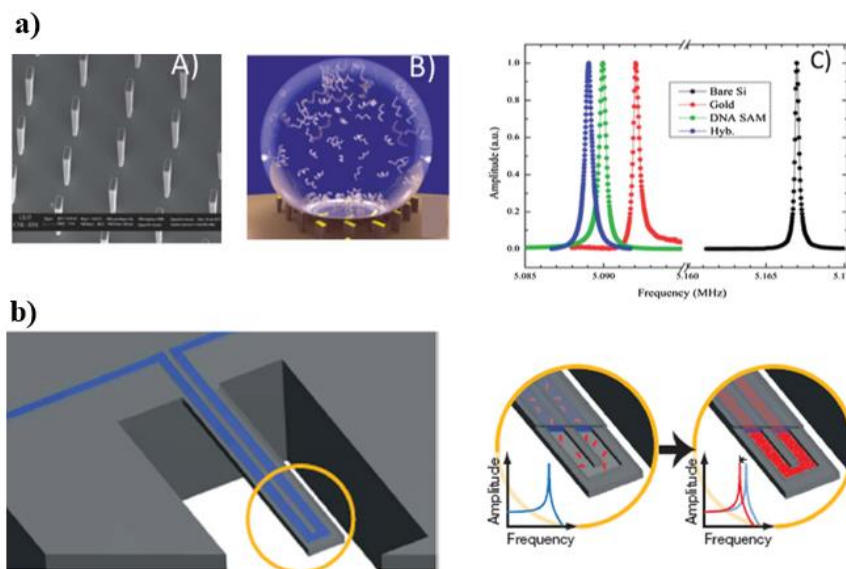


Figure 3.11: a) alternative approach to minimizing the effects of immersion of sensors in liquids using a superhydrophobic surface (Melli,2011); b) a suspended microchannel containing the liquid environment is inside translates mass changes into changes in resonant frequency (Manalis, 2007) .

A very sophisticated alternative was proposed by Manalis group who used an abrupt change of perspective by moving the liquid environment inside the cantilever, creating an oscillating microfluidic channel (Fig. 3.11b) This approach allowed the mass measurement for bacteria, but the size of the channels is too small for analyzing most eukaryotic cells¹⁰². A simpler and more effective approach was proposed by the group of Oesterschulze, who showed that using a suitable geometry, it is possible to place only one side of a cantilever in contact with the fluid while maintaining the resonance performance of the air operation. In their work, they presented a new concept to significantly reduce the viscous damping of the first out-of-plane bending mode of a cantilever by using a special interface configuration. By fabricating a cantilever surrounded by a U-shaped groove in a silicon nitride membrane (Fig. 3.12a, on left), they showed that upon contact with the fluid, the formation of a meniscus in the groove enables a so-called *partial wetting* configuration (Fig. 3.12a, on right). In this way, they were able to demonstrate that partial wetting can improve the quality factor of micromechanical cantilevers operating in liquids. Many studies have shown that with such a configuration, highly time-resolved *in situ* mass measurements in liquids with *fg*-resolution is possible (Fig. 3.12b)^{103,104}. The mechanism that could explain this difference compared to the fully immersed cantilever is not yet understood, since the breaking of symmetry by the meniscus changes also significantly changes the boundary conditions to the dynamic behavior in fluid. Otherwise, the observed improvement of the quality factor in liquid environment is a requirement to enhance the sensitivity of force and mass detection, especially for life science applications^{103–106}.

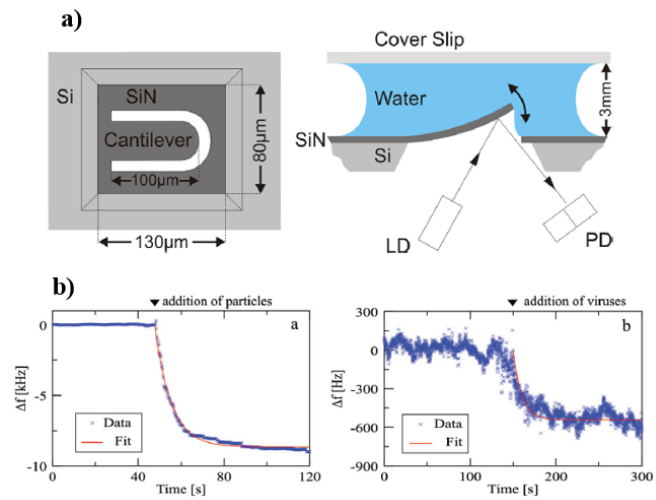


Figure 3.12: a) the design of the suspended cantilever in the silicon nitride membrane, surrounded by the groove (on the left), the partial wetting configuration of the sensor (on the right); b) an example of application of the partial wetting configuration to measure the mass of particles and living viruses in real-time mode.

3.12. Nanomechanical sensors to detect forces exerted by cells

As described in previous sections, migrating cells exert forces on the substrate to move forward. These forces, or tractions, are part of the contraction phase of migration, in which the rear part of the cell detaches from the substrate and the body of the cell moves forward.

Using microcantilevers as biosensors to measure the forces exerted by the cells could be a good alternative to the techniques described in paragraph 3.1. of this chapter. MEMS sensors are ideal for measuring forces and displacements at level of individual cells due to their small size and fine resolution. In addition, the suitability of MEMS sensors for batch manufacturing processes allows multiplexed examination, leading to robust statistical studies¹⁰⁷. Although these structures offer high sensitivity that could allow the detection of cellular dynamics, some limitations have hampered their use for studying forces exerted by cells.

For example, as early as 1997, Sheetz et al. were able to use micro-cantilevers to determine ventral traction forces as a function of time and compare them with dorsal measurements of fibroblasts (Fig. 3.13a)⁷⁴. Although this system was able to obtain information on the migration dynamics of fibroblast, the dimension of the cantilever allowed the analysis of just a small part of the cell body.

In 2005, hybrid polymer cantilevers were used to measure the contractile forces of cardiomyocytes. In that study, analysis of forces was measured by acquiring images at the edge of the microcantilever¹⁰⁸. More recently, Galbraith and Ferrell used a polymer-based cantilever to measure forces exerted by fibroblasts by optically measuring the deflection of each probe during cell attachment and spreading¹⁰⁹. Although these systems were based on hybrid polymer cantilevers to achieve low power threshold for large deformations, they suffered from low sensitivity and resolution. In addition, their dimension allowed the measurement of one cell or only part of a cell per time.

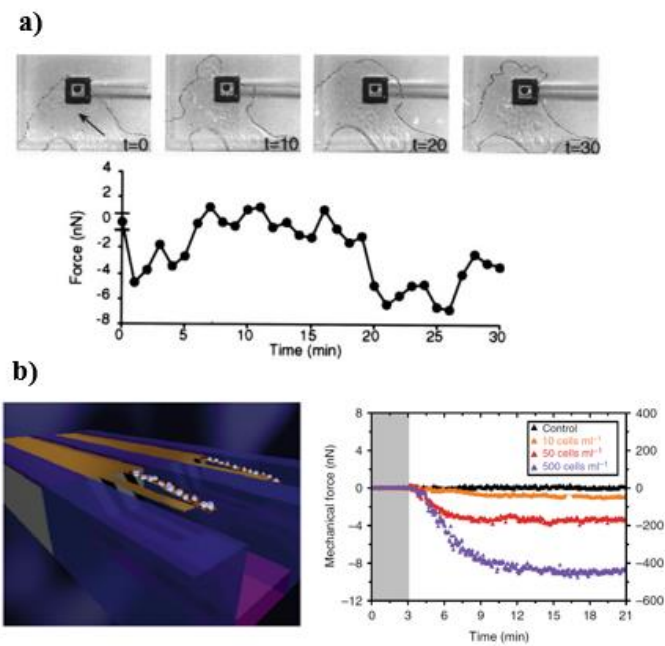


Figure 3.13: a) Micro-cantilevers to determine ventral traction forces as a function of time and compare them with dorsal measurements of fibroblasts (Sheetz, 1997); b) microcantilevers to investigate the effect of physical location of functionalization molecules on the detection of cells signal (Patil, 2018).

Recently, silicon-based nanomechanical sensors have been used to study the forces of living cells by recording in real-time the change in surface stress of the cantilevers. In particular, Etayash *et al.* in 2015 studied the deflection of the cantilever in the presence of living cells. They found that it was possible to detect the forces that occur when cells bind on the sensors⁸⁵. In 2018, Patil *et al.* investigated how the reproducibility of such deflection signals depends on the physical location of the chemically responsive regions (Fig. 3.13b). They developed a special structured functionalization to decipher important aspects of the transmission of mechanical forces over short and long length scales⁸⁹. Although several attempts have been made to improve the sensitivity of commercial nanomechanical sensors in liquids for the mass detection, there is a lack of studies that enhance their performance to detect the forces exerted by cells. Indeed, to improve their sensitivity the cantilevers should be smaller than cells, resulting in unreliable performances. Otherwise, very large and stiff

cantilevers or other microstructured platforms are needed to grow cells as *in vitro* substrates, to investigating the cell migration.

Chapter 4

Half-wet nanomechanical biosensors to investigate cancer cells adhesion and migration dynamic

3. Introduction

The design of the devices employed in this thesis arise from that one proposed by Oesterschulze and coworkers and described in detail in previous chapter. We adapted it to mechanobiology investigations such as the force tracking on living cell cultures. The device features have been changed for the specific requirement of the project, such as the cell seeding and culture protocols and the fitting with different microscopy set-up. The device design has been tuned consistently with the application change and material and specific fabrication and functionalization aspects have been introduced in the processes.

In order to demonstrate the potential of these devices to investigate cancer cells properties in term of adhesion, spreading and motility, two human breast cancer cell lines will be compared: the MCF-7 and the MDA-MB-231 triple-negative breast cancer cell lines, which exhibit representative epithelial-to-mesenchymal transition associated with breast cancer metastasis and are commonly used to study late-stage breast cancer.

The device consists of a series of cantilevers etched into a suspended silicon nitride membrane, separated by a micrometric gap. This architecture allows to keep one side immerse in a liquid environment, typically a cellular culture medium, and the other exposed to air and compatible with optical and electronic requirements. Based on this characterizing feature, I named this sensor family as “*half wet nanomechanical sensor*”, in the following referred as *HWN* sensors. The mechanical and mechanobiological features of HWN sensors showed that this approach allowed to highlight and quantify important mechanobiological

features that may have an impact on the development of new anticancer therapies. This work shows that the HWN sensors can be used to evaluate the adhesion and contraction forces of different cell lines and are a valuable tool for rapid and quantitative *in vitro* screening of new chemotherapeutic drugs that target cancer cell adhesion and motility.

4.1. Design of HWN sensors

As anticipated in the introduction to this chapter, HWN sensors consisted of rectangular cantilevers carved on a silicon nitride suspended membrane by the formation of a narrow gap. The membrane was supported by a silicon frame on all four sides. The formation of a water meniscus in the gap prevents the medium from leaking to the opposite side, which remains dry and is used to reflect a laser to measure the deflection of the cantilever. To explore a wide range of mechanical forces, the suspended microcantilevers of HWN were fabricated with three different lengths (50 μm , 100 μm , and 200 μm) and a width of 30 μm (Fig. 4.1a). The optimization of the half-wetting operation mode, reducing the leakage of solution through the cantilever gap (the wider the gap, the higher the leakage probability) and the elastic response of the meniscus (the narrower the gap, the stiffer the meniscus response), was accomplished by changing the gaps surrounding the cantilevers (2, 4, and 8 μm). The chip with the suspended cantilevers are shown in the following images collected by scanning electron microscope (SEM) (Fig. 4.1b, c).

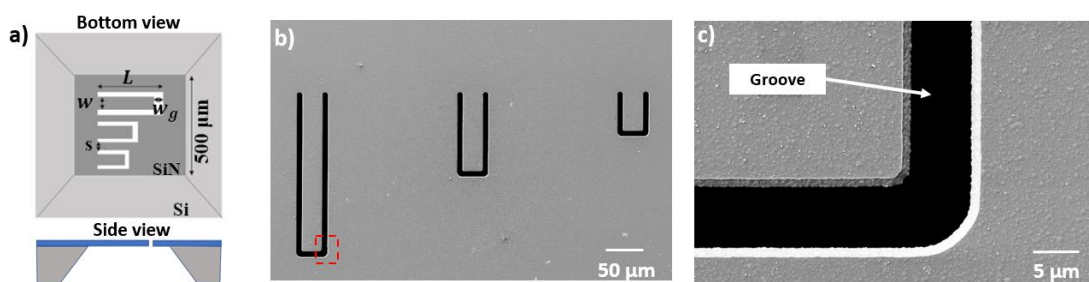


Figure 4.1: a) A schematic diagram of bottom and side view of suspended cantilevers; SEM image of suspended cantilever array etched on Si_3N_4 membrane: b) Cantilevers with 30 μm width, 4 μm gap, and 200 μm , 100 μm and 50 μm long, respectively; c) magnified view of the area identified by a red square (in the (b) panel) to highlight the gap area, as indicated by the white arrow.

4.2. Fabrication of HWN cantilevers

The chips with suspended cantilevers were fabricated using conventional micromachining approach and started from a 500 μm thick silicon wafer coated on both sides with a 2 μm thick low-stress LPCVD silicon nitride (Si_3N_4) film. At first, a 150nm thick chromium film was deposited on both sides by DC magnetron sputtering (Fig. 4.2a); a positive photoresist (MEGAPOSITTM SPRTM220 1.2) was spin-coated at 3500 rpm for 45 seconds on both sides (Fig. 4.2b) and pre-baked at 115°C for 1'30'' (Fig. 4.2c); a double-sided aligned exposure by standard proximity UV lithography (Fig. 4.2d) using two masks allow the resist patterning: the upper mask contains the markers and cantilevers pattern while the lower mask the structures for the windows definition (Fig. 4.3). After resist develop (Fig. 4.2e), the pattern was transferred into the chromium film by wet etching process (Fig. 4.2f), in a mixture of water, acetic acid (CH_3COOH), and ceric nitrate ammonium ($\text{CeNH}_4)_2(\text{NO}_3)_6$. Then the exposed Si_3N_4 was dry etched by reactive ion etching (RIE) for the windows structures using a mixture of CF_4/O_2 (150W, 100V bias) and by inductively coupled plasma RIE (ICP-RIE) (Fig. 4.2g) for the cantilever, using a mixture of $\text{SF}_6/\text{C}_4\text{F}_8/\text{O}_2$ (240W, 50V bias). First of all, I performed etching for the transfer of large window by RIE because, although the low anisotropy of the etching process, it allows higher etch rate. Then, I etched the top side containing the cantilevers by ICP-RIE, because it permits to achieve high anisotropy and better quality in term of verticality, necessary for the range of resolution and aspect ratio of the produced structures.

The Si_3N_4 cantilever were released by wet etching in KOH solution (30 wt %, 80°C) (Fig. 4.2h). Finally, the chromium mask was removed in etchant solution. It is important to stress here that gaps as narrow as 2 μm with a 2 μm thick membrane with an aspect ratio of 1 represent the smaller value achievable for a quasi-isotropic RIE process.

In the following, the Si_3N_4 surface that was previously in contact with the bulk silicon wafer will be referred as the “laser-side”, while the opposite surface will be referred as the “cell-side”, since it will be in contact with the cell medium where the cells will grow (Fig. 4.2I).

The chips were further cleaned in O_2 plasma oxygen (1 min, 40 W, Bias 100 V) and coated with a Ti-20nm – 50nm Au thin film by e-gun evaporation on the “laser side” to improve the laser reflectivity, that, as explained later, will be important for the detection sensitivity.

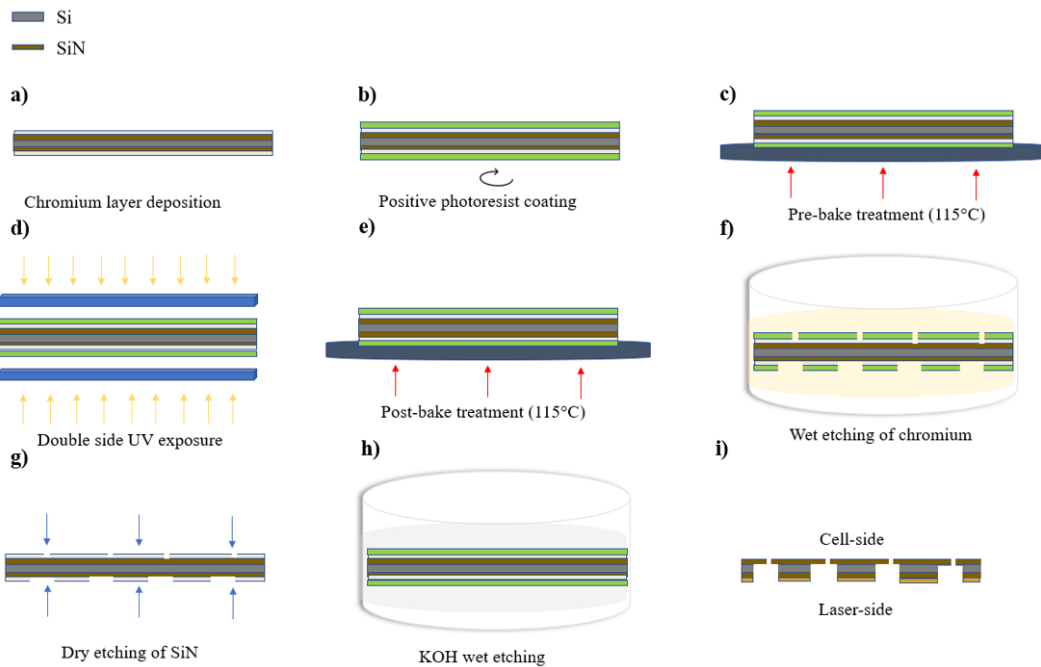


Figure 4.2: a) a 150nm thick chromium layer was deposited on both sides of a 2 μm thick low- stress LPCVD silicon nitride layer; b) SPR 220-1.2 photoresist is spin-coated on both sides of the wafer; c) pre-bake treatment is performed; d) double- aligned exposure by standard proximity UV lithography; e) exposure is followed by post-bake treatment; f) the protective chromium layer was removed by wet etching; g) the exposed Si_3N_4 layer is etched by reactive ion etching; h) the SiN cantilevers immersed in KOH are exposed; i) the cantilever side is referred to as the "cell-side" while the opposite side is referred to as the "back-side" and is covered with a thin gold layer.

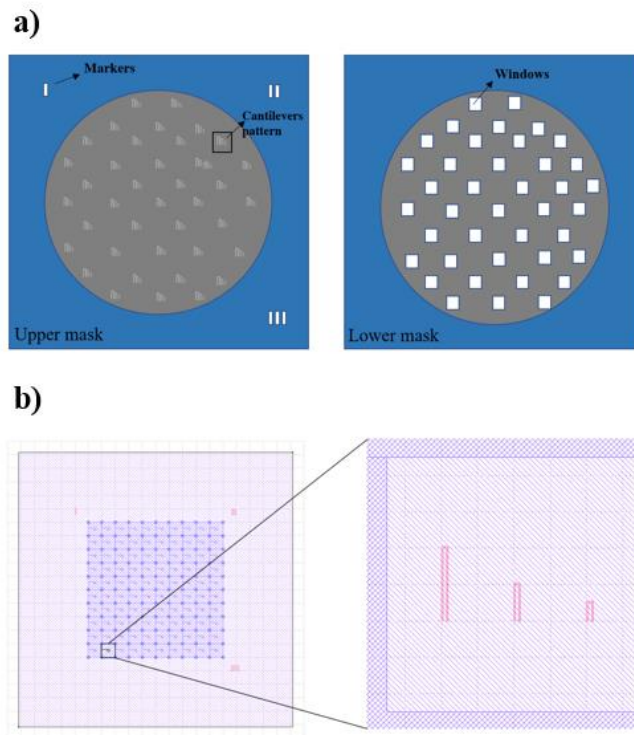


Figure 4.3: a) the upper (left) and lower (right) masks used for double exposure in the standard photolithography process; b) the GDS (Graphic Data System) file for the upper mask, showing the markers and pattern with the cantilever structures (enlarged on the right image).

4.3. Development of a chamber of measurements for HWN sensors

The configuration of our sensor requires that the cell side stay in contact with the liquid, while the laser side remains dry to enable the detection of the signal through an optical read-out. To operate properly the HWN sensors, I designed and developed a dedicate open liquid chamber (Fig. 4.4). In this chamber, the chip (Fig. 4.4a) is mounted on a suspended circular holder (Fig. 4.4b). The holder is then turned upside down, placed on the lid of a Petri dish and sealed with metal rings. This creates a cell that can be filled with the liquid with an overall volume of 650 μl (Fig. 4.4c). It can be used on an inverted microscope, so performing fluorescence optical microscopy, and compatible with the head of a JPK-NanoWizard II and Nanowizard 3 AFMs, so that the embedded laser detection system, used in the microscope to detect the AFM cantilever detection, can also be used to measure the deflection of the HWN sensor cantilevers (Fig. 4.4d).

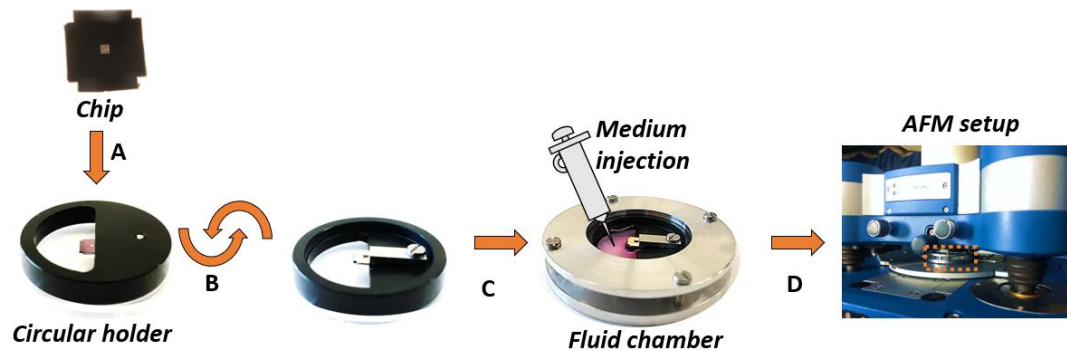


Figure 4.4: a) The chip with the fabricated cantilevers is mounted on the suspended circular holder with the bottom side facing up; b) the holder is turned upside-down, placed on the petri dish lid; and c) sealed by metallic rings, thus creating a liquid cell which is filled with the medium (650 μl final volume); d) the sealed fluid chamber is finally placed in an AFM setup.

4.4. Nanomechanical characterization of HWN sensors

To evaluate the forces exerted by the cells on the sensor, the static deflections caused by the cells, which are detected by optical readout (AFM-based), must be converted from an amplitude signal (V) to a force (N). This step requires calibration of the spring constant (k) and the sensitivity of the cantilevers.

In air and in liquid, the static spring constant (k) of the suspended cantilever does not depend on the size of the gap, while in the half-wet (HW) configuration the formation of the meniscus on the gap surrounding the cantilevers can add a further restoring force to the cantilever displacement, thus increasing the effective elastic constant of the systems. To quantify this effect, the cantilevers were calibrated in static mode both in air and in HW condition.

The spring constant of the fabricated cantilevers was calculated using a rectangular commercial cantilever NSC18/AIBS (μ Masch) as a reference probe with comparable length, width, and thickness, whose spring constant was previously evaluated using the thermal noise method^{104,105}. To perform the measurement, the reference cantilever was mounted on the AFM tip holder and the HWN sensor chip (with the suspended cantilevers) was attached to a glass coverslip with double-sided tape.

Calibration is performed by generating two force-displacement curves. First, the reference cantilever is pressed against a rigid surface (Si surface) to determine its spring constant k_{ref} and its sensitivity s_{ref} .

The second measurement is made by pressing the reference cantilever against the HWN sensor cantilever.

The spring constant of the HWN sensor cantilever (k_u) is evaluated by the following equation:

$$k_u = \frac{z_{ref}}{z_{tot} - z_{ref}} \times k_{ref} \times \cos^2(\theta)$$

Where, z_c is the deflection of the reference cantilever; z_{tot} is the total relative displacement; k_c is the spring constant of reference cantilever. Notice that $z_c = z_u + z_u$, where z_u is the deflection of the HWN sensor cantilever. The term $\cos^2(\theta)$ is a geometric correction for the tilt angle of the reference cantilever (15° tilt for our AFM). A sketch of the calibration procedure is shown in figure 4.5.

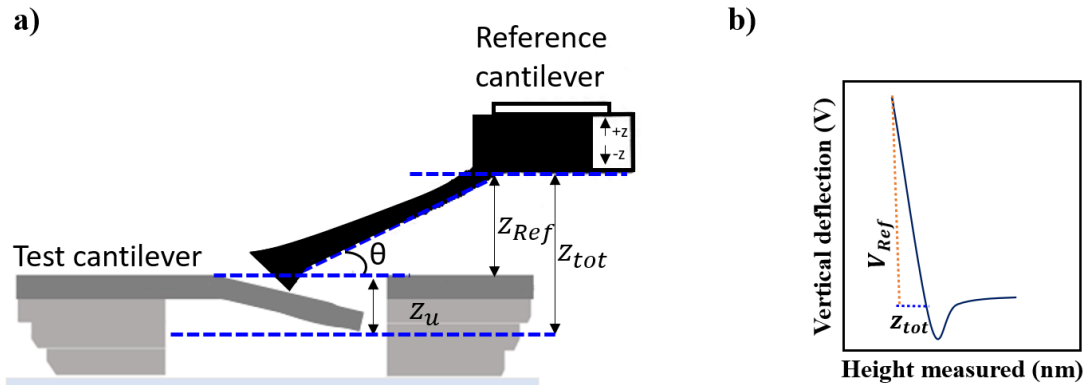


Figure 4.5: Graphical description of the approach to evaluate the spring constant of the HWN sensor cantilever. a) Schematic of the AFM set-up for measuring the spring constant of the HWN sensor cantilevers using a reference cantilever. b) Force-displacement curve (Height measured vs. Vertical Deflection) for the reference cantilever approaching the HWN cantilever. Using the force-displacement curve we can find the value of z_{ref} by multiplying the value of $V_{ref} \times S_{ref}$.

Finally, to convert the deflection of the HWN cantilever into a force value, we evaluate the sensitivity of the read-out system using the non-contact approach of the JPK- NanoWizard III AFM software which is based on Sader's theory and does not require the acquisition of a force-distance curve on a hard surface.

This method provides the inverse optical lever sensitivity (InvOLS) of the rectangular cantilevers from the thermal spectrum^{110,111}.

For the cantilevers with a length of 50 μm , we notice an extremely large variability of the k values both in air (82 ± 46 N/m) and in HW (138 ± 79 N/m) conditions which is probably results from the uncertainty in the positioning of the AFM tip of the reference cantilever on the edge of the tested cantilever, which is particularly relevant for shorter cantilevers.

Spring constants of (25 ± 6) N/m and (3 ± 1) N/m were obtained in air for the cantilevers with length of 100 and 200 μm , respectively. When measured in HW condition, for both cantilevers we observed a slight increase in k-values, which was larger for smaller gap sizes. The increase of the k-values when moving from the in-air condition to the HW-condition was evaluated for each cantilever, and then the ratio between the tow HW / AIR was plotted (Fig. 4.6). For the smaller gaps (2 μm and 4 μm) the stiffening induced by the water meniscus is relevant, up to an average increase of 70% of the k values in the case of 2 μm gap and 200 μm long cantilevers. For the 8 μm gap, the meniscus contributes with a 10% to the stiffness value, without a significant difference among 100 μm and 200 μm length.

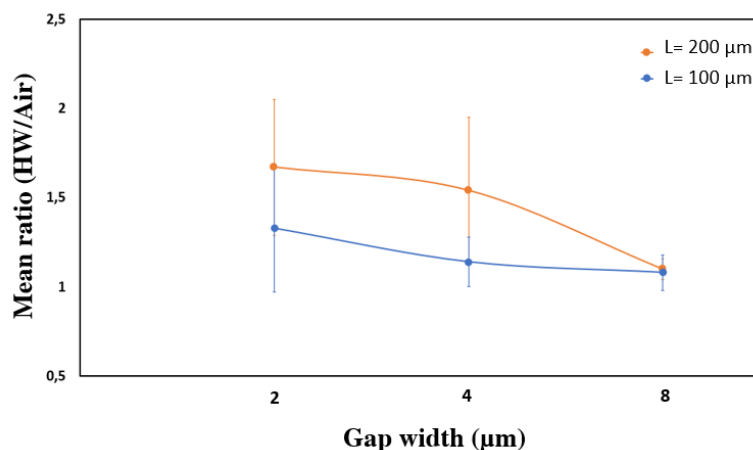


Figure 4.6: Mean ratio HW/AIR of spring constant values of the suspended cantilevers with different length as a function of the gap width obtained in air and half-wetting condition.

To evaluate the performance in dynamic mode, we performed resonance frequency measurements of our cantilevers in three different conditions: air, half-wet and fully-wet (in milliQ water). The cantilever resonance frequency was obtained using a home-built photothermal excitation system, integrated into a JPK- NanoWizard II AFM in the same three different conditions.

An excitation laser (375 nm, 70 mW) was focused on the base of the cantilever, the AFM built-in detection laser (780 nm) was then aligned on the tip of the cantilever and its reflection aligned on the AFM photodiode detector. For the half- wet condition, the chamber of measurements was filled with 650 μ l of milliQ water, while for full-wet condition the chamber is completely filled causing the cantilever to be immersed in liquid.

The resonance spectra obtained for the cantilevers of length 100 and 200 μ m are shown in Figure 4.7. In air, resonance frequencies of 240 kHz and 64 kHz were obtained, respectively. By fitting a Lorentz function to these spectra, a quality factor (QF) of 66 and 116 were obtained, respectively. In the half-wet conditions (HW), we observed a shift to lower resonant frequencies for both lengths, with peak values of 106 kHz and 30 kHz and a QF= 23 and 10.6 for cantilevers of 100 and 200 μ m length, respectively. In the fully wet condition (FW), the resonant frequencies were 48.8 kHz and 24.1 kHz, with 5.4 and 1.7 QF. Operation under the HW condition results in a decrease in QF of 3 and 10 times for 100 μ m and 200 μ m long cantilevers, respectively, which is significant but still allows the cantilevers to be used as mass detectors. In contrast, in FW condition the change in QF is dramatic, up to a factor 10^2 . Therefore, the HW configuration drastically reduces viscous damping, as also suggested by other authors¹⁰³.

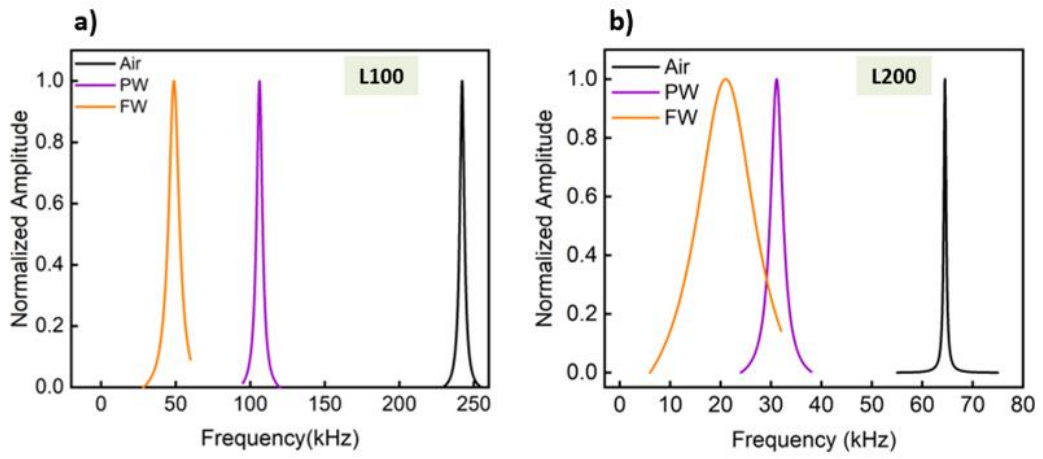


Figure 4.7: Normalized amplitude values of resonance frequency measurements for 100 μm (a) and 200 μm (b) long cantilevers as obtained in air, half-wetting, and full-wetting conditions.

4.5. Application of the HWN sensors to the detection of cancer cells

4.5.1. Cantilever functionalization

Any type of biosensor must be functionalized with appropriate molecules to facilitate cell interaction or adhesion. Such a procedure usually results in coating of all exposed surfaces for fully immersed cantilevers, which leads to cells growing on both sides of the cantilever^{69,100}.

As a result, either the presence of cells on the laser side may interfere with laser deflection or the cellular forces on the opposite side could balance each other, leading to misleading results. In order to restrict the cells growth to one side of the cantilever I developed a specific functionalization protocol to functionalize only one side of the cantilevers. The surface of the cell side surface of the HWN sensor is functionalized with 3-amino-propyl-triethoxysilane (APTES), an aminosilane commonly used in biosensors that creates a monolayer that exposes amino groups on the surface¹¹², which facilitates cell adhesion, as shown in several studies^{109,113–115}.

An alternative protocol based on vapor deposition to functionalize only the cell side of the sensor is applied, which leaves the back side of the cantilever free of impurities that could also interfere with laser reflection (Fig. 4.8). Specifically, the chips were fixed on a glass substrate with a Kapton tape (Fig. 4.8a), then subjected to a plasma O₂ process (1 min, 40 W, 100 bias) to clean the substrate and expose the silanol groups on the surface for the subsequent functionalization process.

A glass Petri dish filled with 300 μ l of APTES was placed on the bottom of a glass vacuum chamber (maintained at $1 - 10^{-1}$ mbar) and heated to 50°C. The sample was placed upside down 20 cm above the Petri dish and exposed to APTES vapor for 4 hours at 50°C in continuum vacuum (Fig. 4.8b). Finally, the chip was cured at 120°C for two hours in a separate vacuum oven (Fig. 4.8c).

The functionalization protocol was optimized based on the parameters found in the literature, which showed better adhesion of the Aptes when deposited at temperatures between 50-75^o^{116,117}. The curing after incubation with APTES is very important, enabling the formation of covalent bonds between APTES molecules to the hydrophilized surface¹¹⁸.

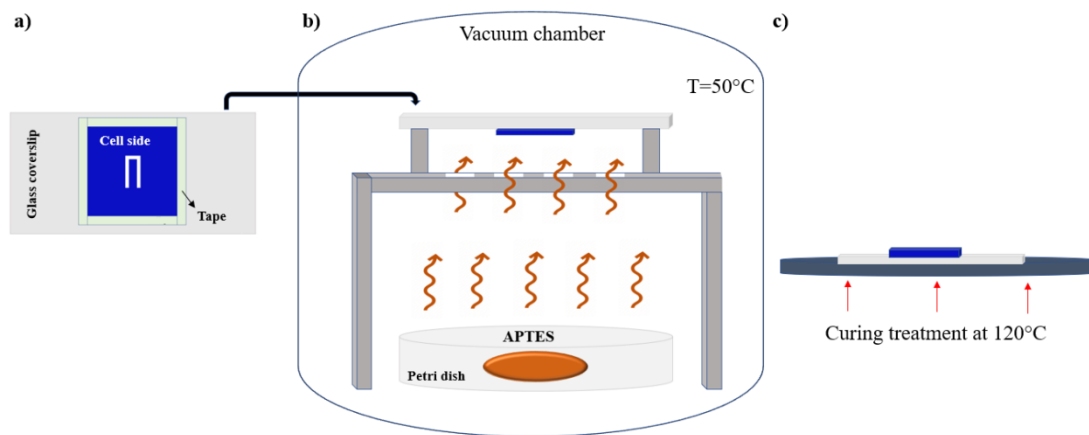


Figure 4.8: a) the chip (blue) with the top-side facing up is fixed on a glass coverslip with a tape and subjected to a plasma O₂ process; b) the coverslip is then placed backside down 20 cm above the Petri dish with APTES and exposed to silanes vapor for 4 hours at 50°C in continuum vacuum; c) afterward, the sample was underwent to the curing treatment at 120°C for 2 hours.

The functionalization of the cantilever was characterized by contact angle measurements (CA) (Fig. 4.9a) performed with a DataPhysics optical instrument OCA 15Pro (DataPhysics Instruments GmbH, Germany) at room temperature by adding 2 μ L Milli-Q water to the Si_3N_4 . The average CA values were determined by averaging over four different positions on three samples. We measured $(60 \pm 0.7)^\circ$ for the native SiN surface and $(79 \pm 3)^\circ$ one hour after the APTES coating. After 24 hours, the values showed a stable functionalization $(83 \pm 5)^\circ$. This result is consistent with the literature, as it has been demonstrated that the presence of the NH_2 groups of the APTES increases the contact angle of the silicon nitride surface compared to the native material¹¹⁹.

These value seems to be consistent with those found in the literature for APTES functionalization in a 10% v/v solution¹¹⁵. To evaluate the adhesion of cells to our chip after APTES functionalization, the number of MDA-MB-231 cells on the surface was determined by counting the cells 20 minutes after seeding (the same time used for experiments). The data showed better adhesion of cells on the Si_3N_4 surface after treatment with APTES compared to the untreated surface (Fig. 4.9b). Although higher hydrophobicity might be contrary to better cell adhesion, many studies in the literature have shown that surface energy is not the only feature that increases cell adhesion¹²⁰. In fact, the higher adhesion of cells can be explained by the presence of active $-NH_2$ groups on the Si_3N_4 surface.

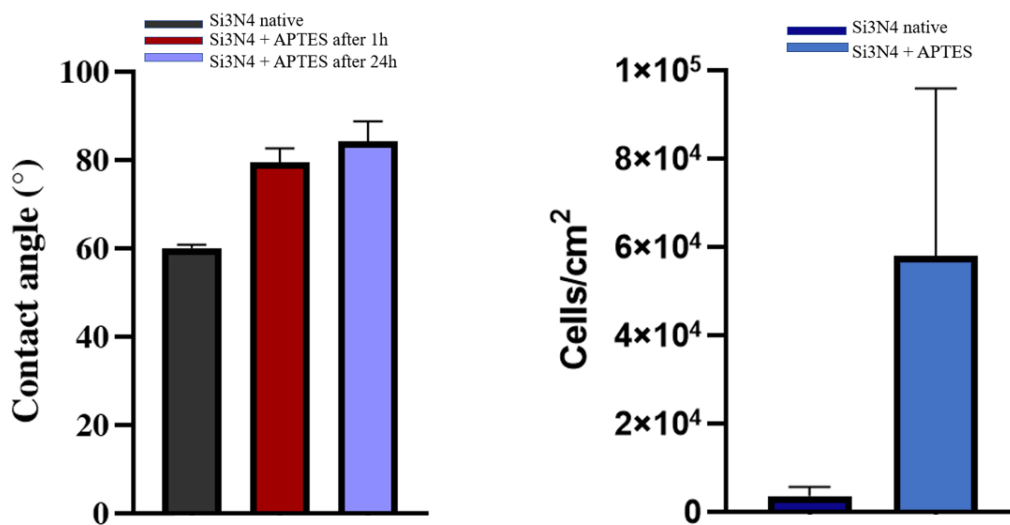


Figure 4.9: a) Characterization of APTES SAMs based on water contact angle on native silicon nitride (Si_3N_4) surfaces and 1h or 24h after APTES functionalization. Data show an increase in contact angle after functionalization and no significant change after 24 h of treatment as evidence of silane layer stability; b) Evaluation of functionalization efficiency for cell adhesion enhancement.

The morphology of the functionalized surfaces was also analysed by atomic force microscopy (AFM) (Fig. 4.10). When evaluating the roughness values, we found a decrease in surface roughness for the substrates functionalized with

APTES, from 4.3 to 4.1 nm compared to the value obtained with the native silicon nitride substrate.

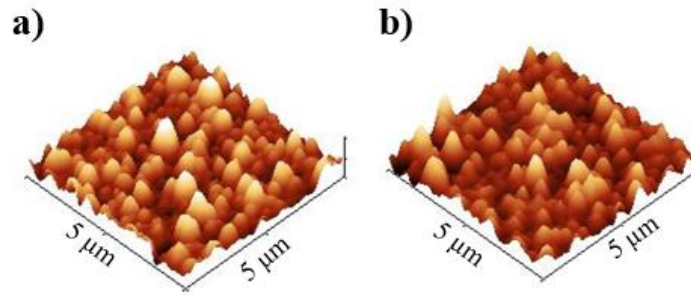


Figure 4.10: The 3D AFM images of surface morphology of Si_3N_4 surface before (a) and after (b) APTES functionalization. AFM images were acquired in AC mode in air on a MFP-3D-Bio instrument (Asylum Research/Oxford Instruments) with silicon cantilevers (Mikromasch, NSC19/AL BS with a nominal tip radius of ~ 8 nm and spring constants of $k = 0.6$ N/m ($f \approx 65$ kHz)). The 512x512 pixel images were acquired in a $5 \mu\text{m} \times 5 \mu\text{m}$ area. Here the scale in the vertical range is 30 nm.

Since the high roughness of silicon nitride surfaces makes it difficult to study the contribution of the APTES layer, I performed an in-depth morphological analysis on silicon surfaces (see Appendix).

This functionalization protocol was used also for the development of a novel bioassay platform, which was used as part of a collaboration with the Karolinska Institute. All the details are reported in the *Appendix section*. A more in-depth investigation of functionalized surfaces with APTES is there showed.

4.5.2. Cell lines and cell cultures

MDA-MB-231 (ECACC 92020424) and MCF7 (Sigma-Aldrich ECACC, #92020424) cells were cultured in a Dulbecco's modified eagle medium DMEM-high glucose, with L-glutamine and sodium pyruvate (Sigma-Aldrich), supplemented with 10% (v/v) of fetal bovine serum (FBS) (Sigma-Aldrich) and 1% (v/v) penicillin-streptomycin (EuroClone) at 37°C 5% of CO₂ incubator.

4.5.3. Experimental setup for living cells analysis

To use HWN sensors to monitor cell adhesion, spreading, and motility, the cell must be positioned on the cell side while the laser side remains dry. To perform the experiments with MDA-MB-231 and MCF-7 cells, I used the open liquid chamber described before. After the chip has been mounted on the suspended circular holder a 25 μ l droplet containing approximately 3.000 cells is placed on the top of the cantilever under sterile conditions (Fig. 4.11a) and incubated in a humidified atmosphere at 37°C and 5% CO₂ for 20 minutes to allow the cells to adhere while the back is kept dry (Fig. 4.11b). The holder is then turned upside down, placed on the lid of the Petri dish (Fig. 4.11c) and sealed with metal rings. The resulting liquid cell is filled with the medium (650 μ l final volume) (Fig. 4.11d) and mounted under the AFM head (Fig. 4.10e). In this way, the cell side of the cantilever with the adherent cells is in contact with the medium, while the formation of a meniscus in the gap prevents leakages over the back side where the laser beam of the AFM system is focused.

Cell position and movement were monitored by fluorescence images and time-lapse movies, which were acquired by a Zeiss AxioVert200 inverted microscope with a 20X objective and an XM10 camera (Olympus Corporation). Fluorescence images were acquired with an exposure time of 500 ms, while in time-lapse images were acquired every 30 seconds with an exposure time of 65 ms for a total time of 15 minutes. The images were then analyzed using ImageJ software.

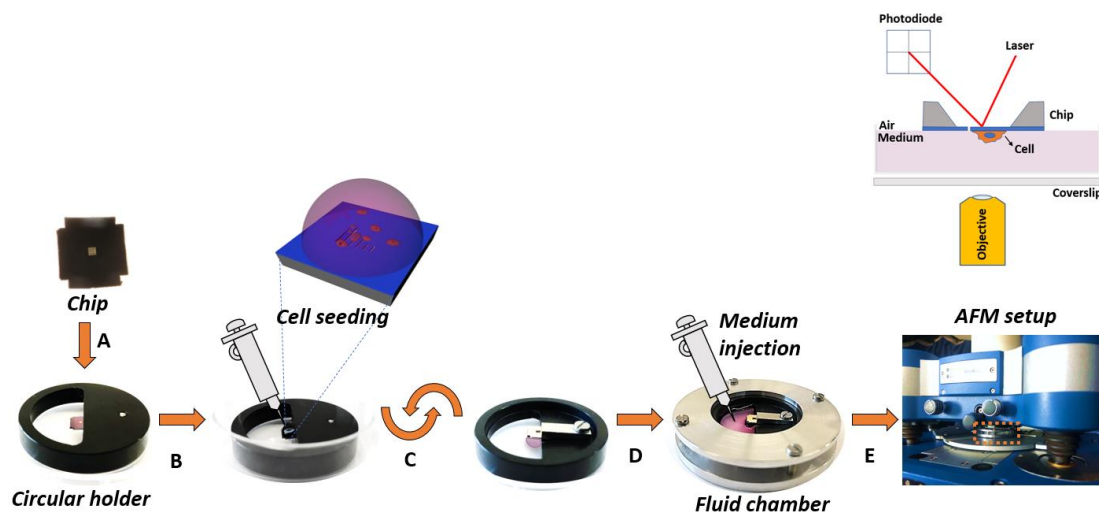


Figure 4.11: Graphical description of the assembly of HWN sensor with a liquid chamber for experiment with adherent cells: a) The chip is mounted on the suspended circular holder with the bottom side facing up; b) a 25 μl drop of cells suspension is placed on the chip surface and incubated for 20 min in incubator (37°C and 5% CO_2) to allow cells to adhere, while the top side (faced down) is kept dry; c) the holder is turned upside-down, placed on the petri dish lid; and d) sealed by metallic rings, thus creating a liquid cell which is filled with the medium (650 μl final volume); e) the sealed fluid chamber is finally placed in an AFM setup to detect the deflection signal. Moreover, the chamber is compatible with an inverted microscope to follow the migrating cells during the experiments.

4.5.4. Mass measurements of living cells on HWN sensors

The reduced effect on the quality factor achieved by the HW condition, is an important aspect to improve mass detection in liquids for biological applications. As a proof of concept, I evaluated the performance of HWN sensors measuring the mass of MDA-MB-231 breast cancer cells grown in adhesion on the cantilevers. The spectra acquired before and after the cells were deposited on a 4 μm gap and 200 μm long cantilever are shown in Figure 4.12: we observed a negative resonance shift induced by the presence of the cells. A shift of 0.8 kHz and 1.3 kHz was observed for the presence of $n > 10$ cells and (Fig. 4.12a) and 5 cells, respectively (Fig. 4.12b). The presence of cells on the gaps could add a further stiffening contribution which may compensate the frequency shift induced by the added mass^{54,70}. As is well known, the resonance frequency shift generally depends on the position of the cell on the cantilever and the surface tension applied to the cantilever by the adhesion and migration process of the cells^{62,63,80,102,121,122}. Since living cells move constantly on the sensor surface, and their position and the exerted forces change from measurement to measurement, it is not possible to accurately determine the cell mass. An estimate of the single-cell mass was made assuming a uniform distribution of cells along the cantilever and in the gaps. To determine the value of the resonant frequency, the frequency curves were fitted with Lorentzian functions. The corresponding values of the resonance peaks were used to calculate the additional mass due to the presence of cells in dynamic mode, as described in the literature^{121,123}. The results showed an additional mass of 0.1 ng for the cantilever with 5 adherent cells. The value of mass was ~ 0.02 ng/cell. This value is about 10-100 times lower than the mass of single cells measured in the literature^{96,123,124}. This result confirms that the stiffening contribution of the cells on the gaps affects the measure of mass.

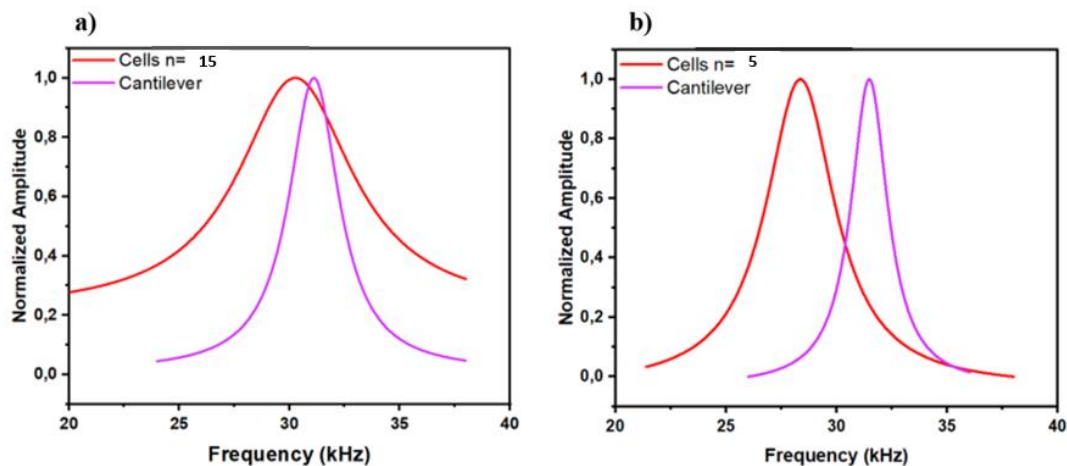


Figure 4.12 : The graph shows the normalized amplitude value of resonance frequency measurements in absence (violet) and in presence of $n > 10$ cells (a) and $n = 5$ cells (b) as obtained in half-wetting condition.

4.5.5. HWN sensor to investigate cancer cell motility and exerted forces

To investigate cell motility and adhesion forces, cantilevers with 200 μm length and gap size of 2 μm and 4 μm were used, because the force sensitivity improves with lower spring constants⁶². The gap size of 8 μm was not suitable for these experiments, since we frequently observed that the cells somehow remained trapped in the gap, leading a decrease in their motility. The deflection curves in presence of cells, acquired using the "real-time" oscilloscope mode of NanoWizard II AFM (JPK Instrument, AG), can be converted into forces by using the values of k and sensitivity obtained for the cantilever in HW condition (see the calibration section).

We measured the dynamic deflection of the same cantilever before (Fig. 4.13a) and after (Fig. 4.13b) MDA-MB-231 cell adhesion under HW (blue traces) and FW (red traces) conditions. In absence of cells the signal amplitude is larger in the FW conditions, indicating that the presence of the medium also on the laser side perturbs the read-out adding an extra noise contribution. When cells are

present on the cantilevers, the signal amplitude remains the same, but the deflection variation induced by the cell motion appear much larger on the cantilevers operated in HW conditions. Since cell behaviors on the cell side of the cantilever cannot be influenced by the presence or not of culture medium on the laser side, we can conclude that HW condition offer a much larger sensitivity to cell-induced deflection.

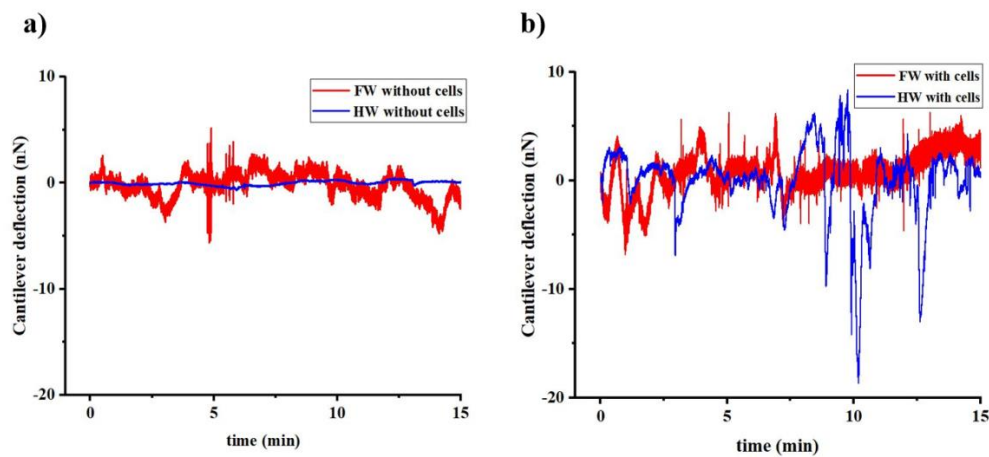


Figure 4.13: Deflection signal recorded in half wetting (blue curve) and in full wetting conditions (red curve) for the same cantilever in absence (a) and in presence (d) of MDA-MB231 cells.

To better assess the variation of the signal over time, we performed the moving variance analysis (Fig. 4.14). The moving variance was obtained by calculating a variance value for intervals of 100 milliseconds. Each value is plotted as a function of time. Due to the higher damping, the FW configuration was able to follow much faster variations. In fact, the moving variance showed significant differences when the time interval for which the value is calculated is of the order of Q/f , i.e., ~ 60 ms and ~ 300 ms for FW and HW, respectively. By using these values, the moving variance analysis showed that the difference between the cantilever before (top) and after cell adhesion (bottom) is less remarkable in FW condition (Fig. 4.14a) than in HW (Fig. 4.14b). Indeed, in FW the spurious peaks, likely due to cellular debris or other factors interfering with the laser path, complicate the interpretation of the signal after cell

adhesion. At longer time intervals of moving variance (3 seconds) we can see an increase in the values after cells adhesion in HW condition (Fig. 4.14c, blue traces), while in FW condition (Fig. 4.14c, red traces) we observe a decrease in the variance signal because of the higher damping. All together, these data confirm the highest sensitivity of the sensors operating in half-wet conditions.

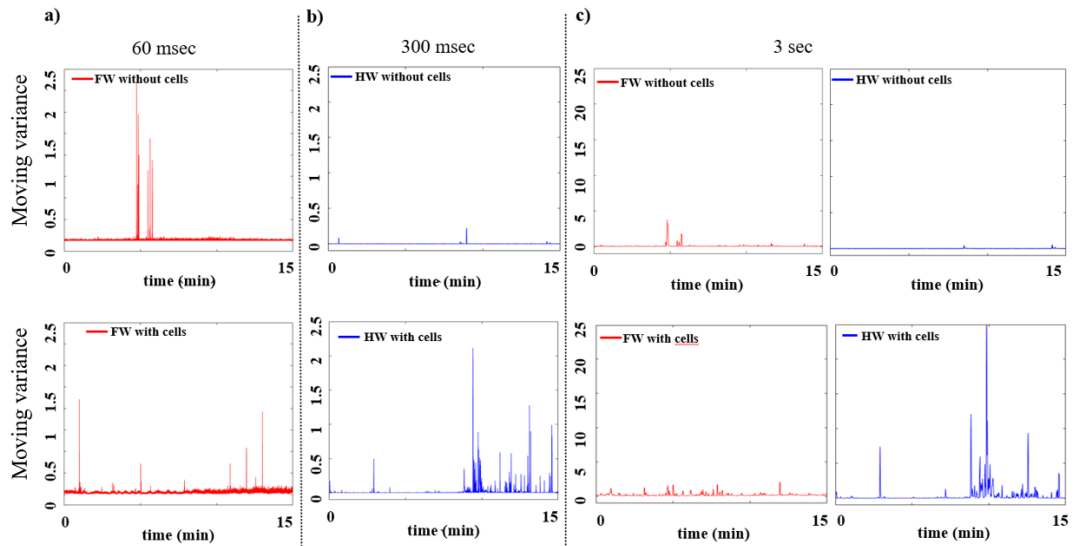


Figure 4.14: The corresponding moving variance analysis of deflection signal (Fig.6 a and b) recorded in half-wetting (HW) (blue curve) and in full-wetting (FW) (red curve) is shown in absence (at the top) and in presence (on the bottom) of cells, at three different time intervals: 60 ms (a), 300 ms (b) and 3 sec (c). The time interval was chosen according to the ratio between the quality factor and the resonance frequency of the sensor. In FW condition, it is possible to notice the presence of spurious peaks also without cells, as demonstrating the possibility to signal disturbance during analysis. Moreover, for higher time interval to analyse, due to the higher damping, the FW condition is not able to highlight variance changing compared to the HW one.

To check the potential of the HWN sensors as a test of cancer malignancy the same experiment were performed with a less aggressive breast cancer cell line: MCF-7. A comparison of the deflection signal of the cantilever before and after cell incubation (Fig. 4.15) shows that, when cultured on the HWN sensor, MDA-MB-231 cells (Fig. 4.15a, in red) exhibit much higher forces than MCF-7 cell (Fig. 4.15b). In order to associate the recorded forces with the cellular motion, I recorded a time lapse movie simultaneously to the deflection measurements. The cells move and spread on the cantilever surface and across the gap.

To quantify in a more rigorous way the forces developed by the cells, we performed the analysis of the variance over the entire measurements period. Indeed, the variance does not account for static deflection, while attributes the correct weight to rapid cell pulsation that would be lost by force averaging. The vertical deflection signal was recorded at a sampling frequency of 1 kHz for 15 minutes. During the measurements, the temperature of the setup was monitored and maintained at $30^{\circ}\text{C} \pm 1^{\circ}\text{C}$. Before analysis, the thermal drift was subtracted from the data by linear flattening. The cantilever deflection of the resulting curves was then converted to force using the cantilever spring constant and the sensitivity previously evaluated.

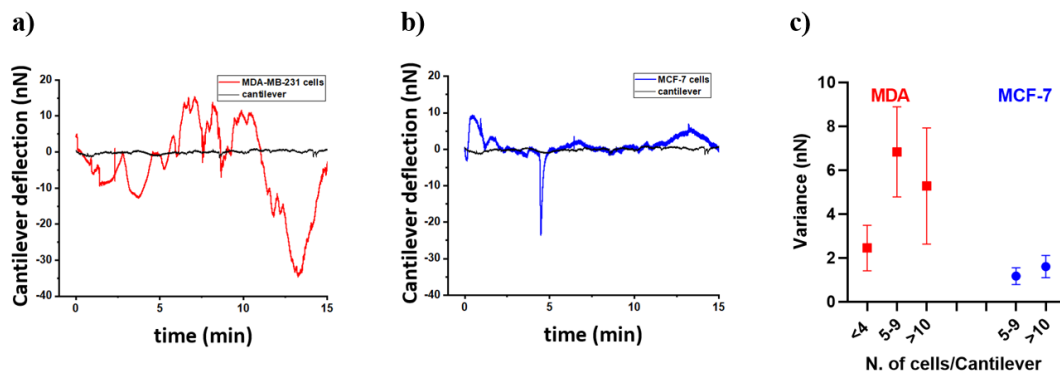


Figure 4.15: Deflection curves as function of time for bare cantilevers and in presence of MDA-MB 231 (a) or MCF7 cells (b) recorded in HW conditions. (c) Variance values obtained for the cantilevers of 200 μm of length and 2 μm of gap size grouped according to the number of cells adherent to the cantilever: for MD-MB231 ≤ 4 cells $N=3$; 5-9 cells $N= 6$; >10 cells $N=4$, for MCF7 5-9 cells $N= 5$; >10 cells $N= 5$.

In the analysis of variance, we classified the cantilevers according to the different number of cells adhering on the sensors. To this purpose, the nuclei were stained and by using the fluorescence microscopy we counted the number of cells on the cantilever and across the gap (as shown in Fig. 4.16).

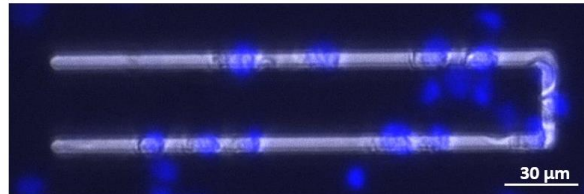


Figure 4.16: an example of fluorescence image acquired on MDA-MB-231 cells (stained with NucBlue) during migration analysis.

As expected, the variance is larger when a higher number of cells is present on the cantilever surface. As can be seen in Figure 4.15c, the variance relative to MDA-MB-231 is much larger than that relative to MCF-7, suggesting the former exert larger forces during migration, adhesion, and contraction process. This is consistent with the data from the literature¹²⁵ and with the scratch wound assay, which showed that MDA-MB-231 have higher mobility than MCF-7 (Fig. 4.17), which is consistent with their high potential ability to metastasize.

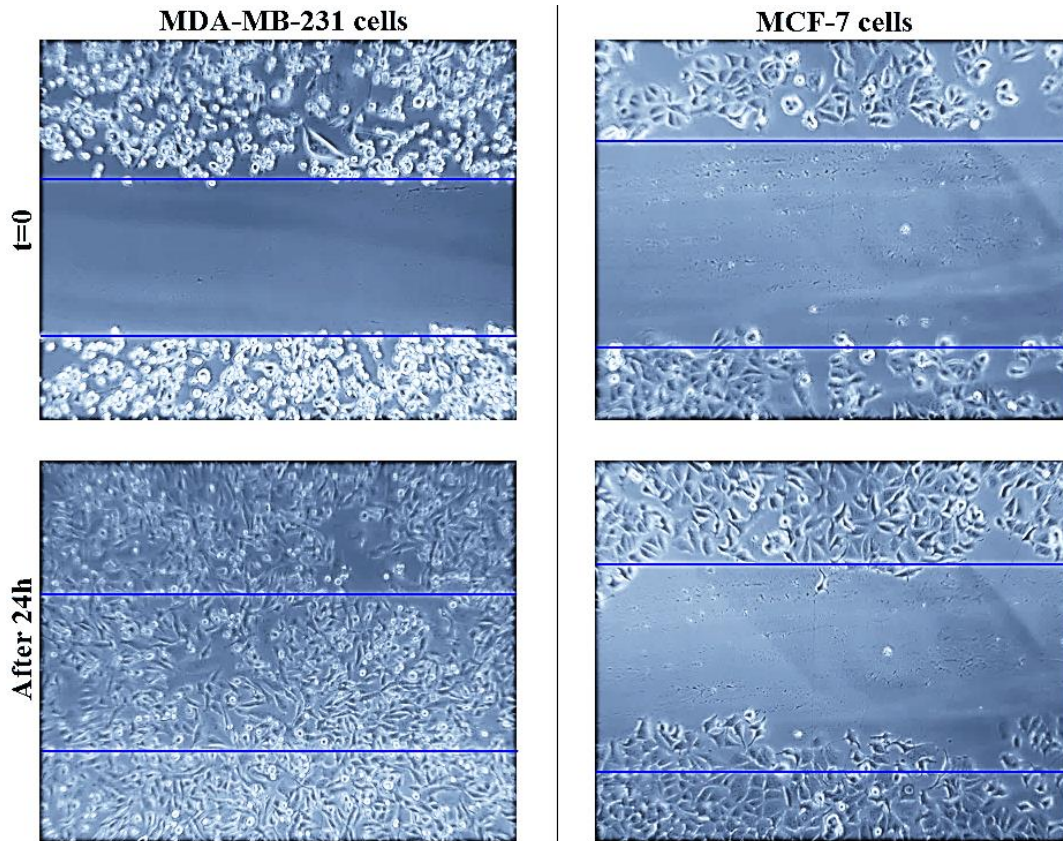


Figure 4.17: Scratch wound healing assay for MDA-MB-231 cells and MCF-7 cells. Cells were starved with medium with 1% (v/v) FBS for 20 h. Afterward, a scratch was made on each well by a micro-pipette tip and images were acquired at $t=0$ and after 24 h. The images show that after 24h the MDA-MB-231 cells cover completely the entire cross as respect to the MCF-7 cells.

Scanning electron microscopy (SEM) was performed with LEO 1540XB (Carl Zeiss AG) on HWNs after fabrication process to characterize the resulting cantilevers and after experiments with cells to assess cells adhesion and position on the cantilever if on plane surface or across the gaps, and to perform morphological analysis. To perform the morphological analysis, the medium was removed at the end of the incubation time and the cells rinsed with Phosphate-buffered saline (PBS). The cells were fixed in 4% paraformaldehyde for 20 minutes, at room temperature. After incubation, they are rinsed in PBS and then dehydrated in graded ethanol, dried, and coated with a thin layer of Au/Pd. SEM images acquired after measurements confirmed the position of the cells on the sensors indicating also a strong adhesion that withstood washing

and fixation procedures required by SEM sample preparation protocols (Fig. 4.18).

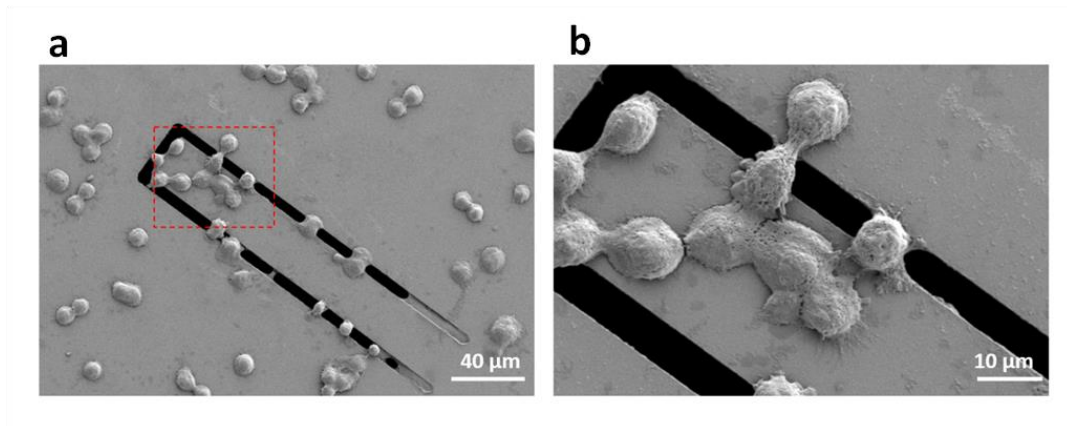


Figure 4.18: SEM images of cell adherent on cantilever with a length of 200 μm and a gap size of 4 μm after deflection measurements. Representative SEM image (a) and zoomed view identified by the red square (b).

4.5.6. Analysis of the variance as a function of cell position along the cantilever

To further investigate the effect of cell positioning on the force generated, I grouped the cantilever according to three different positions of cells (both MDA and MCF7) along the cantilever: 1) the majority of the cells lay in the apical region ($> A$); 2) the majority of the cells lay in the basal region of the cantilever ($> B$); 3) cells are equally distributed on the apical and on the basal region of the cantilever ($A=B$), as described in the scheme (Fig. 4.19a). The analysis of variance of the deflection signal showed an increase when the majority of the cells are in the apical zone compared with the basal zone. This result suggests that the apical zone may be the most sensitive zone of the cantilever, which is consistent with the literature¹²³. When the cells are evenly distributed on the apical and basal zones, the signal is lower compared to the situation when cells are in the basal zone, suggesting that this positioning balances the system and

reduces the detectable oscillations (Fig. 4.19b).

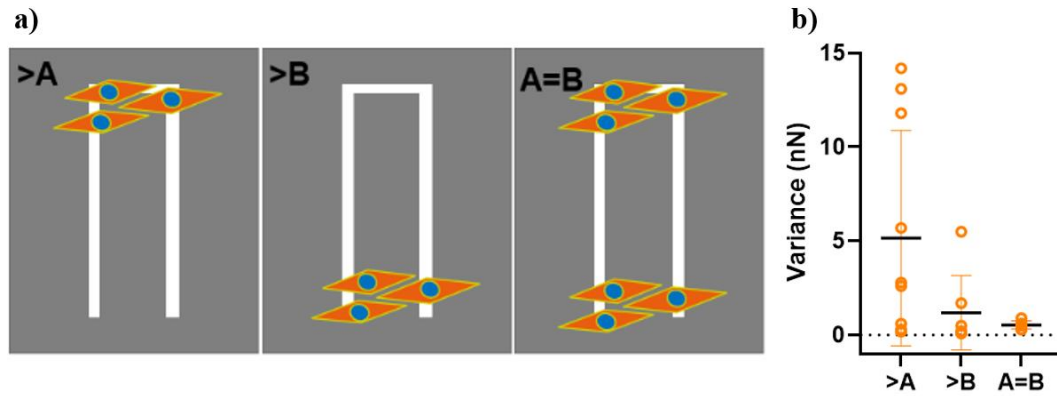


Figure 4.19: The positioning of cells along the cantilever influences the force signal generation. a) Schematic of arrangement of cells (MDA and MCF-7) with three different combinations: a higher number of cells in the apical region (>A) or in the basal one (>B); an equal number of cells in the apical and basal zone (A=B). b) Analysis of variance (nN) of the oscillation signal shows a different outcome in function of the different cells positioning. In details, a higher number of cells placed on the apical region cause an increasing in the variance values than the basal positioning. Moreover, if cells are equally distributed in the apical and basal zones, the signal decreases as indicating how the presence of cells on the opposite part of the sensor could balance the system reducing the oscillation.

To compare the two cell lines, we also analyzed the variance as a function of the position of the cells in the apical or basal zone. We found that MDA-MB - 231 cells had higher variance values in both the apical and basal zones than MCF -7 (Fig. 4.20a). Finally, for the samples where the majority of cells lay in the apical zone, we analyzed the variance for both MDA and MCF -7 as a function of the number of cells, finding a linear correlation between variance amplitude and number of cells, indicating that by evaluating the variance, we actually sum up the force contribution provided by every cell, even if they act randomly and independently (Fig. 4.20b).

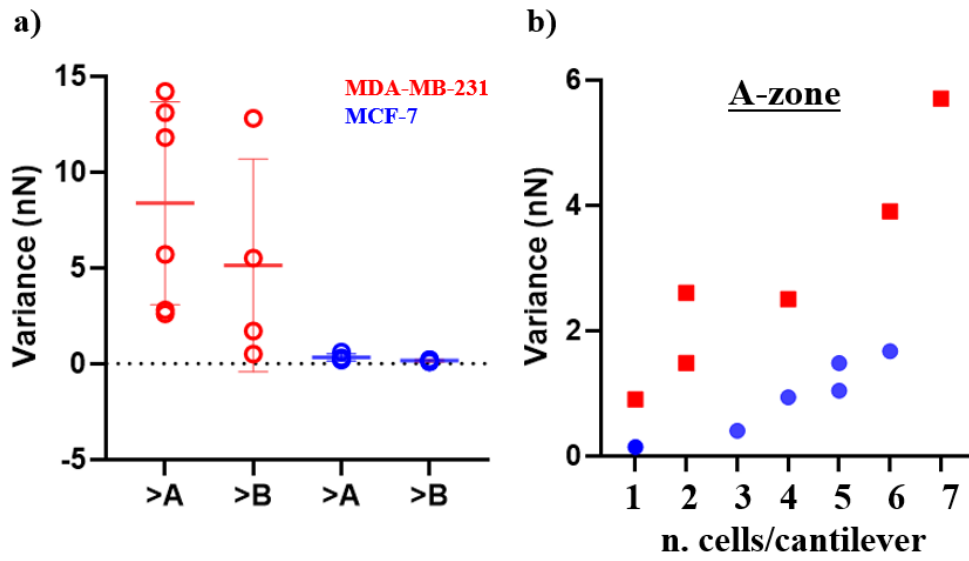


Figure 4.20: The variance analysis of oscillation signal in function of cell positioning for different type of cells (MDA or MCF-7). a) The MDA-MB-231 cells showed higher variance values both on the apical or basal zone if compared to MCF-7 ones; b) the analysis of variance for MDA and MCF-7 placed only on the apical zone (the most sensitive zone) showed higher values consistent with the number of cells.

4.5.7. Macro- and micro-oscillation analysis

Upon further investigation of the forces exerted by the cells on the cantilever, we find that the deflection curves exhibit macro- and micro-oscillations. First, we sampled the data set of the curve (one point every 100) and then performed smoothing using the average of 500 neighboring points. In the resulting baseline curve, the peaks and minima are identified as macro-oscillations. Then the same baseline curve is subtracted from the data curve to obtain additional peaks and minima, which are identified as micro-oscillations (see Fig. 4.21). All data processing and analysis was performed using Matlab R2019a and OriginPRO2021b software.

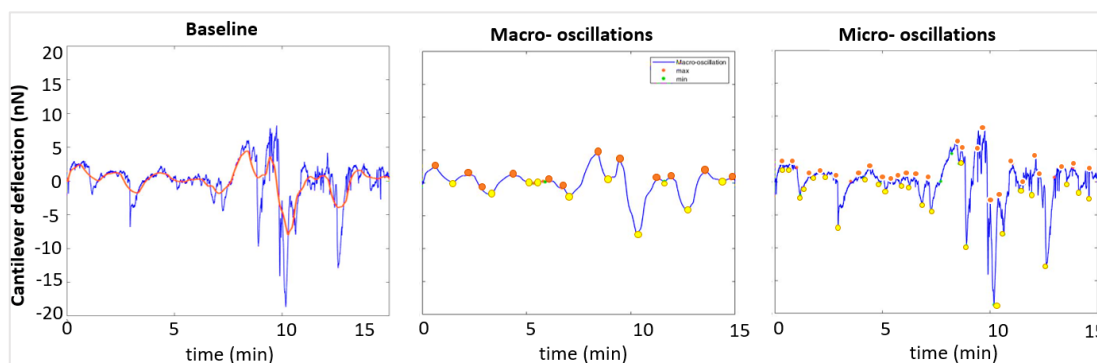


Figure 4.21: Example of the cantilever deflection converted into force for MDA-MB-231 cells adherent to the HWN sensor. The macro-oscillations of the cantilever can be identified (red line), while other small oscillations are present as shown by the data curve (blue curve) (a). Yellow and red dots identify the peaks of macro-oscillations (b), and micro-oscillations (c).

Both oscillations can be attributed to the cells adhering to the cantilever and moving on it or across the gaps, exerting a contractile force that deforms the cantilever. The forces corresponding to these oscillations were evaluated. The results for MDA-MB231 and MCF7 are compared in Fig. 4.22, where the cantilevers are grouped by the number of cells. The force values obtained for

macro- and micro-oscillations appear to be generally broadly distributed for MDA-MB231 compared to those observed for MCF7. The median force values for macro-oscillation of MDA-MB231 are 1.8 nN for ≤ 4 cells, 0.96 nN for 5-9 cells, and 1.6 nN for > 10 cells; while for micro-oscillation, 2.3 nN for ≤ 4 cells, 1.3 nN for 5-9 cells, and 1.8 nN for > 10 cells were obtained. These median values for cantilevers with a number of more than 10 cells are higher than those obtained for MCF7: macro-oscillations 0.65 nN for 5-9 cells, 0.40 nN > 10 cells and for micro-oscillations 1.0 nN for 5-9 cells, 0.79 nN for > 10 cells. These force values are compatible with those observed in single cell adhesion measurements by atomic force spectroscopy¹²⁶. They are also consistent with studies performed using traction force microscopy, which have shown that metastatic cells in breast cancer models exert significantly greater traction forces than non-metastatic cells^{14,40}.

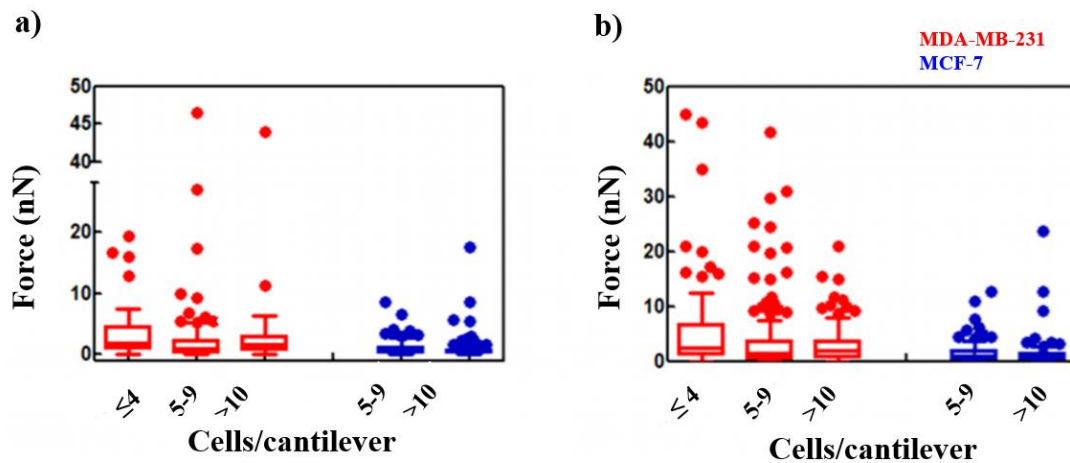


Figure 4.22: Forces correlated with the macro-oscillations (a) and micro-oscillations (b) obtained for MDA-MDA231 and MCF7 grouped according to the number of cells adherent on the cantilever.

The higher values observed in the dispersed distribution are most likely due to the contribution of multiple cells moving and contracting or releasing simultaneously on the cantilever. The widely dispersed force values for MDA-MB231, especially for the micro-oscillations, could reflect a different mechanism of force transmission at the adhesion sites between the two cell lines, with a variation in cell spreading or even a different number of adhesion sites formed in the initial phase of adhesion, but this should be further investigated. These results suggest that the HWN sensors could be a valuable tool for analyzing the force exerted by the cell during the adhesion or migration process and to monitor the effects of drug treatment on such processes in real time.

Chapter 5

Half-wet micropatterned substrates for the investigation of cancer cell migration

5. Introduction

In this chapter, we propose a novel 2D substrate, derived from the architecture developed for the HWN sensors that could, in principle, separate the effects of physical confinement, stiffness and curvature experienced by tumor cells as they migrate, and offer an alternative approximation of the ECM micro-tracks in which tumor cells migrate *in vivo*.

The experiments performed with HWN, described in the Chapter 4, showed that cells locate preferentially on gaps between the suspended cantilever and the membrane, where they also seemed to have a higher motility. Since the presence of meniscus has been demonstrated by the diverse mechanical behavior of the cantilevers in the HW condition as function of gap size, I wondered what the features of the meniscus are formed at the interface air-liquid that attract cancer cells, among the curvature, the surface tension, the absence of a steady anchoring structure, the access to the liquid medium all around the cell, or what else.

The device consists of a chip, as shown in the previous chapter, on which multiple micro-gaps were fabricated. Instead of being used as sensors, the chip was placed in a upright chamber of measurement to allow breast cancer cells to grow on the microstructures. I analyzed the effect of these structures on the morphology of MDA-MB -231 breast cancer by different microscopy techniques and their effect on cell motility by live cell imaging. A preliminary comparison with the behavior on the same substrate of a less aggressive cancer cell line, the MCF -7 cells is also reported.

5.1. Design and fabrication of half-wet micropatterned substrates

The topographic features of the ECM consist of a mixture of fibers, ridges, and sub-micrometer pores^{32,127}. Recently, it has been shown that the growth and morphology of cells vary as a function of geometrical features of the substrates on which they grow. In particular, cells can pass through the pores and channels of the ECM, provided that the diameter of these structures is not smaller than the 10% of the cross-sectional area of their nucleus^{28,32}. Based on these values, in the “*trans-well assay*” (described in the Chapter 2), the most widely used method to analyze the invasiveness of cancer, it is reported that cell populations easily diffuse through membrane pores with sizes between 3 and 12 μm ¹⁰. Moreover, most migration studies were performed on cancer migrating cells with channels, gaps and ridges ranging from 2 to 50 μm in diameter^{127,128}. To better mimic the topographical features of the ECM and study its effects on the migration of MDA-MB-231 and MCF-7 cancer cells, I decided to create rectangular gaps 2 μm , 4 μm , and 8 μm wide and 150 μm long. For each chip, I created a pattern of 4 arrays, each containing 3 gaps spaced 50 μm apart. The 2 μm wide micro-gaps are well below the physical nuclear boundary, while 4 and 8 μm wide ones are comparable to it. Larger widths were excluded to avoid leakage through the gaps and to ensure the half-wet configuration.

Furthermore, since the fiber-like pathways that cancer cells can create and follow during their migration through the tumor microenvironment range from 100 to 600 μm ^{28,32}, I chose a length of 150 μm , that have been commonly adopted in previous studies on migration of breast cancer cells¹²⁹. Using this length, I created an array composed of 12 micro-gaps for each Si_3N_4 chip, thus increasing the size of my dataset with a better statistical analysis.

To fabricate the micro-gaps, I performed two lithographic processes on a Si_3N_4 substrate: standard lithography and electron beam lithography (EBL). First, I performed standard lithography with double mask alignment and exposure, as described in the previous chapter for the HWN cantilevers.

Unlike the HWN sensor fabrication process, here I transferred only the markers (that will be useful for the following EBL processes) of the upper mask and the windows of the lower mask, by wet etching of the chrome, as shown in Figure 5.1a.

At this point, I continued with maskless EBL lithography by covering only the top of the wafer with positive e-beam resist ARP-679-0.2 and using the etched markers to align the pattern of the microstructured gaps (Fig. 5.1b) with the windows already developed during the previous lithography process. After exposing the wafer, I developed the structures and dry etched them as done with the HWN sensors. Finally, the chips with the final microstructures were characterized by SEM (Fig. 5.1c).

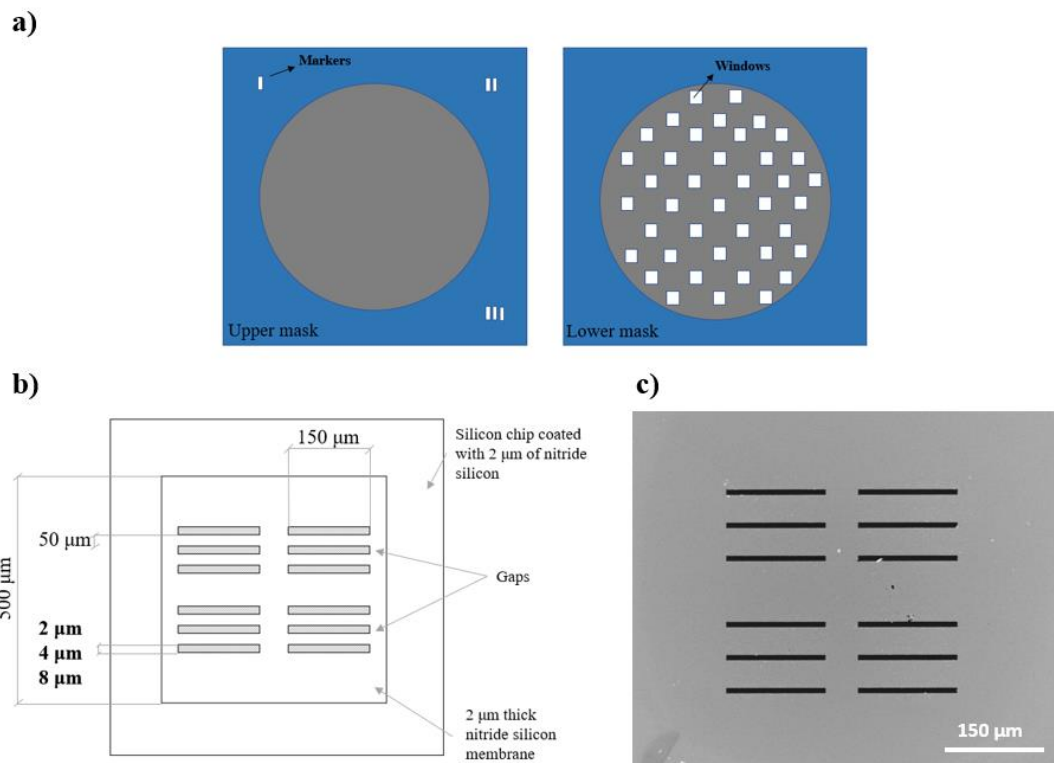


Figure 5.1: (a) schematic of the lithographic transfer of the markers (from the upper mask) and windows (from the lower mask); (b) an example KLayout file showing the final pattern of microstructured gaps; (c) SEM image of the array of microstructured gaps (8 μm width) on the Si_3N_4 membrane.

5.2. Experimental set-up for cancer cell migration analysis on HW micropatterned substrates

To ensure the half-wet configuration, cells must be seeded on the top side of the chip and immersed in the liquid, while the bottom side beyond the gap is kept dry (as for HWN sensor). The liquid-air interface across the gaps is required to create the meniscus which is then used as topographical feature to mimic a confined and curved space (Fig.5.2). For this reason, the medium is placed only on the top of the micro-gaps. To this purpose, I designed and developed a special chamber of measurement compatible with an inverted microscope equipped with live-cell imaging setup.

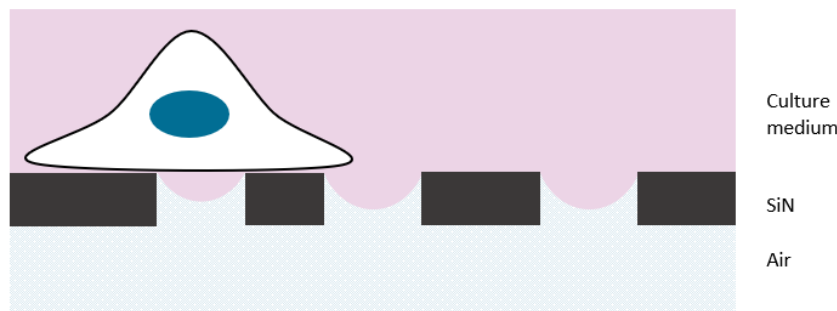


Figure 5.2: Schematic of the cells grown on the micro-gaps and experiencing the half-wetting configuration.

The chamber of measurement consists of a commercial Petri dish in which we cut 4 holes with a diameter of 2 mm using a CO₂ laser cutter. The size of the holes was chosen to amply match the size of the silicon nitride windows (large 500 x 500 μm) on the bottom of the chips.

The holes are used to place the chips (with the micro-gaps arrays) on top and to keep the side above the gaps dry. Indeed, initial attempts to attach the chips directly to the petri dish without holes resulted in condensation on the bottom of the chips during incubation at 37°C, which could compromise the desired half-wet configuration for live cell experiments (as described below).

Each chip containing the micro-gaps was aligned to each hole of the petri dish

and glued using ReproRubber ® ThinPour. To ensure sterility throughout the entire experiments, the Petri dish with the holes is covered with a Petri cap (to avoid any contaminations during the transfer of the device from incubator to the live cell imaging set-up) and a PMMA ring with a diameter of 2 cm and a height of 3 mm is placed between the cap and the Petri dish with the holes (Fig. 5.3a, b).

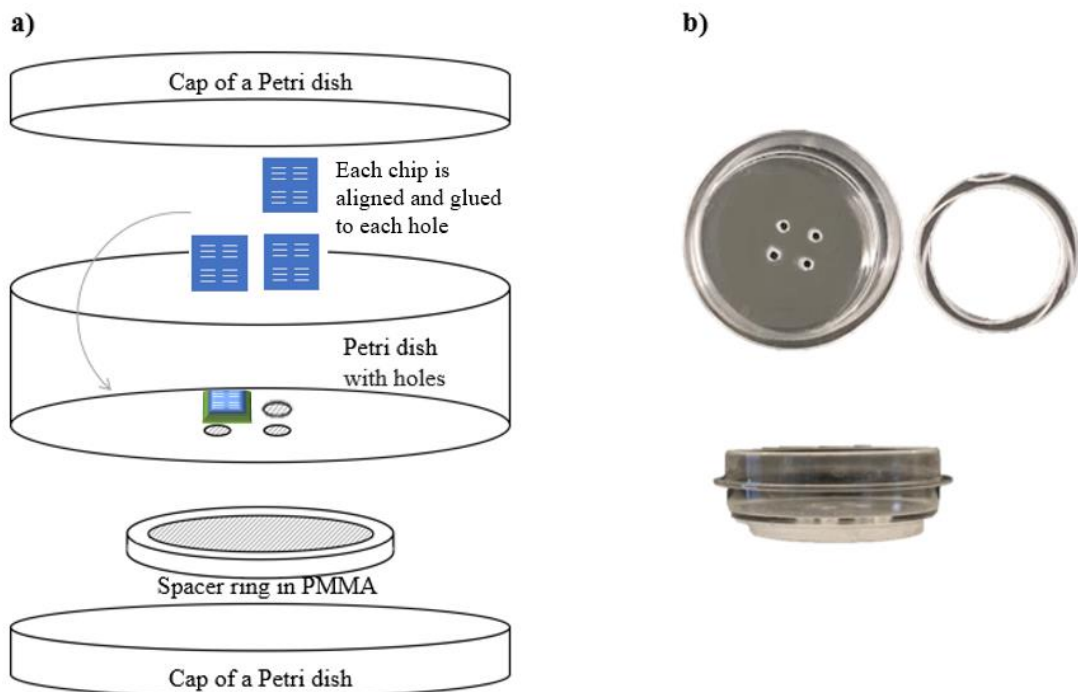


Figure 5.3: a) Schematic diagram of the of the analysis chamber used for the experiments. Each chip was glued to the bottom of a Petri dish on which 4 holes were created, one chip for each hole. b) Pictures of the individual parts of chamber of measurements: commercial Petri dish with homemade holes, PMMA ring spacer, 2 commercial caps of Petri dish.

In order to enable living cells adherence on the substrates, the APTES functionalization protocol (see Chapter 4) was applied on each chip before the experiment.

As can be seen in Fig. 5.4, all experiments with cells were performed according to the following procedure: each chip (blue square) with the final microstructures was glued on each hole created in the Petri dish and the measurement chamber was mounted (Fig. 5.4a); then a 25 μ l droplet containing about 3,000 cells was placed on the top of each chip under sterile conditions and incubated in a humidified atmosphere at 37°C and 5% CO₂ for 20 minutes to allow the cells to adhere while the bottom was kept dry (Fig. 5.4 b); the Petri dish was filled with the medium (2 ml final volume) and incubated at different times. To investigate the effect of microstructures on cell migration, the analyzes were performed on both live cells and fixed cells. Specifically, samples with live cells were left in the incubator (5%CO₂, 37°C) for 12 hours and then observed in the live-cell imaging instrument (with environmental chamber), for the next 12 hours (Fig. 5.4).

For brightfield (BF) imaging, scanning electron microscopy (SEM) and atomic force microscopy (AFM) investigations, 24h after incubation (37°C and 5% CO₂), samples with cells were fixed (PFA 4%) and then analyzed (Fig. 5.4).

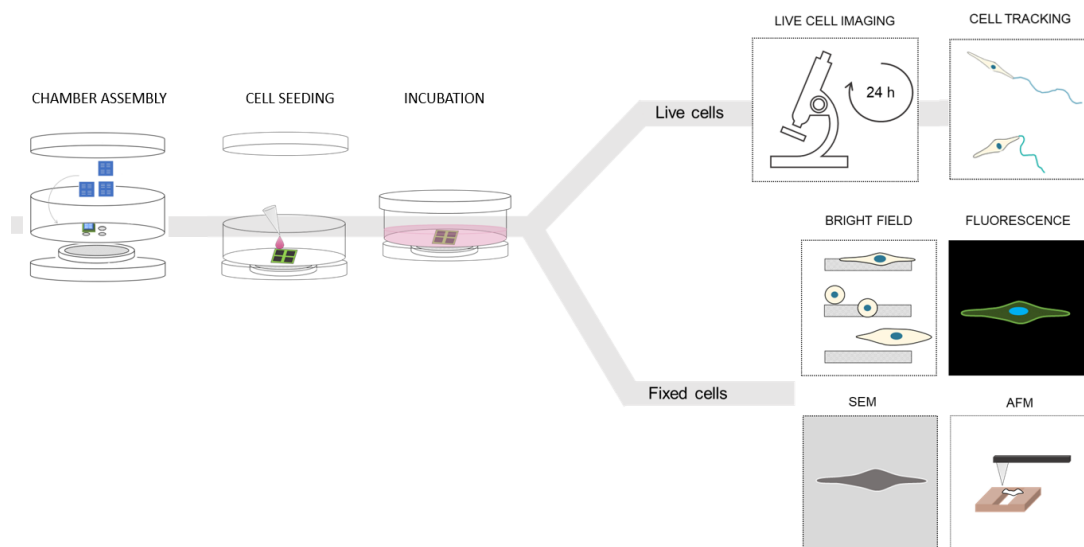


Figure 5.4: a) 4 holes are created on the bottom of a commercial Petri dish (35 mm of diameter) using the laser cutter instrument and each chip is fixed on each hole with a biocompatible glue with the top side facing up; b) a 25 μl drop of cells suspension is placed on the chip surface and incubated for 20 min in incubator (37°C and 5% CO_2) to allow cells to adhere, while the bottom side beyond the gap is kept dry; c) the Petri dish is filled with the medium (2 ml final volume) and the chamber is sealed using a Petri dish cap on the bottom to ensure sterile condition; d) for live cell analysis, samples were left in the incubator (5% CO_2 , 37°C) for 12 hours and then observed in the Live Cell Imaging Instrument for the next 12 hours; e) for fixed cell analysis, cells were fixed 24 hours after incubation and analysed using various microscopy techniques.

5.3. Live-cell migration tracking

Cell migration of MDA-MB-231 and MCF-7 cells was investigated using the Olympus Scan R 3.1 microscope, equipped with the live-cell imaging module. Cells were seeded both on substrates with micro-gaps and on flat Si_3N_4 membranes, left in the incubator (5% CO₂, 37°C) for 12 hours to ensure adhesion and cell recover, and then monitored for the next 12 hours inside the chamber of the live-cell imaging setup. For each experiment, one image was acquired every 15 minutes. The collected images were analyzed using ImageJ software. An example of frames obtained by the migration analysis of MDA-MB-231 cells on micro-gaps is shown in Fig. 5.5.

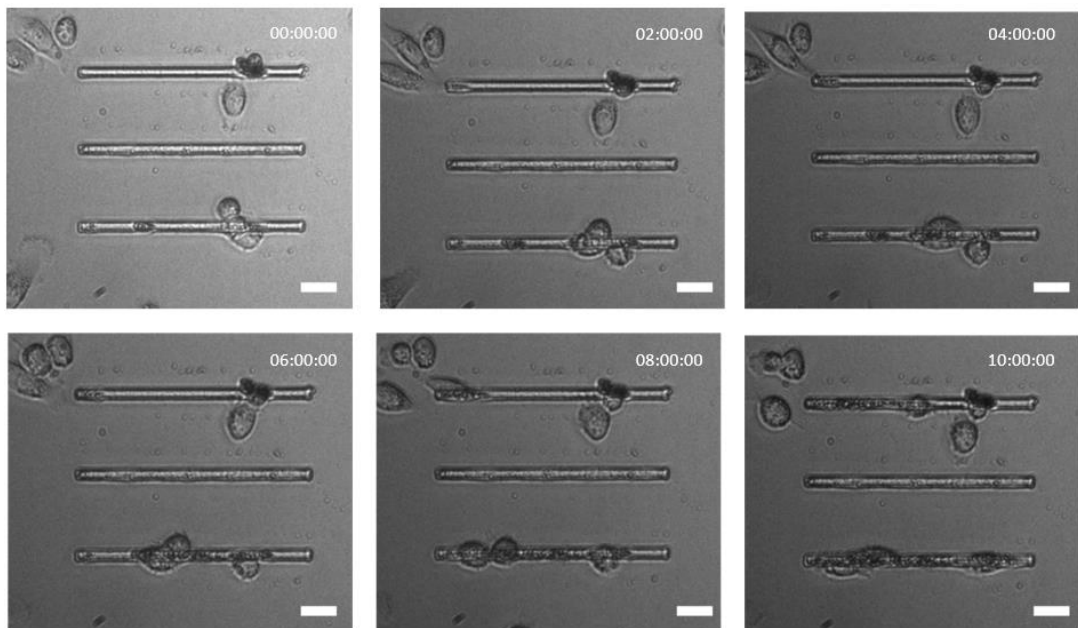


Figure 5.5: an example of frames collected during the experiments with live-cell imaging instrument as obtained for MDA-MB-231 cells grown on the micro-gaps.

5.3.1. Single-cell tracking analysis

The images collected during live-cell imaging experiments were analyzed and the resulting time-lapse videos were used to quantify the velocity of migrating cells. The “Manual Tracking” plug-in allowed individual cell tracking as reported in Figure 5.6. The coordinates obtained with this plug-in were entered in the “Chemotaxis and Migration Tool” (Ibidi®) to extract the total distance covered by a cell both on flat substrate (5.6a) and on gaps (5.6b).

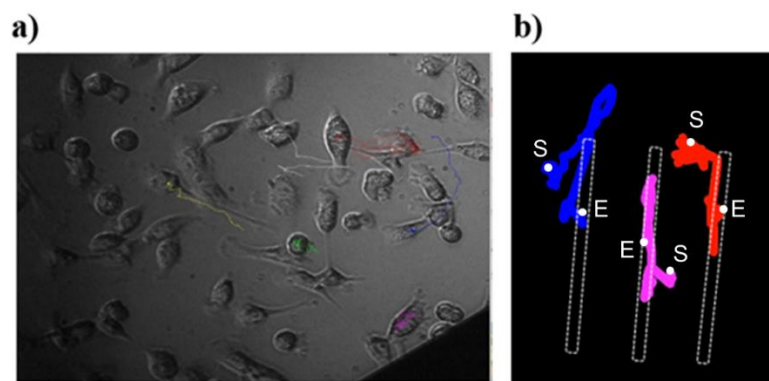


Figure 5.6: An example of cell-tracking analysis for cells on flat substrate a) and on micro-gaps b) The colored lines indicate the trajectories obtain for different cells during migration analysis (S= start point, E= end point).

The velocity values were calculated for cells that were moving along and outside the gaps on flat substrate, using the *Accumulated Distance* and the time intervals in which trajectories of the cells were followed with the “Manual Tracking” plug-in.

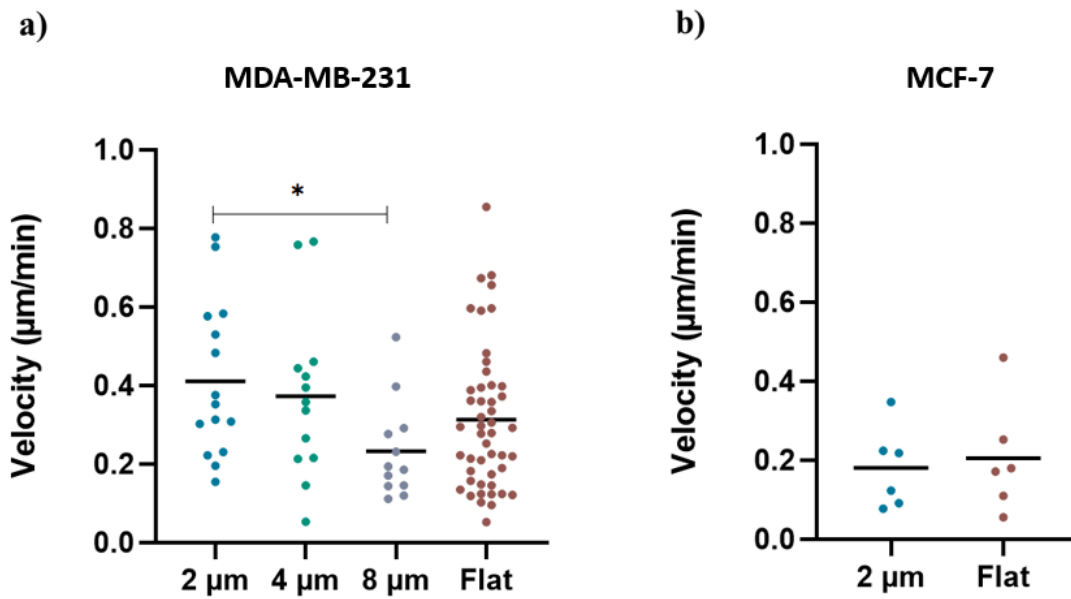


Figure 5.7: a) the graph of the velocity as obtained for MDA-MB-231 migrating on the micro-gaps of 2 μm ($n=15$), 4 μm ($n=13$), 8 μm ($n=12$) wide and on flat substrate ($n=48$); the graph of the velocity as obtained for MCF-7 cells moving on the micro-gaps of 2 μm ($n=6$) compared to flat substrate ($n=6$).

The results are displayed in Figure 5.7a and show a clear dependence of the average cell velocity of MDA-MB-231 cells as a function of gap size with a significant increase for cells moving on the narrower gaps ($0.4 \pm 0.2 \mu\text{m}/\text{min}$) compared to cells moving on 8 μm gaps ($0.2 \pm 0.1 \mu\text{m}/\text{min}$). In addition, we observed no significant difference in the velocity of cells grown in 2 μm wide gaps compared to cells grown on flat substrates, although the average velocity is lower ($0.3 \pm 0.2 \mu\text{m}/\text{min}$). It is likely that the cells grown on the gaps could perceive the presence of a meniscus, the extent of which depends on the gap size, since wider gaps produce meniscus with a lower surface tension. This aspect could influence the physical confinement perception and thus affect the migration mode of cells. The decreasing velocity in the wider gaps could also be due to the lack of anchoring points for the cells inside, making their migration mode difficult by pushing and pulling mechanisms.

In Figure 5.7b, preliminary results showed that there is no significant difference between the average speed of MCF-7 cells grown on 2 μm wide gaps and flat

substrates ($0.2 \pm 0.1 \mu\text{m}/\text{min}$). Moreover, MDA-MB -231 migrate at a higher velocity than MCF -7, both on microstructured and flat substrates. These results are consistent with the literature showing that MDA cells migrate at a higher rate than MCF -7 cells due to their metastatic potential¹²⁵, as also shown by the analysis of migration performed with HWN sensors showed in the previous Chapter.

5.4. Cell density on micropatterned substrates

The quantification of cells adhering to the micro-gaps was done by calculating the normalized ratio of cells grown on the gaps (η). This parameter considers the number of cells that are somehow in contact with the gap to the whole number of cells on the *active count area* (CA).

The *active count area* is defined as the area that a single cell could explore during migration. To quantify this value, the migration tracking analysis was performed on MDA-MB-231 cancer cells by following them for 24h. For each chip, an image was acquired in bright field (BF) microscopy and the whole distance reached by a single cell was calculated with the “Manual Tracking” plug-in of the ImageJ software. By this distance it is possible to obtain the value of the area covered by a cell that is around $2 \times 10^5 \mu m^2$ (indicated in blue in the Figure 5.8a).

In this way the cells that adhere too far from the gap pattern have been excluded from the analysis. In addition, the gap area (GA) was defined inside the active count area, as the area around each gap that includes the cells that are in contact with it. Once defined CA and GA, the count of cells on that area was calculated as follow.

Cell counting was performed using the “Cell Counter” plug-in of ImageJ. Normalization of the cell counting was achieved with the following parameter: (η):

$$\eta = \frac{n_{cells\ gap}}{\sum GA} : \frac{N_{cells\ outside\ gap}}{CA - \sum GA}$$

where $n_{cells\ gap}$ are the cells in the gap area, shown in green in the left image; $N_{cells\ outside\ gap}$ are the cells outside the gap area but inside the active count area; $\sum GA$ is the sum of the GA calculated for each chip (containing 12 gaps, as described in the paragraph above).

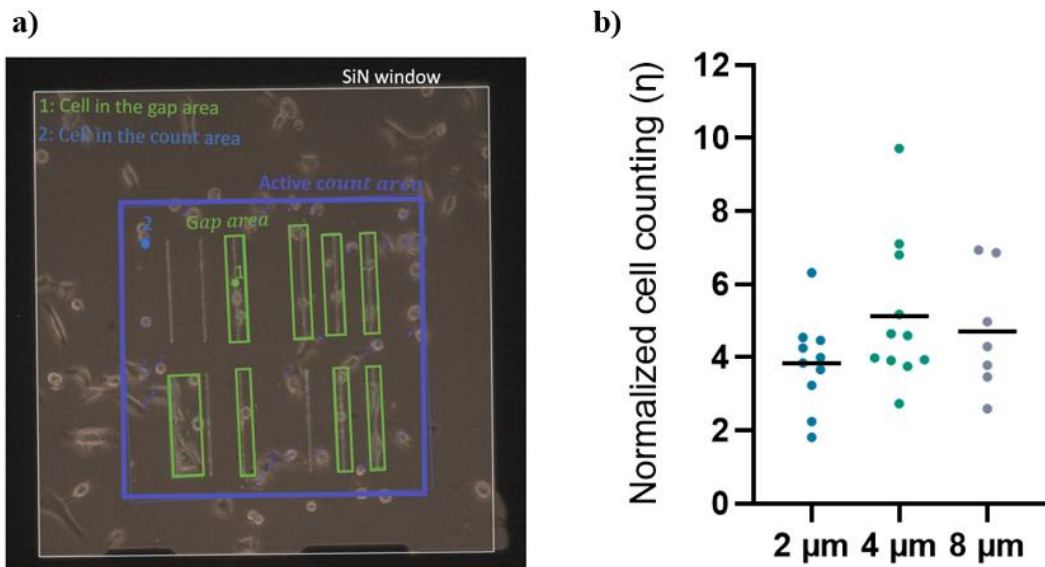


Figure 5.8: An example of image where active count area (CA), in blue, and gap area (GA), in green, are drawn. The number 1 and 2 indicate two cells counted inside the gap area and count area, respectively; b) normalized cells counting (η) on gap area for all gap size: 2 μm ($n=10$), 4 μm ($n=11$), 8 μm ($n=7$).

Normalization of cell counting was performed for all gap sizes (2-8 μm). The results show that cells preferentially remain in contact with the gap (Fig. 5.8b), as all values are >1 . The average density of MDA cells is 3.8 ± 1.2 , 5 ± 2 , and 4.7 ± 1.6 at gap size of 2 μm , 4 μm , and 8 μm , respectively. Statistical analysis shows no significant difference as a function of the gap size. This data clearly shows that cells during their random migration on the surface, when encounter a gap, remain trapped inside and do not move away.

5.5. Morphological characterization of cells as a function of gap size

24 hours after seeding the number and the morphology of migrating MDA-MB-231 cancer cells were analyzed.

From analysis at the electron microscope (SEM), we found a different morphology as a function of the size of the gaps (Fig.5.9). In particular, the cells seeded on the 2 and 4 μm gaps appear to have a more elongated morphology (Fig.5.9a and b, respectively). On the contrary, the cells seeded on the 8 μm gaps appear to have a more rounded morphology (Fig.5.9c).

Moreover, cells in 2 μm gap seem to elongate and place lamellipodia and filopodia at the edge of the cell inside the gap along the microstructures (Fig.5.9d, e, f).

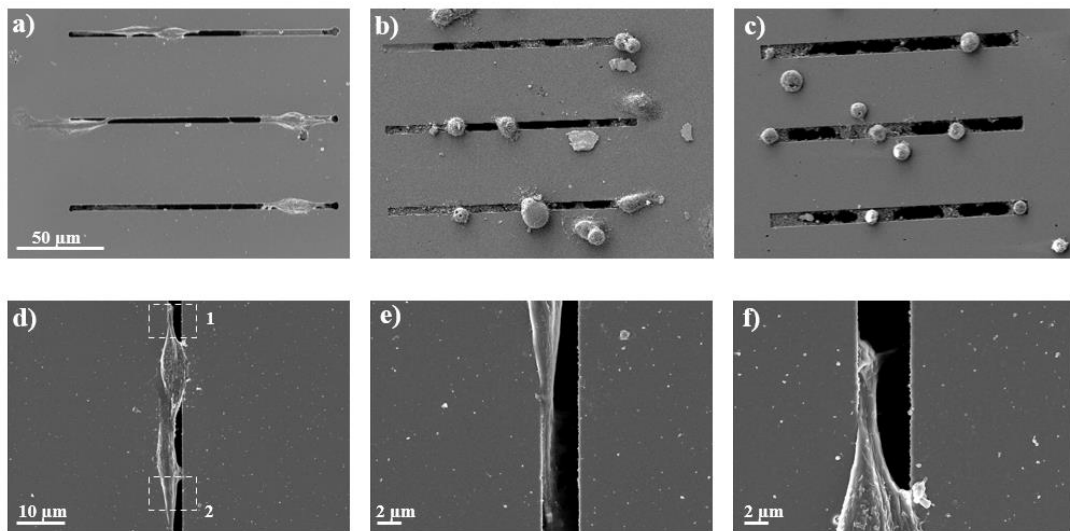


Figure 5.9: SEM images of MDA-MB-231 cancer cells adhered to microstructures with different gap sizes: 2 μm (a), 4 μm (b), 8 μm (c); d) an enlargement of cell on 2 μm gap sized microstructures; zones 1 and 2 are further enlarged in the images e) and f), respectively.

To better characterize cell morphology, the *aspect ratio* (AR) of cells was evaluated as a function of gap size. This parameter, defined as the ratio between the long and short axes of the cell body, was manually drawn around each cell from the optical microscopy images using ImageJ analysis software, as shown in Figure 5.10.

For the analysis, MDA cells were grown on both flat Si_3N_4 substrate and micro-gaps. The average aspect ratio values for cells growing on 2 μm and 4 μm wide are 1.6 ± 0.7 and 1.3 ± 0.4 , respectively, higher than the AR for cells growing on 8 μm wide gaps, 1 ± 0.3 (Fig. 5.11a). For cells grown on flat Si_3N_4 membranes, AR was found to be 1.6 ± 0.5 , which is not significantly different from the values obtained for cells grown on 2 μm wide gaps. These results suggest that cell morphology is influenced by the size of the gaps. Whereas larger gaps lead to rounding of the cells, a gap size of 2 μm seems not affecting too much the cell morphology. Although no significant difference was observed between cells grown on flat and microstructured substrates, it is noteworthy that the edges of cells grown on microstructured substrates can penetrate the gaps, as seen in the SEM images.

Preliminary results with MCF -7 grown on micro-gaps showed that non-metastatic cells perceive the presence of gaps and adapt depending on gap size. As shown in Figure 5.11b, the average aspect ratio for cells on 2 μm wide gaps (1.2 ± 0.2) is significantly higher than on 4 μm wide gaps (1.1 ± 0.1). However, both gap sizes result in a decrease in aspect ratio compared to cells grown on flat substrates (1.3 ± 0.4). Overall, these results suggest that topographic conditions differentially influence the aspect ratio of MDA and MCF -7. The MDA cells grown on the 4 and 8 μm wide gaps can sense the surface tension of the meniscus and a different physical confinement effect by assuming a rounded morphology, which resemble the mesenchymal-ameboid transition during metastatic process¹³⁰.

As shown, MCF -7 are also more elongated on flat substrates than on micro-gaps, but with a smaller impact than in MDA cells. So the lower invasiveness of MCF-7 cells affects their ability to perceive the effects of topographical features, as shown in the literature¹³¹. However, further measurements are needed to better assess the different behaviors of cells grown on micro-gaps.

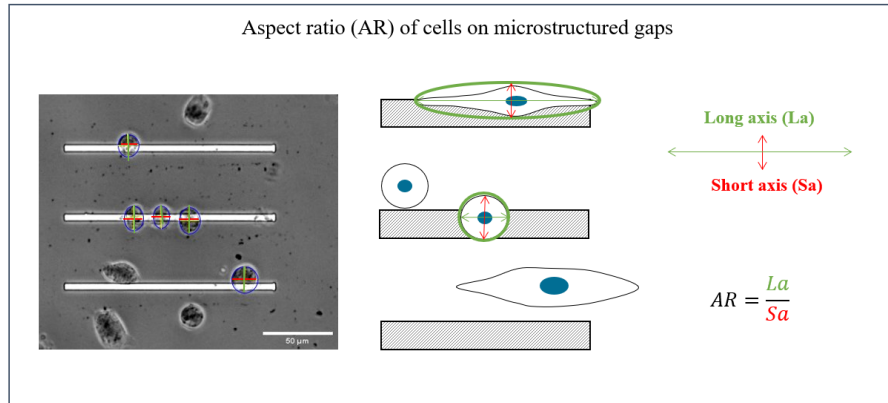


Figure 5.10: On the left, an example of optical images at 20× magnification used to calculate aspect ratio with ImageJ analysis software; on the right, the schematic representation of the long and short axes of cells on structures with different gap sizes used to evaluate the aspect ratio (AR).

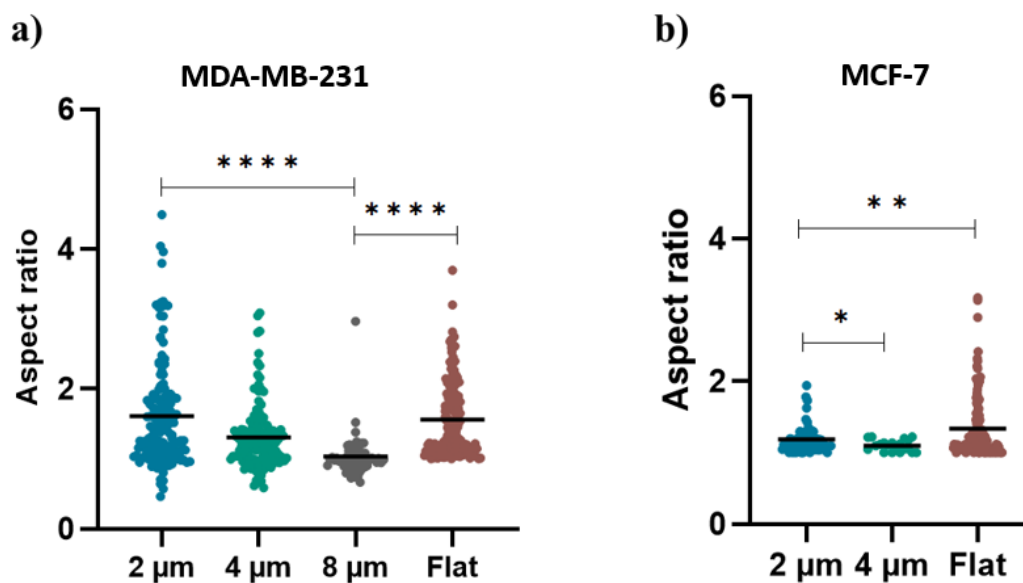


Figure 5.11: a) The values of aspect ratio for MDA-MB-231 cells as a function of gap size: 2 μm ($n=147$), 4 μm ($n=132$), 8 μm ($n=62$) and as evaluated on flat Si_3N_4 membrane ($n=152$); b) The values of aspect ratio (AR) for MCF-7 cells as a function of gap size: 2 μm ($n=64$) and 4 μm ($n=20$), and as evaluated for cells on flat SiN membrane ($n=138$).

For both the velocity and aspect ration investigation, statistical analysis was performed using GraphPad Prism (version 8.4.3). Statistical significance was determined by a two-tailed Student's t test. $P \leq 0.05$ (*), $P \leq 0.01$ (**), $P \leq 0.0001$ (****) were considered statistically significant.

5.6. Cytoskeleton and nuclei adaptation

Fluorescence microscopy analysis of the MDA-MB-231 cells was performed 24h after seeding. To better characterize the distribution of the actin cytoskeleton and the adaptation of the nuclei on the micro-gaps, the cells were stained with phalloidin (Alexa Fluor™ Plus 555 Phalloidin) and DAPI (GeneTex). The images showed a different morphology of the cells growing on the microstructures, because the smaller the gap size, the larger the cell extension in the direction on the gap.

In addition, both the cytoskeleton and the nuclei are affected by the size of the gaps, as the actin cytoskeleton appears differently elongated and the nuclei adapt to the gap (Fig. 5.12).

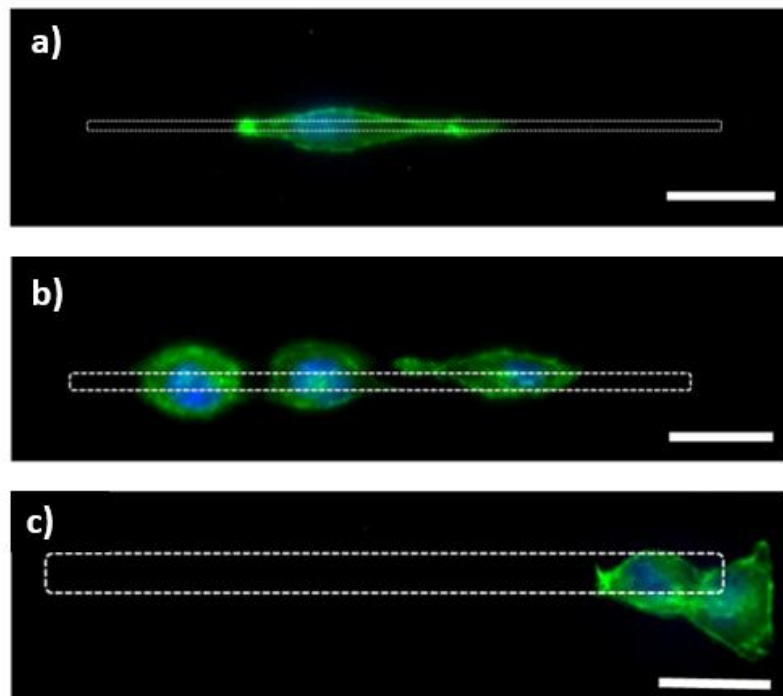


Figure 5.12: the fluorescence images of MDA-MB-231 cells grown on micro-gaps with different gap size. Cells in gaps 2 μm wide (a) appears more elongated than in gaps 4 μm (b) and 8 μm (c) wide.

All together these findings show that the cells grown on the microstructures can perceive the presence of the gaps. It must be considered that the effect of the gap size on cell morphology may also be influenced by the presence of the water meniscus. The fact that the narrower gaps cause elongation and reorganization of the cytoskeleton can be explained by the fact that the cells perceive the gaps as gaps and experience the phenomenon of *contact guidance*^{21,31,32}.

In the 8 μm gaps, cells are more likely to perceive the presence of the underlying water meniscus. Probably the larger gap creates a meniscus with a lower surface tension, which cells may perceive as a softer substrate. Indeed, many studies have shown that MDA-MB -231 cancer cells exhibit a rounder morphology on softer substrates¹³².

5.7. Orientation of cells along the micro-gaps

As fluorescence and electron microscopy analysis showed, the cells can change their orientation as a function of the topographical aspect of the substrate where they are grown. To better analyze this parameter, the cell orientation was calculated as the angle between the major axis of the ellipse fitting the cell and a line parallel to the side of the Si_3N_4 membrane, as described in the Figure 5.13.

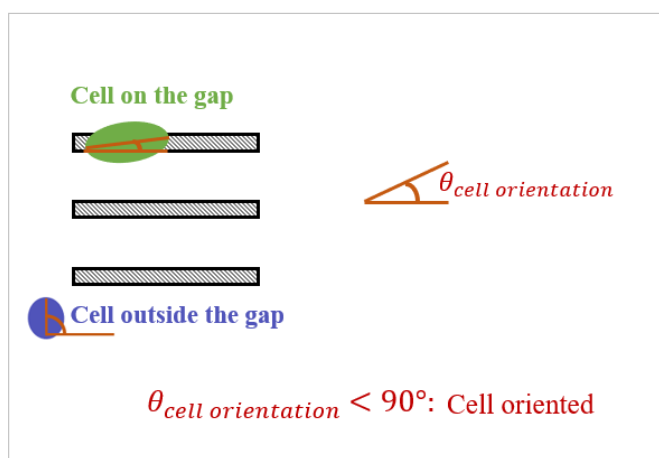


Figure 5.13: schematic of the calculation of cell orientation based on the angle between the major axis of the ellipse fitting the cell and a line parallel to one side of the Si_3N_4 window.

The results of the orientation analysis showed that the MDA cells have a stronger orientation along the micro-gaps compared to those grown on flat substrates (Fig. 5.14a). The orientation angles are $(2.3 \pm 1.4)^\circ$, $(2.6 \pm 2)^\circ$, and $(2 \pm 1.3)^\circ$ for cells grown on 2, 4 and 8 μm wide gaps, respectively, and $(43 \pm 33.4)^\circ$ for cells grown on flat substrates. The remarkable orientation of MDA-MB -231 cells grown on micro-gaps is consistent with previous reports of cells grown on microstructured gratings¹²⁷. As preliminary results, orientation analysis performed on MCF -7 cells grown on micro-gaps of 2 μm and 4 μm and on flat substrates showed that these cells also perceive the topographic effect due to the presence of the gaps, with a lower

orientation for flat substrates (57 ± 29) ° compared with microstructured substrates, (6.1 ± 8.6) ° and (17.5 ± 16) ° for 2 μm and 4 μm wide gaps, respectively (Fig. 5.14b).

In addition, MCF-7 cells could be less oriented when grown on micro-gaps compared with MDA-MB-231 cells. These results are consistent with literature, as it has been shown that due to the lack of 3D geometric recognition, MCF-7 have fewer interactions with the substrate compared to MDA-MB-231 cells. The cells with higher metastatic potential are more able to perceive the topographical features of micropatterned substrates and adapt to them in order to enhance their invasiveness capability^{131,133,134}.

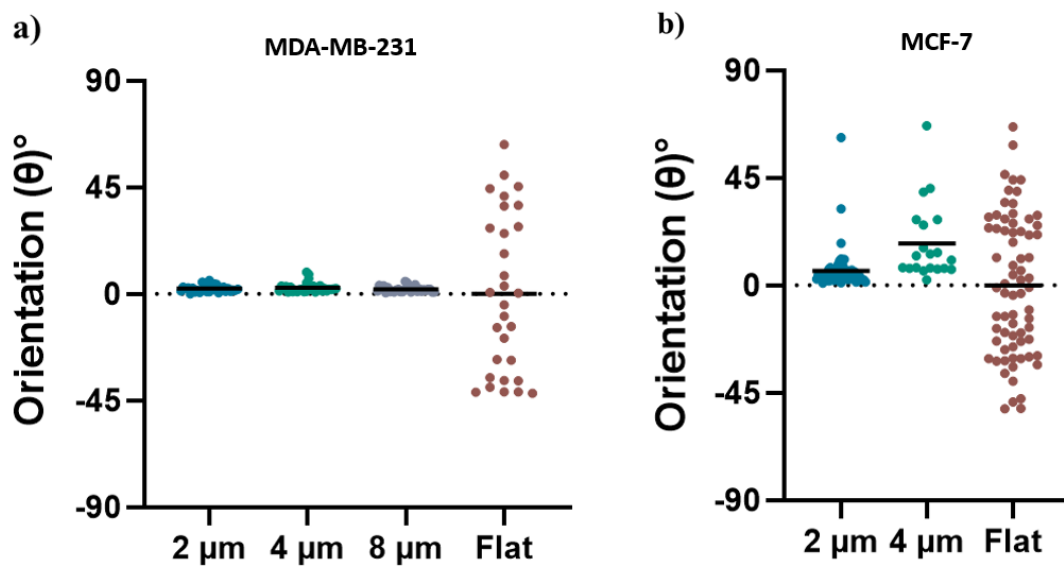


Figure 5.14: a) the distribution of orientation angles for MDA-MB-231 cells as a function of gap size: 2 μm (n=32), 4 μm (n=30), 8 μm (n=30), and as evaluated on flat Si_3N_4 membrane (n=30); b) the distribution of orientation angles for MCF-7 cells: 2 μm (n=60), 4 μm (n=20), and on flat substrate (n=70).

Overall, these results showed that the micropatterned substrates can be used to distinguish cancer cells with different metastatic potential based on morphological and velocity response.

5.8. ECM deposition on micro-gaps during cell migration

Live-cell tracking analysis revealed that cells secreted residues during migration on micro-gaps (Fig. 5.15).

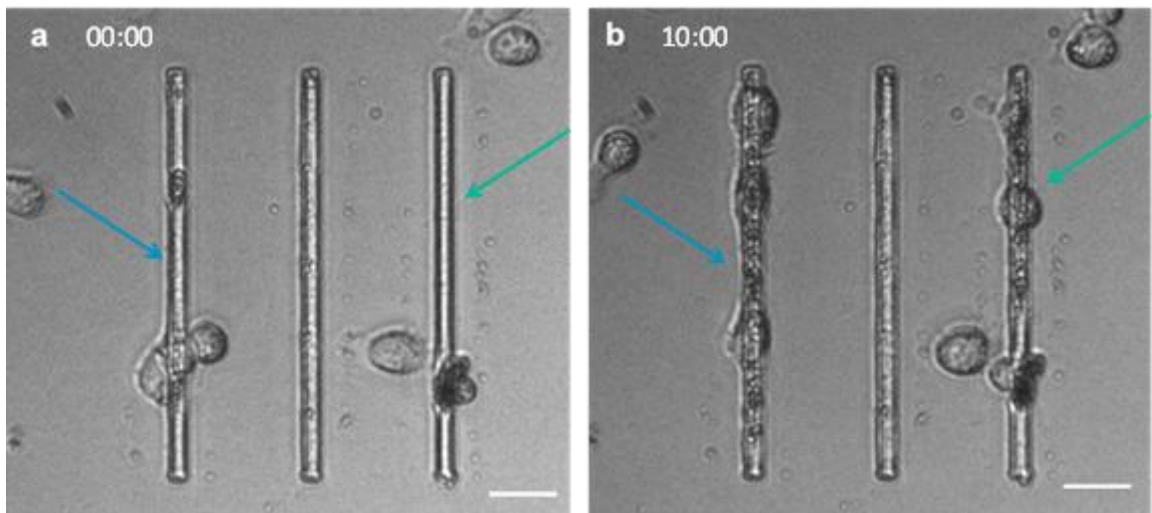


Figure 5.15: MDA cancer cells grown on the micro-gaps (4 μm wide): the arrow indicates the zones where cells have produced ECM at the beginning (a) and 10 hours after migration analysis (b).

To better characterize and analyze that structures, SEM and AFM analysis were performed on fixed and dehydrate samples 24h after migration. SEM analysis demonstrated the presence of a layer that accommodates the curvature of the

water meniscus and resembles the structures that compose extracellular matrix, as shown in the Figure 5.16.

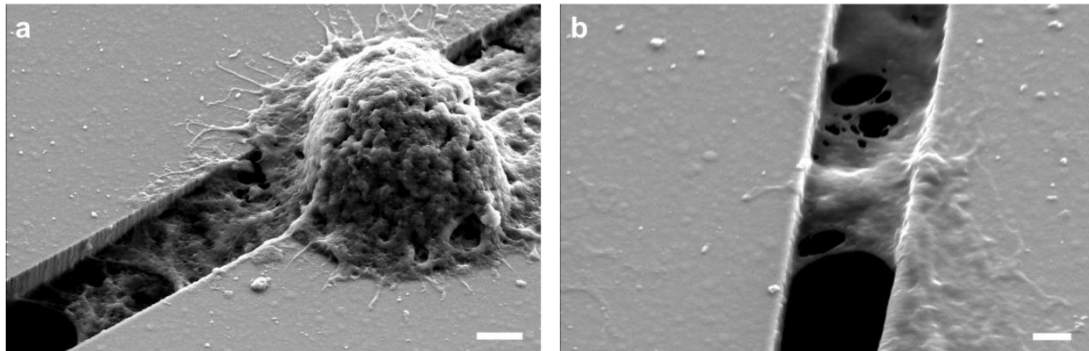


Figure 5.16: SEM image of a MDA-MB-231 cell grown on micro-gaps ($4\ \mu\text{m}$ wide) 24 hours after seeding showing the ECM residues produced (a), and the magnification of the residue layer (b).

AFM imaging was performed and confirmed the presence of the residues around the gaps (Fig. 5.17a) and a layer inside the gaps with a depth of $1.5\ \mu\text{m}$ (Fig. 5.17b). Higher magnification of the images showed the presence of a matrix within the structures organized with such periodicity ($60\pm 5\ \text{nm}$) compatible with typical fibrous of ECM, such as collagen.

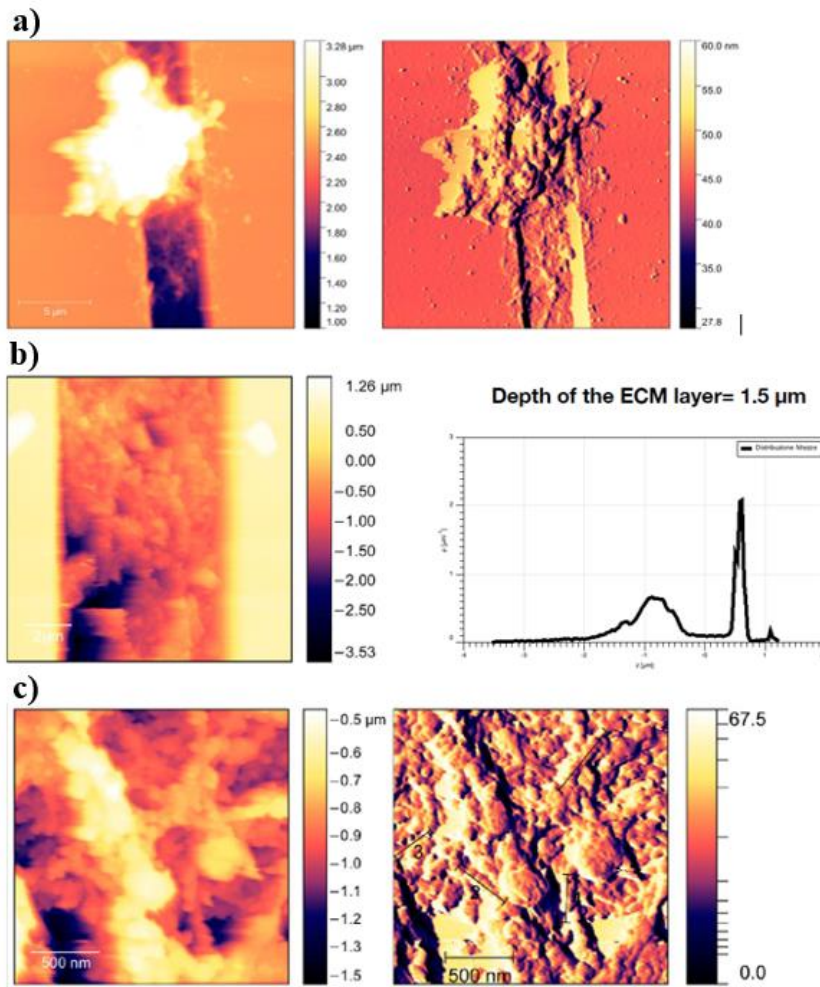


Figure 5.17: a) AFM images of the structures deposited on the micro-gaps (2 μm wide) by the MDA-MB-231 cells after 24h of migration; b) analysis of the image taken across the micro-gaps (2 μm wide) shows a depth of the layer within the gap of about 1.5 μm, next to the diagram of the analyzed height distribution; c) analysis of periodicity of the structures (as marked with the black bars) performed on a magnified image of the layer deposited in the gap.

Our results reveal two important features: cancer cells can perceive the presence of the micro-gaps and secrete ECM to attach to such aligned structures. Moreover, the higher secretion of ECM on these structures compared to surrounding zones might serve for cells to improve cell adhesion and modulate interactions with the environment to enhance migration. It is well known that the balance between degradation and secretion of ECM is responsible for tissue homeostasis, and several studies address the critical role of ECM and its impact on cancer cell morphology and consequently on cancer

cell invasion and metastatic potential¹³⁵. Modeling the ECM microenvironment can be useful to capture mechanistic properties to better understand tumor spread and develop therapies against it¹³⁶. Evidence suggests that the ECM acts as a dynamic scaffold that stimulates cancer cell morphological changes and modulates tumor development and metastatic potential of breast cancer cells. It has been shown that MDA-MB-231 cancer cells become more elongated in 3D cultures with denser ECM components¹³⁷ and with increasing degrees of ECM fiber alignment, that perform more targeted *contact guidance*¹³⁸. Moreover, observing the production of ECM on our micro-gaps could be interesting and relevant for the development of ECM-based biomaterials. Indeed, given the importance of ECMs, their structures, properties, and functions are continuously being explored to enable the development of biomaterials that promote the formation of functional tissues in clinical applications¹³⁹.

Conclusion and future perspectives

Cancer is a pathological condition that results from the uncontrolled growth and migration of cells. For a comprehensive study of cell migration, several aspects need to be considered, from physical to topographical features that can alter the behavior of cells to form metastases. The role of such features in cancer development and progression remains unclear to date. Understanding these mechanisms is useful for determining what distinguishes cancer cells from normal cells and for discovering new mechanisms and markers that can serve as targets for cancer therapies. It is also useful for determining the factors that support the metastatic process. In this work, I have presented two systems to study the mechanisms underlying cancer cell migration: a novel nanomechanical sensor capable of measuring the forces exerted by cancer cells, and a 2D assay based on micropatterned substrates that allows us to study the effects of topographical effects on the behavior of migrating cancer cells.

In summary, I have designed and fabricated a novel nano-motion detector that improves the sensitivity and performance of nanomechanical sensors and reduces the attenuation losses of the cantilever by operating with only one side in contact with a liquid solution, a so-called half-wet configuration. I have shown that this approach makes it possible to detect and evaluate the differences in adhesion force and motility of two breast cancer cell lines simultaneously with optical observation of cell activity. These results suggest that this approach is a promising tool for real-time analysis of the dynamics of cell adhesion and the effect of drugs that affect this cellular process (i.e., adhesion and motility). Moreover, the ability to multiplex such a substrate could be a great advantage for monitoring therapeutic outcomes in cancer patients. The half-wet architecture that I used to improve the sensitivity of our nanomechanical sensors was used to develop a novel 2D assay based on micropatterned substrates that allow to separate the effects of physical confinement, stiffness, and curvature to which tumor cells are exposed during

migration.

In addition, the presence of a meniscus could play a role in the perception of the physical confinement to which the cancer cells are exposed *in vivo*. Moreover, this design recreates a state of spatial confinement in which cells can experience different adhesion conditions that occur during the migration process. The results showed that cancer cells modulate their morphology, velocity and orientation depending on the size of the microstructures. Moreover, cancer cell lines with different invasiveness potential seems to perceive differently some geometrical and physical cues.

This *in vitro* assay could be a simple tool to mimic both the architecture and biophysical cues of the extracellular matrix, investigate the effects of these features on cell migration, and distinguish cancer cells with different metastatic potential based on morphological and velocity responses. Since this assay is based on conventional optical techniques, all analyzes are compatible with automation procedures. This aspect could be a great advantage when considering the use of these substrates as rapid diagnostic tools. Both the half-wet nanomechanical sensors and the substrates with micro-gaps can contribute to a better understanding of the mechanisms underlying the mechanobiological aspects of tumor development and progression. Such information can complement computational modeling techniques that address the simulation of the mechanical components involved in biological processes and develop new diagnostic tools for cancer prevention and treatment.

Appendix

This appendix describes the design and fabrication of a platform for bioassay applications. This work is the result of a collaboration with the Karolinska Institute group led by Professor Ana Teixeira, to which I had the opportunity to participate during my PhD studies.

As described in Chapter 4, the use of the HWN sensors for the study of cell dynamics required the functionalization of the sensor surface to improve cell adhesion. The optimized functionalization protocol served as the starting point for the development of the bioassay platform. The aim of this work was to develop a simple and cost-effective platform based on substrates whose functionalization enables the specific binding of the Her2/Her3 protein for the validation of an analytical method based on DNA-based molecular sensors.

At CNR-IOM laboratories, I have designed, fabricated, and characterized these substrates, which have been subsequently used and tested at Karolinska Institute.

The following section describes the work done so far.

“Patterned carboxymethyl-dextran functionalized surfaces using organic mixed monolayers for biosensing applications”

Introduction

The field of biosensing has grown exponentially since the first report of its application⁵⁵. As mature, versatile, and well-established technologies, electrical and optical biosensors dominate biological detection research worldwide^{51,140}. However, the mechanical nature of many fundamental biological processes paved the way for the extensive use of nanomechanical biosensors⁶⁴. Regardless of type, the use of these sensors for biological applications requires functionalization of the surface to enable cell adhesion or immobilization of the analytes of interest. Immobilization of biomolecules on biosensor surface platforms plays a key role in achieving the required sensitivity and selectivity for the analysis of biomolecular interactions. Controlling the interaction between the surface and biomolecules plays a critical role in modulating the surface properties required to improve assay performance and detection results¹⁴¹. The main approaches to immobilize molecules on biosensor surfaces are based on physical adsorption and covalent coupling. In physical adsorption, proteins react spontaneously with the surface through non-covalent interactions. Due to the variety of molecular phenomena involved, predicting the interaction and bioactivity of proteins on the surface is challenging¹¹². In contrast, immobilization by covalent bonding results in stronger bonds with substrates. One of the most commonly used methods for selective adsorption of biomolecules is the generation of self-assembling monolayers (SAMs) to introduce reactive moieties on inert metallic surfaces (e.g., gold, silicon, titanium) that can be further derivatized with ligands¹¹³. Silanization with aminosilanes is widely used because of the high reactivity of the terminal amino groups (NH₂) in subsequent coupling reaction¹¹³. Among them, 3-

aminopropyltriethoxysilane (APTES) has been extensively used for the functionalization of bioanalytical platforms^{114,115}. The advantages of covalent bonding and the use of hydrogels have been chosen by many companies as the best combination for the production of commercially available SPR platforms. Indeed, commercially available SPR sensors which consist of a chip coated with a thin layer of gold use CMD self-assembled monolayer as immobilization matrix^{142,143}. Although surface immobilization of molecules is easier to perform, three-dimensional immobilization provides more binding sites and a better environment for retention of the immobilized molecules. Thanks to their smart properties and versatility, hydrogels are increasingly becoming a functional tool for 3D immobilization¹⁴⁴. The most commonly used matrix for three-dimensional immobilization is the carboxymethylated dextran (CMD)¹⁴⁵, a carboxymethylated form of dextran, that allows the introduction of reactive anchor groups. Thanks to the low-fouling properties and the availability of free carboxyl groups homogeneously distributed on the polymer, the CMD coating can efficiently enable the chemical grafting of capture antibodies while serving as a blocking layer for protein adsorption per se¹⁴². Moreover, by carbodiimide-based linkage chemistry CMD is suited for the conjugation of biomolecules forming covalent bonds between its carboxyl groups and aminated surface¹⁴⁶.

1. Carboxymethyl-dextran (CMD) patterned surfaces for biosensing application

In the present work, we have developed and optimized a technique to produce low-cost patterned surfaces based on CMD for the immobilization of biomolecules. They consist of silicon or glass substrates with patterned bioactive surfaces capable of efficiently entrapping the sampling solution by simply using the hydrophilic/hydrophobic patterning of the surface. The hydrophilic areas were first functionalized with APTES through the vapor deposition protocol, presented in Chapter 3, which was previously optimized for cell attachment on the surface of HWN sensors. Subsequently, CMD is linked to enable analyte binding. The fabrication process involves the use of low-cost instrumentation and techniques compatible with large-scale production. The devices were validated using a chemiluminescence assay that we recently developed for analyzing the binding of DNA nano-assemblies modified with an affinity binder to target proteins immobilized on the bioactive areas. Using this assay, we were able to characterize the chemical reactivity of two target proteins toward the dextran matrix of the patterned surfaces and compare them with standard CMD -based surfaces for Surface Plasmon Resonance (SPR) analysis. We found high reproducibility and selectivity in molecular recognition, consistent with the results obtained with SPR sensing surfaces. The proposed approach is straightforward and cost-effective and provides the opportunity to evaluate patterned functionalized surfaces for bioanalytical platforms. We have developed arrays consisting of silicon or glass substrates with patterned bioactive areas capable of efficiently entrapping the sampling solution by simply exploiting the hydrophilic/hydrophobic patterning of the surface. This bifunctional patterning was achieved by depositing 3-aminopropyl-triethoxysilane (APTES) on selected 1 cm diameter areas surrounded by a self-assembling monolayer (SAM) of octadecyl-trichlorosilane (OTS) (Fig. 1a).

APTES allows efficient immobilization of CMD, as shown in several studies^{113,147}, while OTS provides the necessary hydrophobicity for the confinement of water-based sample solutions. The APTES areas were then functionalized with a thin film of CMD to obtain the bioactive surfaces areas (Fig. 1b). Following the design and fabrication of the OTS/APTES patterned surface and its characterization, thus the fabrication of CMD-patterned surfaces, their characterization and validation as biosensing assay.

1.1. Design and fabrication of OTS/APTES patterned surfaces

The fabrication process involves the use of tools and techniques compatible with large-scale production (Fig. 1c): first, the substrates (SiO_2 or coverslips) were cleaned to efficiently remove the organic impurities and promote the formation of the hydroxyl groups required for functionalization with OTS. OTS was deposited on the samples through vapor deposition process (in static vacuum) for 4 hours at room temperature (RT); an annealing process, which consisted of incubating the samples for 2 hours at 120 °C in continuum vacuum, promoted the removal of unreacted molecules adsorbed on the surface, resulting in a more homogeneous and hydrophobic SAM uniformity and hydrophobicity. Then, we proceeded with deposition of APTES on defined patterned areas. To achieve selective deposition, we used a silicon mask made from a silicone foil in which we created holes of the desired dimensions using a CO_2 laser cutter. This method enables the rapid fabrication of masks with large dimensions, so that dozens of samples can be prepared simultaneously. In addition, silicone-based masks are reusable and can adhere to the OTS-modified surface by taking advantage of the self-adhesive properties of apartment silicone. The mask-covered surface was subjected to oxygen plasma treatment (40 W, bias 120 V) to promote the removal of OTS from the exposed areas. The sample was then transferred to a chemical vapor deposition (CVD) chamber to deposit APTES, which selectively binds to the areas from which the hydrophobic OTS SAM was removed. APTES (99%, Sigma-Aldrich) was applied to the samples through vapor deposition process (in continuum vacuum) in a glass chamber (as described in the HWN functionalization section).

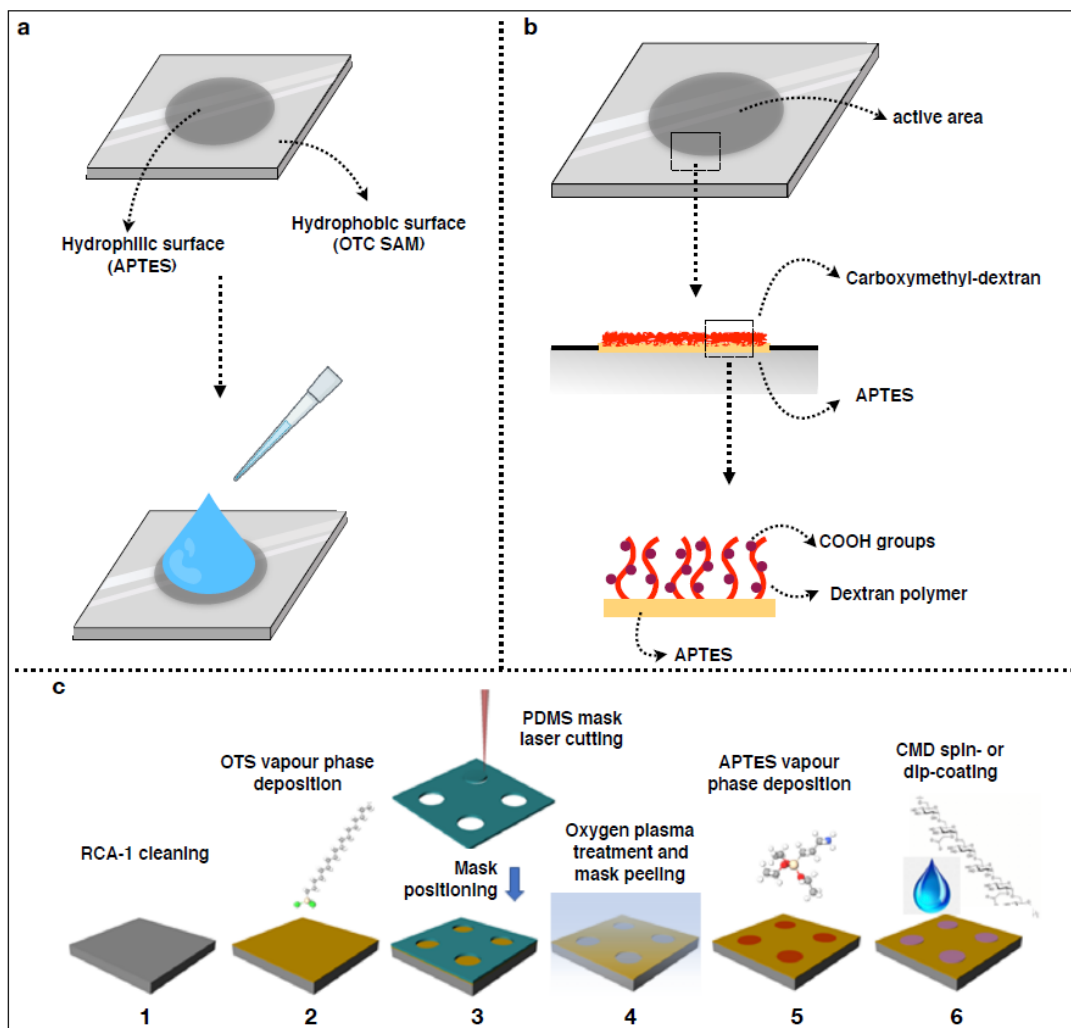


Figure 1: Schematic representation of carboxymethyl-dextran patterned silicon surfaces. *a*, Square silicon surfaces or glass surface (10 cm x 10 cm) were treated with octadecyl trichloro silane (OTS) to create a hydrophobic Self Assembled Monolayers (SAM). Round hydrophilic active areas (1 cm diameter) were created by removal of OTS SAM and subsequent deposition of (3-Aminopropyl) triethoxysilane (APTES). The dual feature of the surface allows to confine the sample/reaction drop in the limited active area. *b*, Schematic of the composition of active areas. Deposition of APTES created a layer to promote the adhesion of carboxymethyl-dextran brushes. The chains of dextran polymer are functionalized with carboxylic groups. *c*, Schematic representation of the fabrication process of carboxymethyl-dextran functionalization. (1) Surface cleaning by RCA-1 solution, (2) OTS vapour phase deposition, (3) PDMS mask fabrication and positioning, (4) oxygen plasma treatment and mask peeling off, (5) APTES solution/vapour phase deposition, (6) CMD spin- or dip- coating.

1.1.1. Characterization of OTS/APTES patterned surfaces

We verified the quality and reproducibility of the deposition of OTS/APTES SAM with water contact angle measurements (Fig. 2) and atomic force microscopy (AFM) on SiO₂ substrates (Fig. 3). The water contact angles on APTES areas were different from the contact angles on OTS, indicating efficient patterned deposition of APTES SAM. In addition, the water contact angles were measured before and after the patterning process, showing that mask-based removal of OTS with oxygen plasma treatment effectively removed OTS from the exposed areas and protected the unexposed areas from the effects of oxygen plasma treatment, preserving hydrophobicity on OTS areas and selectivity on APTES areas for the subsequent deposition of CMD (Fig. 2).

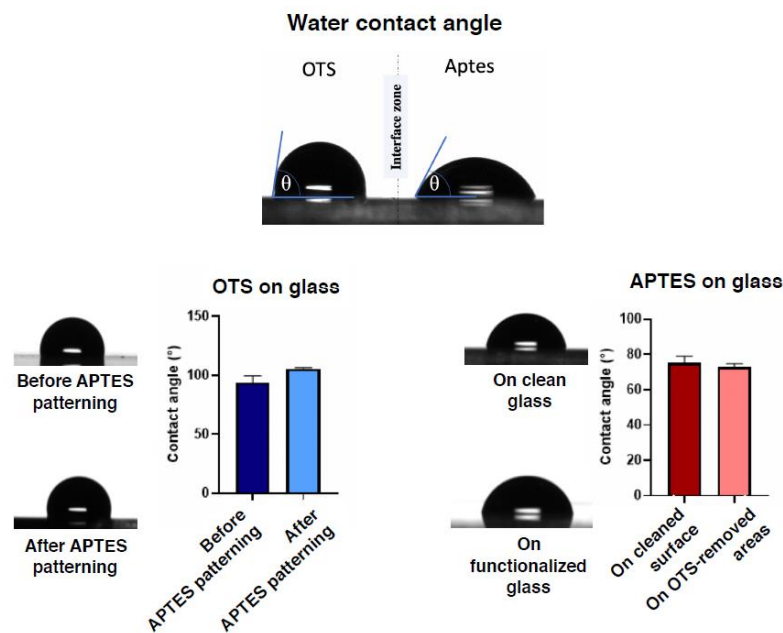


Figure 2: **a)** water contact angle at the interface region between OTS and APTES (top). **b)** no significant variation on the contact angle values of the OTS SAM deposited on glass before and after the treatment with oxyplasma and APTES deposition demonstrated that the process used for APTES patterning preserve the hydrophobicity feature of OTS SAM (bottom, left). APTES deposited on patterned areas where OTS was removed resulted in similar contact angle value obtained when deposited on cleaned glass (bottom right).

The structure of SAMs absorbed on the surfaces was also imaged by AFM (Fig. 3). The surfaces appeared to be fully covered, and when evaluating of the

roughness values, we found an increase in surface roughness for both SAMs from OTS and APTES, from 0.09 to 0.19 nm and to 0.21 nm, respectively, with respect to the value obtained with purified silicon substrate. The proposed method allows the definition of complex patterns for surface functionalization down to the resolution of laser cutting, avoiding the use of more complex and less reliable techniques¹⁴⁸. Indeed, many methods for SAM patterning are described in the literature (e.g., microcontact printing, AFM grafting, dip-pen nanolithography). Our alternative approach allowed us to achieve the resolution required for the device while ensuring a much faster and easily scalable method. Moreover, it allows selective functionalization of surfaces with two different SAMs in a few simple steps without affecting their quality and cleanliness, as shown by the AFM and contact angle analysis performed.

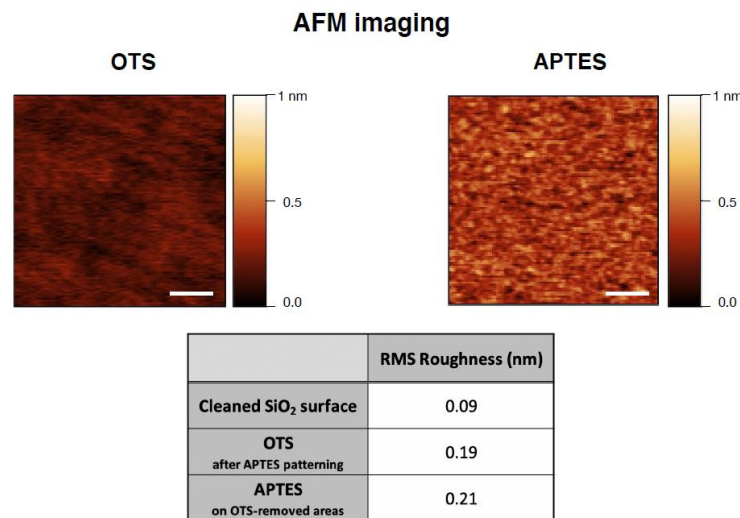


Figure 3: Characterization of the OTS and APTES SAMs by means of AFM imaging. AFM images of OTS and APTES SAM on silicon at the end of the APTES patterning process (OTS deposition, mask-based oxygen plasma removal of OTS and APTES deposition). RMS roughness values of SAMs are shown in the underlying table. Area of images: 1 x 1 μ m. Scale bars: 200 nm.

1.2. Fabrication of Carboxymethyl-dextran (CMD) patterned surfaces

Finally, we deposited the CMD to functionalized APTES surfaces. We tested and characterized two different deposition methods, dip coating and spin coating. We prepared the solution by dissolving CMD (Sigma Aldrich – MW 20 kDa) in DI water at a variable concentration between 1 and 10 wt%; the solution was then stirred overnight to allow complete and homogeneous dissolution. A 5% solution was used for spin coating; the final thickness can be modulated by changing the spin rate. The ellipsometry data showed a strong dependence of the CMD film thickness on the rotational speed when comparing the thickness values at 1000 and 2000 rpm. However, varying the rotational speeds to 3000 and 4000 rpm did not cause a significant difference in CMD film thickness¹⁴⁶. We chose 2000 rpm as the optimal rotational speed for our deposition protocol. Although dip coating is the preferred method for complex patterns and leads to very precise separation between hydrophobic and hydrophilic area, spin coating results in faster and more reliable CMD deposition, including control of the thickness control and uniformity of the deposited film¹⁴⁹.

1.2.1. Characterization of carboxymethyl-dextran (CMD) patterned surfaces

The CMD matrix was visualized by AFM imaging as molecular aggregates, which were revealed by the increase in surface roughness (Fig. 3). Moreover, both AFM imaging and optical profilometer analysis of CMD, showed that the height of dextran deposition obtained by spin coating was in the range of 20-40 nm, which is consistent with previously reported data¹⁴⁴, while deposition by dip coating resulted in a thicker CMD layer (Fig. 3). A higher MW of CMD entails longer branching chains and a higher layer thickness, leading to a higher protein immobilization potential. On the contrary, a high-density dextran matrix may face several problems, such as matrix swelling due to chain repulsion and matrix expansion¹⁴⁶ and steric hindrances. Consequently, the ability of the analyte to reach all available immobilized proteins decreases, and the equilibrium state between protein and analyte is reached only after a long time¹⁵⁰, leading to a decrease in detection sensitivity. For this reason, a trade-off between these two events was preferred in the preparation of the surface by choosing an intermediate size MW (20 kDa) and thickness of the dextran layer (20-40 nm) to ensure optimal results in biomolecule binding assays.

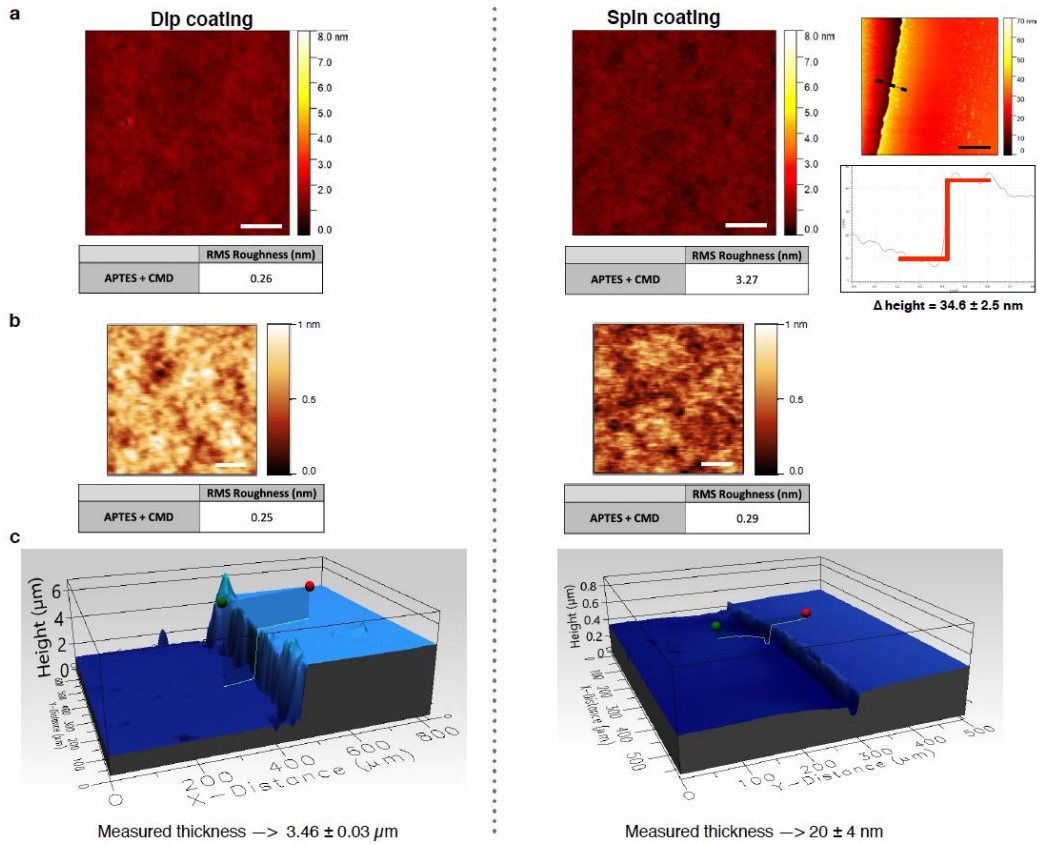


Figure 3: **a, b**, AFM map and respective roughness values of CMD on SiO₂ deposited by dip coating (left) and spin coating (2000 rpm) (right). **a**, Area of images: 5 x 5 μ m. Scale bars: 1 μ m. n = 10. **b**, Area of images: 1 x 1 μ m. Scale bars: 200 nm. n = 4. For the sample obtained with spin coating a section analysis (red line on the image) has been performed. **c**, Optical profilometer map at the CMD coated region produced by dip coating (left) or spin coating (right).

1.3. Validation of the CMD-based patterned platform for biosensing application

To understand and characterize how biomolecules interact with our functionalized SiO₂ surfaces and to evaluate the yield of protein immobilization resulting from the different fabrication processes (APTES: solution vs. vapour phase deposition - plus vs. minus annealing treatment; CMD: dip vs. spin coating), we performed a bioassay that we recently implemented in the development of a non-microscopy-based method for ensemble analysis of membrane protein nanodomains called NanoDeep¹⁵¹.

Briefly, the DNA nanoassembly, called NanoComb, consists of a double-stranded backbone with four single-stranded DNA sequences (prongs) protruding from the backbone at regular intervals. The first prong is preloaded with an oligonucleotide conjugated binder specific for a target protein.

In our workflow, the target protein was the extracellular domain of human epidermal growth factor receptor 2 (ECD-Her2), which was immobilized by amine coupling to active areas of the CMD-based patterned surfaces. The amine coupling chemistry (EDC/NHS), used to activate the CMD layer for immobilization of biomolecules¹⁵², simultaneously allowed covalent grafting of CMD onto the surface, ensuring stronger stability of the interaction between APTES and CMD, but also preserving the carboxyl groups of CMD, which could be used for immobilization of the target biomolecule.

1.3.1. Fabrication parameter can affect the yield of immobilization protein

Subsequently, the surfaces were treated with NanoCombs preloaded with anti-Her2 affibody (hereafter Her2 NanoCombs), which have been shown to have a high affinity for their target molecule (21). The NanoCombs were modified with desthiobiotin at the 3' end of the backbone. After incubation with a streptavidin conjugated to horseradish peroxidase, a specific substrate was catalyzed by the peroxidase and converted into a luminescent signal (Fig. 2a). Analysis of the luminescence data showed that the preparation of the surface sample affected the yield of immobilization of the selected protein. As shown in Fig. 2b, considering both the processes with and without annealing treatment, the lowest luminescence signal was observed for surfaces obtained by solution-phase deposition of APTES, followed by spin-coating deposition of CMD. A possible explanation for the low yield of protein immobilization resulting from the combination of these two processes lies in the observation that APTES deposited in solution phase leads to a SAM with low homogeneity. This can have a negative impact on the subsequent deposition of CMD, which is more likely to be deposited in a thin layer, as in the spin coating method, than in a thick layer, as in the dip coating method. In addition, for all the conditions tested, we found a positive effect of the annealing treatment performed after the APTES coating. The vacuum thermal process associated with the annealing treatment is able to promote the selective removal of APTES and OTS molecules that are physically but not chemically bound on the surface, which improves the subsequent reproducible deposition of the CMD (30, 31). Moreover, it has been previously demonstrated that thermal treatment at 120 °C is critical to promote covalent binding of APTES molecules to the hydrophilic surface (32). We found that of the 11 different samples analyzed, the surfaces obtained by solution-phase deposition of APTES followed by annealing and dip coating of CMD and vapor-phase deposition of APTES followed by annealing

and spin or dip coating of CMD had the highest luminescence values (Fig. 2b), indicating that the highest degree of protein immobilization was achieved with these preparation methods. Although dip coating is the preferred approach for complex patterns, spin coating resulted in faster and more reliable CMD deposition, including control of the thickness of the deposited layers. For this reason, even though a comparable luminescence signal was obtained for the three SiO₂ surfaces mentioned above, we selected the surface obtained by spin coating for further processing and characterization.

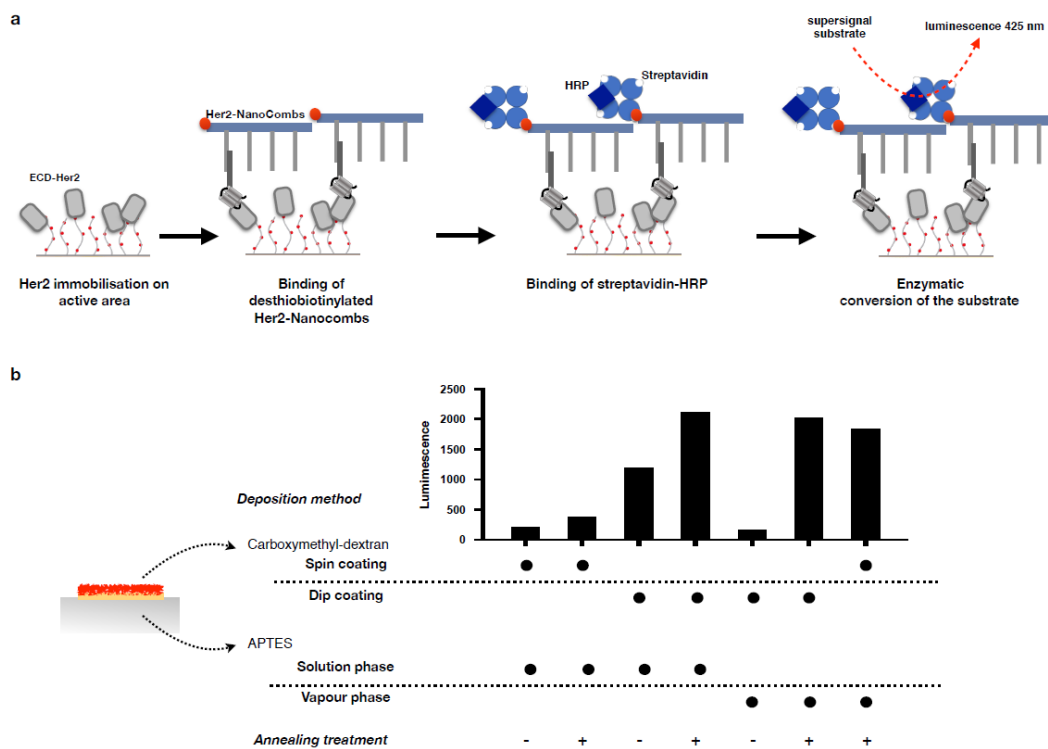


Figure 5: **a**, Schematic of the chemiluminescence assay used to evaluate the yield of protein immobilisation on the SiO₂ surfaces. ECD-Her2 was covalently immobilised on the active area by means of coupling of the amine groups of protein to the carboxylic groups of dextran. Active areas were then treated with DNA nanoassemblies (NanoCombs) preloaded with anti-Her2 affibody (Her2-NanoCombs) and modified with a desthiobiotin. After washing, patterned surfaces were then incubated with streptavidin conjugated with horseradish peroxidase. The enzyme catalyses the substrate conversion, leading to the luminescence emission at 425 nm. **b**, Luminescence values are presented on histogram. Samples differ for fabrication parameters of three steps: deposition of APTES (from vapour phase versus solution phase), annealing treatment after APTES deposition (with versus without) and deposition of carboxymethyl-dextran (by spin coating versus dip coating).

1.3.2. Chemiluminescence assay to validate the signal read-out on CMD patterned SiO₂ surfaces

We treated three independent samples of the selected SiO₂ surfaces with the same amount of Her2 protein. A similar chemiluminescence signal obtained with the DNA nanoassembly-based assay indicated the same yield of protein immobilization and confirmed the reproducibility and stability of the surface functionalization (Fig. 3a). We observed proportionality between the amount of protein used for immobilization and the readout signal, reflecting the yield of immobilization (Fig. 3b). In addition, we found that the readout signal was specific for the immobilized protein (Fig. 3c), indicating that the manufacturing processes used for the deposition of CMD preserved the properties of high chemical specificity and, most importantly, minimal nonspecific binding.

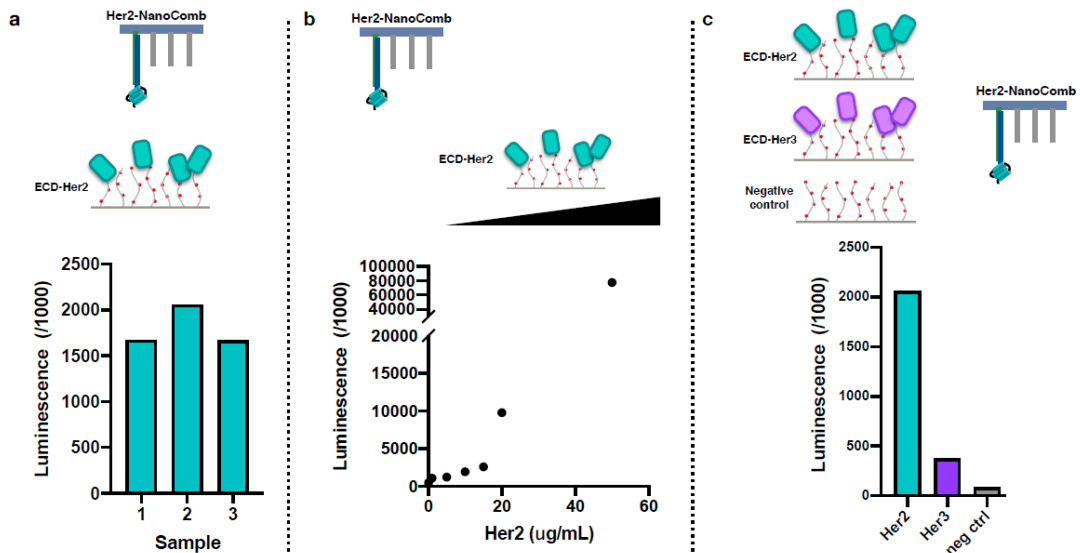


Figure 2: **a**, Evaluation of the reproducibility of protein immobilisation. Three SiO₂ sample surfaces were processed as replicates of the same experiment which entails first the immobilisation of ECD-Her2 on patterned surfaces by means of amine coupling and then tested with chemiluminescence assay to determine the level of protein immobilisation, as previously described. **b**, Evaluation of proportionality between amount of protein used for immobilisation and yield of immobilisation. Different amount of ECD-Her2 (from 1 to 50 µg/mL) were immobilised on different patterned surfaces. Chemiluminescent assay revealed a direct proportionality between protein

concentration used in the immobilisation step and readout signal. *c*, Evaluation of specificity of luminescence readout. Three surfaces presenting ECD-Her2, ECD-Her3 and without any protein as negative control were created. Chemiluminescence signal showed that Her2-NanoComb bound specifically to the surface presenting its target (ECD-Her2) and that there was minimal background binding to the surface that did not present the correct target protein (ECD-Her3) or to the negative control.

1.3.3. Validation of specificity of the luminescence readout on CMD patterned SiO₂ surfaces

To further prove the specificity of the detection performed with our device, in the absence of nonspecific binding of proteins during immobilization and of binder-oligo conjugates during the binding assay, we performed a cross-reactivity assay testing the binding of Her2 and Her3 NanoCombs over SiO₂ surfaces with ECD-Her2 and ECD-Her3. The luminescence signal was observed only when the NanoCombs were incubated over the surfaces presenting their respective target proteins (Fig. 4a). Next, we correlated the SPR signal obtained on the SPR sensor chip with the luminescence readout obtained on our CMD-based arrays (Fig. 4bc). We immobilized two different target proteins (ECD-Her2 and ECD-Her3) on CMD-based SPR sensor chips (CM5 chip) using the same concentrations for the two proteins in the amine coupling reaction. Then, we recorded the binding of the binder-oligo conjugates specific for each of the two proteins by injecting them in saturating concentrations over the SPR sensor surface. We observed different degrees of binding of the binder-oligo conjugates for their respective target proteins (Fig. 4b), This is due to both the different immobilization of the target proteins by amine coupling to the CMD matrix of the SPR sensor chip and to the specific interactions between the binders and the target proteins. In parallel, we performed the same binding assay on our CMD-based patterned surfaces. We immobilized the two target proteins on two distinct active areas of the SiO₂

surface and then we ran the chemiluminescence assay by using NanoCombs functionalized with the binder-oligo conjugates used in the SPR experiment (Her2- and Her3-NanoComb) (Fig. 4c). We found a good correlation between the luminescence signal and the SPR binding level for each binder-oligo/target protein pair. Together, these results show that our CMD -based arrays have protein immobilization capability and detection performance of their respective binders comparable to commercial CMD -based SPR sensor chips.

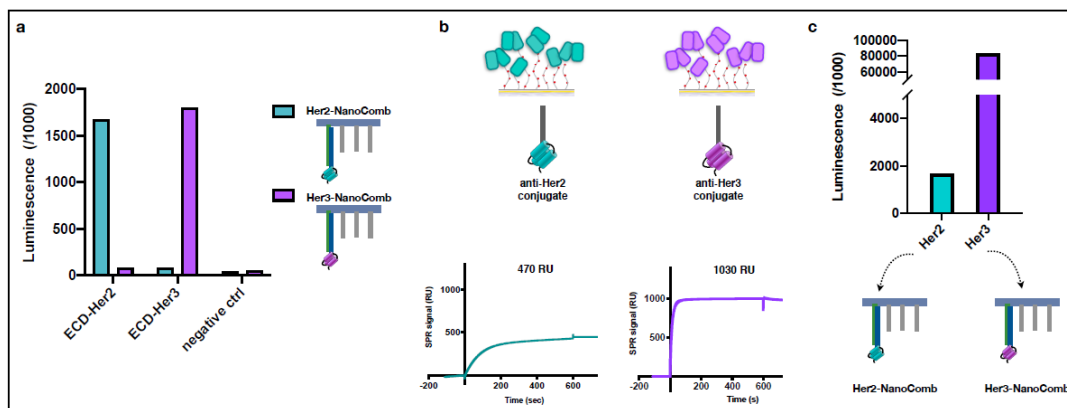


Figure 3: **a**, Cross-reactivity test: patterned SiO₂ surfaces presenting Her2, Her3 (immobilized at a concentration to obtain the same NanoComb binding level, as tested in Fig. S4) and without any protein, as negative control, were treated with Her2- and Her3-NanoCombs. Chemiluminescence assay was performed, and signals obtained from the two different NanoCombs on surfaces functionalized with the same target revealed the absence of cross-reactivity. **b** and **c**, Comparable difference in chemical reactivity of two target proteins towards dextran matrix of patterned surfaces and of model SPR surfaces leads to comparable different yield of immobilisation. **b**, Two different target proteins (Her2 and Her3) were covalently attached to two distinct SPR sensor surfaces, functionalized with a carboxymethyl-dextran matrix. The amount of immobilised protein was estimated from SPR signal of binder-oligo conjugate specific for each protein and injected at 10-fold the KD for their respective target. **c**, Same target proteins (Her2 and Her3) were covalently immobilised on two distinct patterned SiO₂ surfaces at a saturating concentration. NanoCombs specific for each surface were incubated and amount of immobilised protein was verified with the chemiluminescence readout. Difference of luminescence signal among the two target proteins is comparable to that one obtained with SPR sensor surfaces.

1.3.4. Binding assay on patterned surfaces compared to ELISA standard plate-based assay

In addition, we compared biomolecular interaction analyses performed on our CMD -based patterned surfaces with standard, commonly used ELISA plate-based assays (Fig. 5). Our CMD-based chips allow immobilization of a higher amounts of target proteins at lower volumes compared to 96-well plates. Higher detection signals in reduced volumes of the chemiluminescence assay also enable the possibility of future miniaturization of the system.

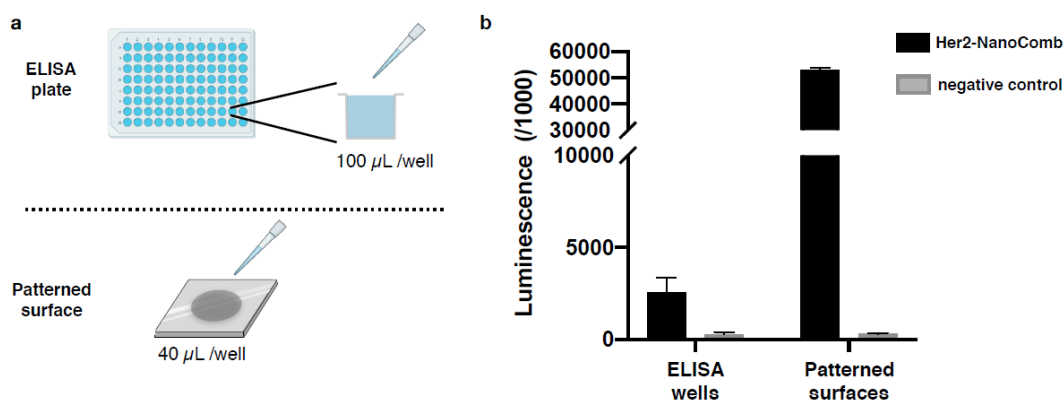


Figure 5: **a**, His-tagged ECD-Her2 was immobilised in parallel on patterned surfaces and on Nickel coated 96-well plate, commonly used for ELISA and other standard plate-based binding assays. **b**, Chemiluminescence assay performed in triplicate on both formats showed that patterned SiO₂ surfaces allow the immobilisation of higher amounts of target protein in lower volume if compared to 96-well plate. Volumes used for target protein immobilisation and subsequent steps of the chemiluminescence assay are reduced in patterned surfaces assay if compared to 96-well plate assay.

1.3.5. Carboxymethyl-dextran functionalization of glass coverslip allows to use fluorescence imaging as readout of binding assays

We used the selected fabrication process developed for the SiO₂ surface to functionalize the cover glass substrate. By repeating the process optimized for SiO₂ samples on a transparent substrate, we aimed to produce surface samples that could be used in microscopy and imaging (Fig. 6). Immobilization of ECD-Her2 as a target protein on glass surfaces was assessed by standard immunoassays (Fig. 6a). In both immunoassays performed, we observed a specific binding of ECD-Her2 through amine coupling chemistry of the immobilization step and we did not detect aspecific binding of nanobodies and antibodies used for fluorescence detection. In addition, we demonstrated that the immobilization/interaction of biomolecules occurred only at the bioactive areas of the surface (Fig. 6b).

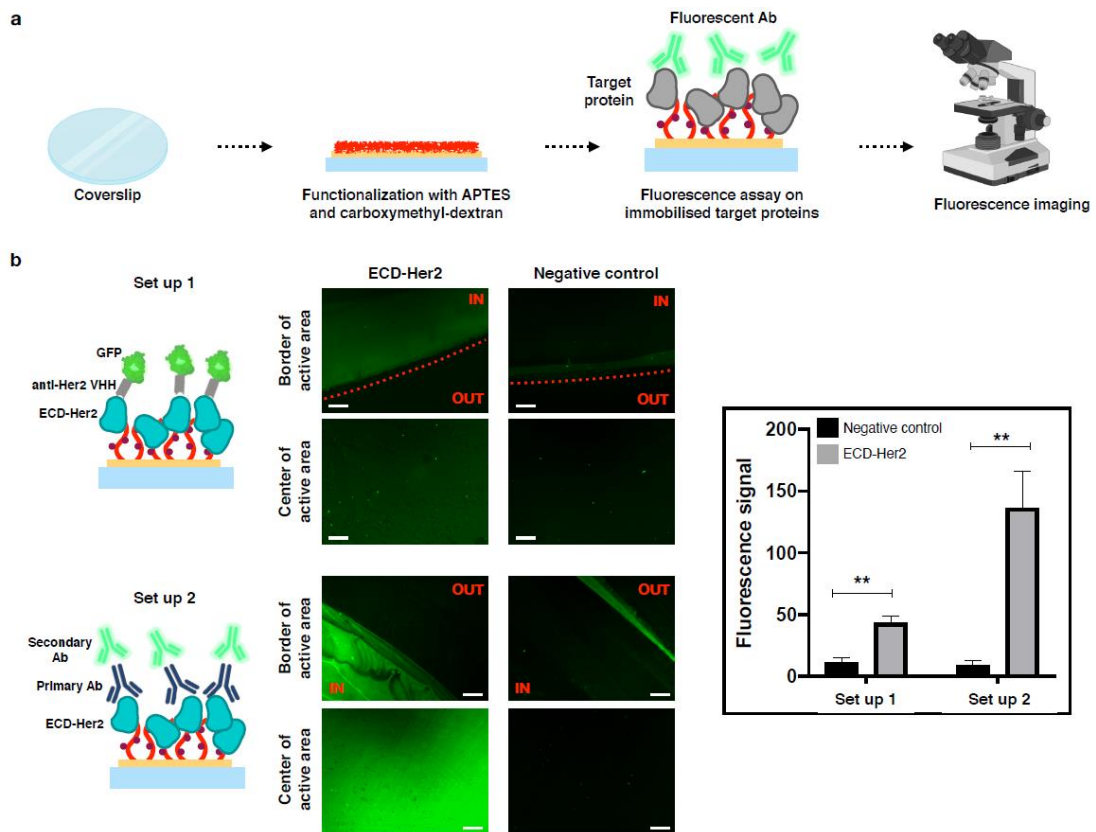
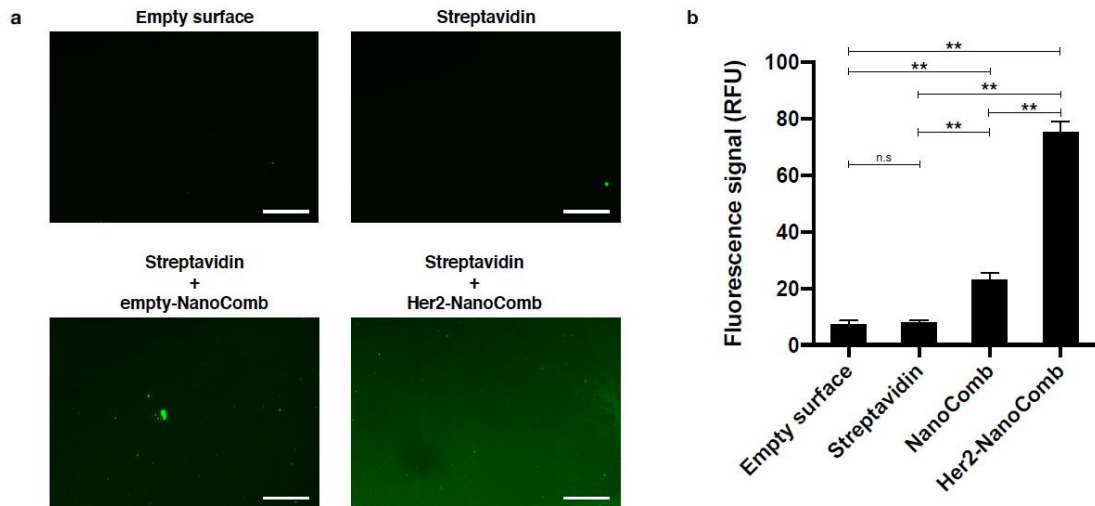


Figure 6: **a**, Schematic representation of fluorescent assay performed on carboxymethyl-dextran functionalized surfaces. ECD-Her2 was immobilised on cover glass, functionalized with CMD, by amine coupling reaction. Then two different fluorescence assays set up were performed and the fluorescence signal was observed on fluorescence microscopy. **b**, In the set up 1 a nanobody (VHH) specific for ECD-Her2 and labelled with GFP was incubated over the surface. In the set up 2 a first incubation with a primary Ab specific for ECD-Her2 was followed by the incubation with secondary Ab labelled with Alexa488 fluorophore. Both in set up1 and 2 the fluorescence signal of was acquired in triplicate with a fluorescence microscope. Quantification of the signal is showed in the histogram. $**P \leq 0.05$. Scale bars: 100 μm .

Finally, we tested the capability of our CMD -based patterned glass surfaces to inversely immobilize Her2-nanoCombs and then perform ECD-Her2 recognition. Again, we observed specific binding between ECD-Her2 and Her2 nanoCombs, as detected by a primary anti-Her2 AB and a secondary fluorescent Ab (Fig. 7), compared with all negative controls (empty surface, immobilized Streptavidin, biotinylated NanoComb that was not functionalized with anti-Her2 affibody).



*Figure 7: Desthiobiotin-Her2-NanoCombs were immobilized on glass CMD-based patterned surfaces through SA molecules previously attached by means of amine coupling. Empty surface, surfaces with immobilized SA and surface with SA with anchored empty-NanoComb were used as negative control. Binding of ECD-Her2 was determined through a primary Ab specific for ECD-Her2 was followed by the incubation with secondary Ab labelled with Alexa488 fluorophore. **a**, Fluorescence images of the four samples. Scale bars: 100 μm . **b**, Quantification of the fluorescence signal, obtained in triplicate, is shown in the histogram. $**P \leq 0.05$.*

2. Conclusions

In this work, we have developed a fabrication process for the patterned functionalization of bioanalytical platforms. We have demonstrated the development of CMD patterned surfaces that combine standard, simple, and inexpensive fabrication techniques.

SiO₂ and glass substrates with limited CMD -based bioactive areas were fabricated and optimized for efficient and specific protein immobilization. We have shown that biomolecular interactions observed with our surfaces correlate with results obtained with CMD -based SPR sensor chips. This enables the transfer of the highest quality data for characterizing biomolecular interactions, such as with the SPR gold standard technique, to simple assays that are feasible on our CMD-based chips. Validation of our surfaces in parallel with SPR assays is advantageous compared to other surface analysis techniques, as we can transfer the information content of an interaction together with highly sensitive and accurate detection results of real-time binding events directly to our CMD -based chip, benefiting from a low-cost, straightforward and higher throughput assay device.

3. Methods

Fabrication of CMD patterned surfaces

Cleaning of the silicon substrates

The silicon wafers were cut into pieces (approximately 3.0 cm x 4.5 cm) and processed with appropriate cleaning and surface activation. The silicon substrates were cleaned by keeping them in a piranha solution (3:1; H₂SO₄/H₂O₂) for 15 min to effectively remove the organic contaminants and promote the formation of the hydroxyl group for the following functionalization step with OTS. The substrates were then carefully rinsed with deionized water (DI) and dried under a nitrogen (N₂) gas stream. After the cleaning step, oxygen plasma treatment was performed by reactive ion etching (RIE) for 2 min (40 W, bias 100 V) to activate the OH group on the surface.

Cleaning of the silicon substrates

Glass substrates (22 mm × 22 mm) were first cleaned in soapy water, rinsed in DI water, and finally immersed in a freshly prepared RCA-1 solution (5:1:1; H₂O/H₂O₂/NH₃) for 20 minutes at 70 °C. Then they were washed with DI water, acetone, and isopropanol (IPA) and dried with N₂ blow. Then, the glass substrates were further cleaned with oxygen plasma treatment by RIE for 2 min (40 W, Bias 100 V) to allow the activation of silanol groups on the surface.

Laser-patterned PDMS mask

The silicone mask with the desired pattern was fabricated directly on a silicone film (ELASTOSIL® Film 2030, 200 µm thickness - Wacker Chemie AG) using a laser cutting technique. We used a commercial CO₂ laser plotter (Versa Laser System, model VLS3.50, Universal Laser System, Ltd.) with the following parameters: maximum power 25 W, maximum pulses per inch (PPI) 1000, and scanning speed from 0.25 to 25 mm/s.

Characterization of CMD-patterned surfaces

Atomic Force Microscopy (AFM)

Surface morphologies and roughness were characterized by AFM imaging with an MFP-3D atomic force microscope (Asylum Research) in tapping mode in air using a silicon cantilever (Mikromasch, NSC19/ AL BS) with a nominal tip radius of ~ 8 nm and spring constants of $k = 0.6$ N/m ($f \approx 65$ kHz). The 512×512 pixel images were acquired in a $5 \mu\text{m} \times 5 \mu\text{m}$ area on the chip surface; two scans were acquired for each surface, each from a separate chip. Gwyddion software was used for quantitative analysis of the AFM images.

Contact angle measurements

Contact angle measurements were performed using a DataPhysics OCA 15Pro optical instrument (DataPhysics Instruments GmbH, Germany) at ambient temperature by adding $2 \mu\text{L}$ of Milli-Q water to the sensor surface. Average CA values were determined by measuring five different positions on each sample surface.

Optical profile images

3D optical profiles were obtained using a Profilm3D optical profilometer (Filmetrics Inc., USA).

Chemiluminescence assay

ECD-Her2 and ECD-Her3 (ACROBiosystems) (Sino Biological) proteins were immobilized on the active areas of our microfabricated SiO_2 CMD -based chip by covalent amine coupling. Briefly, a 10-min incubation of a mixture of 1-ethyl-3-(3-dimethylaminopropyl) carbodiimide hydrochloride (EDC) and N-hydroxysuccinimide (NHS) (Cytiva) was used to activate the carboxyl groups of CMD. The proteins were diluted in Na-acetate buffer pH 4.0 - 4.5 (Cytiva)

and incubated on the activated surfaces for 20 minutes. Finally, the non-reacting carboxyl groups were blocked with a solution of ethanolamine hydrochloride-NaOH pH 8.5 (Cytiva) for 10 minutes. Patterned CMD -based surfaces presenting ECD-Her2 or ECD-Her3 were then treated with Her2 and Her3 NanoCombs modified with desthiobiotin at the 3' end of the backbone for 2 h at room temperature (RT), followed by washing with PBS + 0.05% Tween20. The surfaces were then incubated with streptavidin conjugated to horseradish peroxidase (Thermo Fisher Scientific) for 20 min at RT followed by washing. SuperSignal enzyme-linked immunosorbent assay Pico chemiluminescent substrate (Thermo Fisher Scientific) was added, and substrate conversion catalysed by horseradish peroxidase was performed for 1 min at RT. Luminescence at 425 nm was measured within 5 min of the end of the reaction using a Varioskan Lux plate reader (Thermo Fisher Scientific).

Elisa plate-based chemiluminescent assay

Pierce Nickel Coated Plates (Thermo Fisher Scientific) were used to immobilize His-tagged ECD-Her2 proteins (1 h incubation). After washing with PBS + 0.05% Tween20, the chemiluminescence assay was performed as described above for the CMD-based patterned surfaces.

Fluorescence assay

Two fluorescence assays were performed.

Experimental setup 1: The surfaces were incubated with a camelid nanobody (VHH) specific for ECD-Her2 co-expressed with green fluorescent protein (GFP) (gift from Prof. Ario de Marco - College of Nova Gorica) for 2 hours at RT, followed by washing with PBS + 0.05% Tween20 (FIG6B);
Experimental setup 2: Surfaces were incubated with a primary antibody (Her2 Recombinant Rabbit Monoclonal Antibody - Thermo Fisher Scientific) for 2 hours at RT and, after washing with PBS + 0.05% Tween20, with a secondary

fluorescent antibody (Donkey anti-Rabbit IgG Secondary Antibody, Alexa Fluor 488 - Thermo Fisher Scientific) for 1 hour at RT, followed by washing. For the SA experiment, SA molecules were covalently immobilized by amine coupling as described previously. Desthiobiotin NanoCombs were then incubated for 1 hour at RT above the surface.

The fluorescence signal was acquired using Zeiss Axio Imager. M2 microscope at 10x magnification and quantified using ImageJ. Three different images of the same region of interest (ROI) were included in the analysis.

SPR-assay

ECD-Her2/ECD-Her3 proteins were immobilized on different flow cells of a CM5 sensor chips via amine coupling reactions according to the manufacturer's instructions. Binding assays of anti-Her2 and anti-Her3 binder- oligo conjugates were performed with a saturating concentration of analytes in running buffer (HBS-EP +). A Biacore T200 instrument and related reagents (Cytiva) were used to perform all SPR experiments.

Statistical analysis

Statistical analysis was performed using GraphPad Prism (version 8.2.1). Statistical significance was determined by a two-tailed Student's t test. $P \leq 0.05$ was considered statistically significant.

References

- (1) Ridley, A. J.; Schwartz, M. A.; Burridge, K.; Firtel, R. A.; Ginsberg, M. H.; Borisy, G.; Parsons, J. T.; Horwitz, A. R. Cell Migration: Integrating Signals from Front to Back. *Science* **2003**, *302* (5651), 1704–1709. <https://doi.org/10.1126/science.1092053>.
- (2) Grada, A.; Otero-Vinas, M.; Prieto-Castrillo, F.; Obagi, Z.; Falanga, V. Research Techniques Made Simple: Analysis of Collective Cell Migration Using the Wound Healing Assay. *J. Invest. Dermatol.* **2017**, *137* (2), e11–e16. <https://doi.org/10.1016/j.jid.2016.11.020>.
- (3) Trepat, X.; Chen, Z.; Jacobson, K. Cell Migration. *Compr. Physiol.* **2012**, *2* (4), 2369–2392. <https://doi.org/10.1002/cphy.c110012>.
- (4) Lauffenburger, D. A.; Horwitz, A. F. Cell Migration: A Physically Integrated Molecular Process. *Cell* **1996**, *84* (3), 359–369. [https://doi.org/10.1016/s0092-8674\(00\)81280-5](https://doi.org/10.1016/s0092-8674(00)81280-5).
- (5) Vishwakarma, M.; Spatz, J. P.; Das, T. Mechanobiology of Leader–Follower Dynamics in Epithelial Cell Migration. *Curr. Opin. Cell Biol.* **2020**, *66*, 97–103. <https://doi.org/10.1016/j.ceb.2020.05.007>.
- (6) Barnes, J. M.; Przybyla, L.; Weaver, V. M. Tissue Mechanics Regulate Brain Development, Homeostasis and Disease. *J. Cell Sci.* **2017**, *130* (1), 71–82. <https://doi.org/10.1242/jcs.191742>.
- (7) Hayward, M.-K.; Muncie, J. M.; Weaver, V. M. Tissue Mechanics in Stem Cell Fate, Development, and Cancer. *Dev. Cell* **2021**, *56* (13), 1833–1847. <https://doi.org/10.1016/j.devcel.2021.05.011>.
- (8) Wu, S. K.; Gomez, G. A.; Stehbens, S. J.; Smutny, M. Editorial: Forces in Biology - Cell and Developmental Mechanobiology and Its Implications in Disease. *Front. Cell Dev. Biol.* **2020**, *8*, 598179. <https://doi.org/10.3389/fcell.2020.598179>.
- (9) Butcher, D. T.; Alliston, T.; Weaver, V. M. A Tense Situation: Forcing Tumour Progression. *Nat. Rev. Cancer* **2009**, *9* (2), 108–122. <https://doi.org/10.1038/nrc2544>.
- (10) Kramer, N.; Walzl, A.; Unger, C.; Rosner, M.; Krupitza, G.; Hengstschläger, M.; Dolznig, H. In Vitro Cell Migration and Invasion Assays. *Mutat. Res. Mutat. Res.* **2013**, *752* (1), 10–24. <https://doi.org/10.1016/j.mrrev.2012.08.001>.
- (11) Hanahan, D.; Weinberg, R. A. Hallmarks of Cancer: The Next Generation. *Cell* **2011**, *144* (5), 646–674. <https://doi.org/10.1016/j.cell.2011.02.013>.
- (12) Lintz, M.; Muñoz, A.; Reinhart-King, C. A. The Mechanics of Single Cell and Collective Migration of Tumor Cells. *J. Biomech. Eng.* **2017**, *139* (2). <https://doi.org/10.1115/1.4035121>.

- (13) Friedl, P.; Gilmour, D. Collective Cell Migration in Morphogenesis, Regeneration and Cancer. *Nat. Rev. Mol. Cell Biol.* **2009**, *10* (7), 445–457. <https://doi.org/10.1038/nrm2720>.
- (14) Kraning-Rush, C. M.; Califano, J. P.; Reinhart-King, C. A. Cellular Traction Stresses Increase with Increasing Metastatic Potential. *PLOS ONE* **2012**, *7* (2), e32572. <https://doi.org/10.1371/journal.pone.0032572>.
- (15) Clark, A. G.; Vignjevic, D. M. Modes of Cancer Cell Invasion and the Role of the Microenvironment. *Curr. Opin. Cell Biol.* **2015**, *36*, 13–22. <https://doi.org/10.1016/j.ceb.2015.06.004>.
- (16) Mierke, C. T. The Matrix Environmental and Cell Mechanical Properties Regulate Cell Migration and Contribute to the Invasive Phenotype of Cancer Cells. *Rep. Prog. Phys. Phys. Soc. G. B.* **2019**, *82* (6), 064602. <https://doi.org/10.1088/1361-6633/ab1628>.
- (17) Kumar, S.; Weaver, V. M. Mechanics, Malignancy, and Metastasis: The Force Journey of a Tumor Cell. *Cancer Metastasis Rev.* **2009**, *28* (1–2), 113–127. <https://doi.org/10.1007/s10555-008-9173-4>.
- (18) Yamada, K. M.; Sixt, M. Mechanisms of 3D Cell Migration. *Nat. Rev. Mol. Cell Biol.* **2019**, *20* (12), 738–752. <https://doi.org/10.1038/s41580-019-0172-9>.
- (19) Doyle, A. D.; Petrie, R. J.; Kutys, M. L.; Yamada, K. M. Dimensions in Cell Migration. *Curr. Opin. Cell Biol.* **2013**, *25* (5), 642–649. <https://doi.org/10.1016/j.ceb.2013.06.004>.
- (20) Provenzano, P. P.; Eliceiri, K. W.; Campbell, J. M.; Inman, D. R.; White, J. G.; Keely, P. J. Collagen Reorganization at the Tumor-Stromal Interface Facilitates Local Invasion. *BMC Med.* **2006**, *4* (1), 38. <https://doi.org/10.1186/1741-7015-4-38>.
- (21) Ray, A.; Lee, O.; Win, Z.; Edwards, R. M.; Alford, P. W.; Kim, D.-H.; Provenzano, P. P. Anisotropic Forces from Spatially Constrained Focal Adhesions Mediate Contact Guidance Directed Cell Migration. *Nat. Commun.* **2017**, *8*, 14923. <https://doi.org/10.1038/ncomms14923>.
- (22) Doyle, A. D.; Wang, F. W.; Matsumoto, K.; Yamada, K. M. One-Dimensional Topography Underlies Three-Dimensional Fibrillar Cell Migration. *J. Cell Biol.* **2009**, *184* (4), 481–490. <https://doi.org/10.1083/jcb.200810041>.
- (23) Werner, M.; Petersen, A.; Kurniawan, N. A.; Bouten, C. V. C. Cell-Perceived Substrate Curvature Dynamically Coordinates the Direction, Speed, and Persistence of Stromal Cell Migration. *Adv. Biosyst.* **2019**, *3* (10), 1900080. <https://doi.org/10.1002/adbi.201900080>.
- (24) Wolf, K.; Alexander, S.; Schacht, V.; Coussens, L. M.; von Andrian, U. H.; van Rheenen, J.; Deryugina, E.; Friedl, P. Collagen-Based Cell Migration Models in Vitro and in Vivo. *Semin. Cell Dev. Biol.* **2009**, *20* (8), 931–941. <https://doi.org/10.1016/j.semcdb.2009.08.005>.

- (25) Friedl, P.; Alexander, S. Cancer Invasion and the Microenvironment: Plasticity and Reciprocity. *Cell* **2011**, *147* (5), 992–1009. <https://doi.org/10.1016/j.cell.2011.11.016>.
- (26) Stroka, K. M.; Jiang, H.; Chen, S.-H.; Tong, Z.; Wirtz, D.; Sun, S. X.; Konstantopoulos, K. Water Permeation Drives Tumor Cell Migration in Confined Microenvironments. *Cell* **2014**, *157* (3), 611–623. <https://doi.org/10.1016/j.cell.2014.02.052>.
- (27) Altay, G.; Tosi, S.; García-Díaz, M.; Martínez, E. Imaging the Cell Morphological Response to 3D Topography and Curvature in Engineered Intestinal Tissues. *Front. Bioeng. Biotechnol.* **2020**, *8*.
- (28) Paul, C. D.; Mistrionis, P.; Konstantopoulos, K. Cancer Cell Motility: Lessons from Migration in Confined Spaces. *Nat. Rev. Cancer* **2017**, *17* (2), 131–140. <https://doi.org/10.1038/nrc.2016.123>.
- (29) Fisher, K. E.; Sacharidou, A.; Stratman, A. N.; Mayo, A. M.; Fisher, S. B.; Mahan, R. D.; Davis, M. J.; Davis, G. E. MT1-MMP- and Cdc42-Dependent Signaling Co-Regulate Cell Invasion and Tunnel Formation in 3D Collagen Matrices. *J. Cell Sci.* **2009**, *122* (Pt 24), 4558–4569. <https://doi.org/10.1242/jcs.050724>.
- (30) Pieuchot, L.; Marteau, J.; Guignandon, A.; Dos Santos, T.; Brigaud, I.; Chauvy, P.-F.; Cloatre, T.; Ponche, A.; Petithory, T.; Rougerie, P.; Vassaux, M.; Milan, J.-L.; Tusamda Wakhloo, N.; Spangenberg, A.; Bigerelle, M.; Anselme, K. Curvotaxis Directs Cell Migration through Cell-Scale Curvature Landscapes. *Nat. Commun.* **2018**, *9* (1), 3995. <https://doi.org/10.1038/s41467-018-06494-6>.
- (31) Teixeira, A. I.; Abrams, G. A.; Bertics, P. J.; Murphy, C. J.; Nealey, P. F. Epithelial Contact Guidance on Well-Defined Micro- and Nanostructured Substrates. *J. Cell Sci.* **2003**, *116* (Pt 10), 1881–1892. <https://doi.org/10.1242/jcs.00383>.
- (32) Paul, C. D.; Shea, D. J.; Mahoney, M. R.; Chai, A.; Laney, V.; Hung, W.-C.; Konstantopoulos, K. Interplay of the Physical Microenvironment, Contact Guidance, and Intracellular Signaling in Cell Decision Making. *FASEB J. Off. Publ. Fed. Am. Soc. Exp. Biol.* **2016**, *30* (6), 2161–2170. <https://doi.org/10.1096/fj.201500199R>.
- (33) Ermis, M.; Antmen, E.; Hasirci, V. Micro and Nanofabrication Methods to Control Cell-Substrate Interactions and Cell Behavior: A Review from the Tissue Engineering Perspective. *Bioact. Mater.* **2018**, *3* (3), 355–369. <https://doi.org/10.1016/j.bioactmat.2018.05.005>.
- (34) Park, J. Y.; Lee, D. H.; Lee, E. J.; Lee, S.-H. Study of Cellular Behaviors on Concave and Convex Microstructures Fabricated from Elastic PDMS Membranes. *Lab. Chip* **2009**, *9* (14), 2043–2049. <https://doi.org/10.1039/B820955C>.
- (35) Luciano, M.; Xue, S.-L.; De Vos, W. H.; Redondo-Morata, L.; Surin, M.; Lafont, F.; Hannezo, E.; Gabriele, S. Cell Monolayers Sense Curvature by Exploiting Active Mechanics and Nuclear Mechanoadaptation. *Nat.*

- Phys.* **2021**, *17* (12), 1382–1390. <https://doi.org/10.1038/s41567-021-01374-1>.
- (36) Albrecht-Buehler, G. The Phagokinetic Tracks of 3T3 Cells. *Cell* **1977**, *11* (2), 395–404. [https://doi.org/10.1016/0092-8674\(77\)90057-5](https://doi.org/10.1016/0092-8674(77)90057-5).
- (37) Pijuan, J.; Barceló, C.; Moreno, D. F.; Maiques, O.; Sisó, P.; Marti, R. M.; Macià, A.; Panosa, A. In Vitro Cell Migration, Invasion, and Adhesion Assays: From Cell Imaging to Data Analysis. *Front. Cell Dev. Biol.* **2019**, *7*.
- (38) Isherwood, B.; Timpson, P.; McGhee, E. J.; Anderson, K. I.; Canel, M.; Serrels, A.; Brunton, V. G.; Carragher, N. O. Live Cell in Vitro and in Vivo Imaging Applications: Accelerating Drug Discovery. *Pharmaceutics* **2011**, *3* (2), 141–170. <https://doi.org/10.3390/pharmaceutics3020141>.
- (39) Eccles, S. A.; Box, C.; Court, W. Cell Migration/Invasion Assays and Their Application in Cancer Drug Discovery. In *Biotechnology Annual Review*; Elsevier, 2005; Vol. 11, pp 391–421. [https://doi.org/10.1016/S1387-2656\(05\)11013-8](https://doi.org/10.1016/S1387-2656(05)11013-8).
- (40) Li, Z.; Persson, H.; Adolfsson, K.; Abariute, L.; T. Borgström, M.; Hessman, D.; Åström, K.; Oredsson, S.; N. Prinz, C. Cellular Traction Forces: A Useful Parameter in Cancer Research. *Nanoscale* **2017**, *9* (48), 19039–19044. <https://doi.org/10.1039/C7NR06284B>.
- (41) Polacheck, W. J.; Chen, C. S. Measuring Cell-Generated Forces: A Guide to the Available Tools. *Nat. Methods* **2016**, *13* (5), 415–423. <https://doi.org/10.1038/nmeth.3834>.
- (42) Roca-Cusachs, P.; Conte, V.; Trepát, X. Quantifying Forces in Cell Biology. *Nat. Cell Biol.* **2017**, *19* (7), 742–751. <https://doi.org/10.1038/ncb3564>.
- (43) du Roure, O.; Saez, A.; Buguin, A.; Austin, R. H.; Chavrier, P.; Siberzan, P.; Ladoux, B. Force Mapping in Epithelial Cell Migration. *Proc. Natl. Acad. Sci.* **2005**, *102* (7), 2390–2395. <https://doi.org/10.1073/pnas.0408482102>.
- (44) Ghassemi, S.; Meacci, G.; Liu, S.; Gondarenko, A. A.; Mathur, A.; Roca-Cusachs, P.; Sheetz, M. P.; Hone, J. Cells Test Substrate Rigidity by Local Contractions on Submicrometer Pillars. *Proc. Natl. Acad. Sci. U. S. A.* **2012**, *109* (14), 5328–5333. <https://doi.org/10.1073/pnas.1119886109>.
- (45) Coppola, S.; Schmidt, T.; Ruocco, G.; Antonacci, G. Quantifying Cellular Forces and Biomechanical Properties by Correlative Micropillar Traction Force and Brillouin Microscopy. *Biomed. Opt. Express* **2019**, *10* (5), 2202–2212. <https://doi.org/10.1364/BOE.10.002202>.
- (46) Tan, J. L.; Tien, J.; Pirone, D. M.; Gray, D. S.; Bhadriraju, K.; Chen, C. S. Cells Lying on a Bed of Microneedles: An Approach to Isolate Mechanical Force. *Proc. Natl. Acad. Sci. U. S. A.* **2003**, *100* (4), 1484–1489. <https://doi.org/10.1073/pnas.0235407100>.

- (47) Jurchenko, C.; Salaita, K. S. Lighting Up the Force: Investigating Mechanisms of Mechanotransduction Using Fluorescent Tension Probes. *Mol. Cell. Biol.* **2015**, *35* (15), 2570–2582. <https://doi.org/10.1128/MCB.00195-15>.
- (48) Blakely, B. L.; Dumelin, C. E.; Trappmann, B.; McGregor, L. M.; Choi, C. K.; Anthony, P. C.; Dueterberg, V. K.; Baker, B. M.; Block, S. M.; Liu, D. R.; Chen, C. S. A DNA-Based Molecular Probe for Optically Reporting Cellular Traction Forces. *Nat. Methods* **2014**, *11* (12), 1229–1232. <https://doi.org/10.1038/nmeth.3145>.
- (49) McKeating, K. S.; Aubé, A.; Masson, J.-F. Biosensors and Nanobiosensors for Therapeutic Drug and Response Monitoring. *Analyst* **2016**, *141* (2), 429–449. <https://doi.org/10.1039/C5AN01861G>.
- (50) Cammann, K. Bio-Sensors Based on Ion-Selective Electrodes. *Fresenius Z. Für Anal. Chem.* **1977**, *287* (1), 1–9. <https://doi.org/10.1007/BF00539519>.
- (51) Purohit, B.; Vernekar, P. R.; Shetti, N. P.; Chandra, P. Biosensor Nanoengineering: Design, Operation, and Implementation for Biomolecular Analysis. *Sens. Int.* **2020**, *1*, 100040. <https://doi.org/10.1016/j.sintl.2020.100040>.
- (52) Fracchiolla, N. S.; Artuso, S.; Cortelezzi, A. Biosensors in Clinical Practice: Focus on Oncohematology. *Sensors* **2013**, *13* (5), 6423–6447. <https://doi.org/10.3390/s130506423>.
- (53) Zuber, A. A.; Klantsataya, E.; Bachhuka, A. 3.06 - Biosensing. In *Comprehensive Nanoscience and Nanotechnology (Second Edition)*; Andrews, D. L., Lipson, R. H., Nann, T., Eds.; Academic Press: Oxford, 2019; pp 105–126. <https://doi.org/10.1016/B978-0-12-803581-8.10410-2>.
- (54) Tamayo, J.; Kosaka, P. M.; Ruz, J. J.; Paulo, Á. S.; Calleja, M. Biosensors Based on Nanomechanical Systems. *Chem. Soc. Rev.* **2013**, *42* (3), 1287–1311. <https://doi.org/10.1039/C2CS35293A>.
- (55) Boehr, D. D.; Nussinov, R.; Wright, P. E. The Role of Dynamic Conformational Ensembles in Biomolecular Recognition. *Nat. Chem. Biol.* **2009**, *5* (11), 789–796. <https://doi.org/10.1038/nchembio.232>.
- (56) Syeda, R.; Florendo, M. N.; Cox, C. D.; Kefauver, J. M.; Santos, J. S.; Martinac, B.; Patapoutian, A. Piezo1 Channels Are Inherently Mechanosensitive. *Cell Rep.* **2016**, *17* (7), 1739–1746. <https://doi.org/10.1016/j.celrep.2016.10.033>.
- (57) Ridone, P.; Vassalli, M.; Martinac, B. Piezo1 Mechanosensitive Channels: What Are They and Why Are They Important. *Biophys. Rev.* **2019**, *11* (5), 795–805. <https://doi.org/10.1007/s12551-019-00584-5>.
- (58) Zimmerberg, J.; Kozlov, M. M. How Proteins Produce Cellular Membrane Curvature. *Nat. Rev. Mol. Cell Biol.* **2006**, *7* (1), 9–19. <https://doi.org/10.1038/nrm1784>.
- (59) Baumgart, T.; Capraro, B. R.; Zhu, C.; Das, S. L. Thermodynamics and Mechanics of Membrane Curvature Generation and Sensing by Proteins

- and Lipids. *Annu. Rev. Phys. Chem.* **2011**, *62*, 483–506.
<https://doi.org/10.1146/annurev.physchem.012809.103450>.
- (60) Carrascosa, L. G.; Moreno, M.; Álvarez, M.; Lechuga, L. M. Nanomechanical Biosensors: A New Sensing Tool. *TrAC Trends Anal. Chem.* **2006**, *25* (3), 196–206. <https://doi.org/10.1016/j.trac.2005.09.006>.
- (61) Binnig, null; Quate, null; Gerber, null. Atomic Force Microscope. *Phys. Rev. Lett.* **1986**, *56* (9), 930–933.
<https://doi.org/10.1103/PhysRevLett.56.930>.
- (62) Boisen, A.; Dohn, S.; Keller, S. S.; Schmid, S.; Tenje, M. Cantilever-like Micromechanical Sensors. *Rep. Prog. Phys.* **2011**, *74* (3), 036101.
<https://doi.org/10.1088/0034-4885/74/3/036101>.
- (63) Godin, M.; Tabard-Cossa, V.; Miyahara, Y.; Monga, T.; Williams, P. J.; Beaulieu, L. Y.; Lennox, R. B.; Grutter, P. Cantilever-Based Sensing: The Origin of Surface Stress and Optimization Strategies. *Nanotechnology* **2010**, *21* (7), 075501. <https://doi.org/10.1088/0957-4484/21/7/075501>.
- (64) Chaste, J.; Eichler, A.; Moser, J.; Ceballos, G.; Rurali, R.; Bachtold, A. A Nanomechanical Mass Sensor with Yoctogram Resolution. *Nat. Nanotechnol.* **2012**, *7* (5), 301–304.
<https://doi.org/10.1038/nnano.2012.42>.
- (65) Park, K.; Millet, L. J.; Kim, N.; Li, H.; Jin, X.; Popescu, G.; Aluru, N. R.; Hsia, K. J.; Bashir, R. Measurement of Adherent Cell Mass and Growth. *Proc. Natl. Acad. Sci.* **2010**, *107* (48), 20691–20696.
<https://doi.org/10.1073/pnas.1011365107>.
- (66) Waggoner, P. S.; Craighead, H. G. Micro- and Nanomechanical Sensors for Environmental, Chemical, and Biological Detection. *Lab. Chip* **2007**, *7* (10), 1238–1255. <https://doi.org/10.1039/B707401H>.
- (67) Crone, W. C. A Brief Introduction to MEMS and NEMS. In *Springer Handbook of Experimental Solid Mechanics*; Sharpe, W. N., Ed.; Springer Handbooks; Springer US: Boston, MA, 2008; pp 203–228.
https://doi.org/10.1007/978-0-387-30877-7_9.
- (68) Stupar, P.; Opota, O.; Longo, G.; Prod'hom, G.; Dietler, G.; Greub, G.; Kasas, S. Nanomechanical Sensor Applied to Blood Culture Pellets: A Fast Approach to Determine the Antibiotic Susceptibility against Agents of Bloodstream Infections. *Clin. Microbiol. Infect. Off. Publ. Eur. Soc. Clin. Microbiol. Infect. Dis.* **2017**, *23* (6), 400–405.
<https://doi.org/10.1016/j.cmi.2016.12.028>.
- (69) Longo, G.; Alonso-Sarduy, L.; Rio, L. M.; Bizzini, A.; Trampuz, A.; Notz, J.; Dietler, G.; Kasas, S. Rapid Detection of Bacterial Resistance to Antibiotics Using AFM Cantilevers as Nanomechanical Sensors. *Nat. Nanotechnol.* **2013**, *8* (7), 522–526.
<https://doi.org/10.1038/nnano.2013.120>.

- (70) Calleja, M.; Kosaka, P. M.; Paulo, Á. S.; Tamayo, J. Challenges for Nanomechanical Sensors in Biological Detection. *Nanoscale* **2012**, *4* (16), 4925–4938. <https://doi.org/10.1039/C2NR31102J>.
- (71) Barnes, J. R.; Stephenson, R. J.; Welland, M. E.; Gerber, C.; Gimzewski, J. K. Photothermal Spectroscopy with Femtojoule Sensitivity Using a Micromechanical Device. *Nature* **1994**, *372* (6501), 79–81. <https://doi.org/10.1038/372079a0>.
- (72) Thundat, T.; Warmack, R. J.; Chen, G. Y.; Allison, D. P. Thermal and Ambient-induced Deflections of Scanning Force Microscope Cantilevers. *Appl. Phys. Lett.* **1994**, *64* (21), 2894–2896. <https://doi.org/10.1063/1.111407>.
- (73) Kovacs, G. T. A.; Maluf, N. I.; Petersen, K. E. Bulk Micromachining of Silicon. *Proc. IEEE* **1998**, *86* (8), 1536–1551. <https://doi.org/10.1109/5.704259>.
- (74) Galbraith, C. G.; Sheetz, M. P. A Micromachined Device Provides a New Bend on Fibroblast Traction Forces. *Proc. Natl. Acad. Sci. U. S. A.* **1997**, *94* (17), 9114–9118. <https://doi.org/10.1073/pnas.94.17.9114>.
- (75) Goeders, K. M.; Colton, J. S.; Bottomley, L. A. Microcantilevers: Sensing Chemical Interactions via Mechanical Motion. *Chem. Rev.* **2008**, *108* (2), 522–542. <https://doi.org/10.1021/cr0681041>.
- (76) Mader, A.; Gruber, K.; Castelli, R.; Hermann, B. A.; Seeberger, P. H.; Rädler, J. O.; Leisner, M. Discrimination of Escherichia Coli Strains Using Glycan Cantilever Array Sensors. *Nano Lett.* **2012**, *12* (1), 420–423. <https://doi.org/10.1021/nl203736u>.
- (77) Fritz, J.; Baller, M. K.; Lang, H. P.; Rothuizen, H.; Vettiger, P.; Meyer, E.; Güntherodt, H.; Gerber, C.; Gimzewski, J. K. Translating Biomolecular Recognition into Nanomechanics. *Science* **2000**, *288* (5464), 316–318. <https://doi.org/10.1126/science.288.5464.316>.
- (78) Baller, null; Lang, null; Fritz, null; Gerber, null; Gimzewsk, null; Drechsler, null; Rothuizen, null; Despont, null; Vettiger, null; Battiston, null; Ramseyer, null; Fornaro, null; Meyer, null; Guntherodt, null. A Cantilever Array-Based Artificial Nose. *Ultramicroscopy* **2000**, *82* (1–4), 1–9. [https://doi.org/10.1016/s0304-3991\(99\)00123-0](https://doi.org/10.1016/s0304-3991(99)00123-0).
- (79) Vančura, C.; Dufour, I.; Heinrich, S. M.; Josse, F.; Hierlemann, A. Analysis of Resonating Microcantilevers Operating in a Viscous Liquid Environment. *Sens. Actuators Phys.* **2008**, *141* (1), 43–51. <https://doi.org/10.1016/j.sna.2007.07.010>.
- (80) Ziegler, C. Cantilever-Based Biosensors. *Anal. Bioanal. Chem.* **2004**, *379* (7–8), 946–959. <https://doi.org/10.1007/s00216-004-2694-y>.
- (81) Ramos, D.; Tamayo, J.; Mertens, J.; Calleja, M. Photothermal Excitation of Microcantilevers in Liquids. *J. Appl. Phys.* **2006**, *99* (12), 124904. <https://doi.org/10.1063/1.2205409>.
- (82) Penedo, M.; Yurtsever, A.; Miyazawa, K.; Furusho, H.; Ishii, K.-A.; Fukuma, T. Photothermal Excitation Efficiency Enhancement of

- Cantilevers by Electron Beam Deposition of Amorphous Carbon Thin Films. *Sci. Rep.* **2020**, *10* (1), 17436. <https://doi.org/10.1038/s41598-020-74433-x>.
- (83) Haefliger, D.; Hansen, O.; Boisen, A. Self-Positioning of Polymer Membranes Driven by Thermomechanically Induced Plastic Deformation. *Adv. Mater.* **2006**, *18* (2), 238–241. <https://doi.org/10.1002/adma.200501687>.
- (84) Mertens, J.; Daudén, M. I.; Carrascosa, J. L.; Tamayo, J. Stepwise Motion of a Microcantilever Driven by the Hydrolysis of Viral ATPases. *Nanotechnology* **2011**, *23* (1), 015501. <https://doi.org/10.1088/0957-4484/23/1/015501>.
- (85) Etayash, H.; Jiang, K.; Azmi, S.; Thundat, T.; Kaur, K. Real-Time Detection of Breast Cancer Cells Using Peptide-Functionalized Microcantilever Arrays. *Sci. Rep.* **2015**, *5* (1), 13967. <https://doi.org/10.1038/srep13967>.
- (86) *A perspective view on the nanomotion detection of living organisms and its features - Venturelli - 2020 - Journal of Molecular Recognition - Wiley Online Library.* <https://onlinelibrary.wiley.com/doi/10.1002/jmr.2849> (accessed 2021-10-24).
- (87) Friedrichs, J.; Helenius, J.; Muller, D. J. Quantifying Cellular Adhesion to Extracellular Matrix Components by Single-Cell Force Spectroscopy. *Nat. Protoc.* **2010**, *5* (7), 1353–1361. <https://doi.org/10.1038/nprot.2010.89>.
- (88) Kohler, A.-C.; Venturelli, L.; Kannan, A.; Sanglard, D.; Dietler, G.; Willaert, R.; Kasas, S. Yeast Nanometric Scale Oscillations Highlights Fibronectin Induced Changes in *C. Albicans*. *Fermentation* **2020**, *6* (1), 28. <https://doi.org/10.3390/fermentation6010028>.
- (89) Patil, S. B.; Al-Jehani, R. M.; Etayash, H.; Turbe, V.; Jiang, K.; Bailey, J.; Al-Akkad, W.; Soudy, R.; Kaur, K.; McKendry, R. A.; Thundat, T.; Ndieyira, J. W. Modified Cantilever Arrays Improve Sensitivity and Reproducibility of Nanomechanical Sensing in Living Cells. *Commun. Biol.* **2018**, *1* (1), 175. <https://doi.org/10.1038/s42003-018-0179-3>.
- (90) Sader, J. E. Frequency Response of Cantilever Beams Immersed in Viscous Fluids with Applications to the Atomic Force Microscope. *J. Appl. Phys.* **1998**, *84* (1), 64–76. <https://doi.org/10.1063/1.368002>.
- (91) Berger, R.; Delamarche, E.; Lang, H. P.; Gerber, C.; Gimzewski, J. K.; Meyer, E.; Güntherodt, H.-J. Surface Stress in the Self-Assembly of Alkanethiols on Gold. *Science* **1997**, *276* (5321), 2021–2024. <https://doi.org/10.1126/science.276.5321.2021>.
- (92) Ilic, B.; Czaplewski, D.; Zalalutdinov, M.; Craighead, H. G.; Neuzil, P.; Campagnolo, C.; Batt, C. Single Cell Detection with Micromechanical Oscillators. *J. Vac. Sci. Technol. B Microelectron. Nanometer Struct. Process. Meas. Phenom.* **2001**, *19* (6), 2825–2828. <https://doi.org/10.1116/1.1421572>.

- (93) Gupta, A.; Akin, D.; Bashir, R. Single Virus Particle Mass Detection Using Microresonators with Nanoscale Thickness. *Appl. Phys. Lett.* **2004**, *84* (11), 1976–1978. <https://doi.org/10.1063/1.1667011>.
- (94) Gfeller, K. Y.; Nugaeva, N.; Hegner, M. Micromechanical Oscillators as Rapid Biosensor for the Detection of Active Growth of Escherichia Coli. *Biosens. Bioelectron.* **2005**, *21* (3), 528–533. <https://doi.org/10.1016/j.bios.2004.11.018>.
- (95) Park, K.; Jang, J.; Irimia, D.; Sturgis, J.; Lee, J.; Robinson, J. P.; Toner, M.; Bashir, R. ‘Living Cantilever Arrays’ for Characterization of Mass of Single Live Cells in Fluids. *Lab. Chip* **2008**, *8* (7), 1034–1041. <https://doi.org/10.1039/B803601B>.
- (96) Martínez-Martín, D.; Fläschner, G.; Gaub, B.; Martin, S.; Newton, R.; Beerli, C.; Mercer, J.; Gerber, C.; Müller, D. J. Inertial Picobalance Reveals Fast Mass Fluctuations in Mammalian Cells. *Nature* **2017**, *550* (7677), 500–505. <https://doi.org/10.1038/nature24288>.
- (97) Lissandrello, C.; Inci, F.; Francom, M.; Paul, M. R.; Demirci, U.; Ekinici, K. L. Nanomechanical Motion of Escherichia Coli Adhered to a Surface. *Appl. Phys. Lett.* **2014**, *105* (11), 113701. <https://doi.org/10.1063/1.4895132>.
- (98) Pelling, A. E.; Sehati, S.; Gralla, E. B.; Valentine, J. S.; Gimzewski, J. K. Local Nanomechanical Motion of the Cell Wall of Saccharomyces Cerevisiae. *Science* **2004**, *305* (5687), 1147–1150. <https://doi.org/10.1126/science.1097640>.
- (99) Kasas, S.; Ruggeri, F. S.; Benadiba, C.; Maillard, C.; Stupar, P.; Tournu, H.; Dietler, G.; Longo, G. Detecting Nanoscale Vibrations as Signature of Life. *Proc. Natl. Acad. Sci. U. S. A.* **2015**, *112* (2), 378–381. <https://doi.org/10.1073/pnas.1415348112>.
- (100) Kohler, A. C.; Venturelli, L.; Longo, G.; Dietler, G.; Kasas, S. Nanomotion Detection Based on Atomic Force Microscopy Cantilevers. *Cell Surf.* **2019**, *5*, 100021. <https://doi.org/10.1016/j.tcs.2019.100021>.
- (101) Melli, M.; Scoles, G.; Lazzarino, M. Fast Detection of Biomolecules in Diffusion-Limited Regime Using Micromechanical Pillars. *ACS Nano* **2011**, *5* (10), 7928–7935. <https://doi.org/10.1021/nn202224g>.
- (102) Burg, T. P.; Godin, M.; Knudsen, S. M.; Shen, W.; Carlson, G.; Foster, J. S.; Babcock, K.; Manalis, S. R. Weighing of Biomolecules, Single Cells and Single Nanoparticles in Fluid. *Nature* **2007**, *446* (7139), 1066–1069. <https://doi.org/10.1038/nature05741>.
- (103) Linden, J.; Oesterschulze, E. Improving the Quality Factor of Cantilevers in Viscous Fluids by the Adaptation of Their Interface. *Appl. Phys. Lett.* **2012**, *100* (11), 113511. <https://doi.org/10.1063/1.3694264>.
- (104) Peiker, P.; Klingel, S.; Menges, J.; Bart, H.-J.; Oesterschulze, E. A Partially Wettable Micromechanical Resonator for Chemical- and Biosensing in Solution. *Procedia Eng.* **2016**, *168*, 606–609. <https://doi.org/10.1016/j.proeng.2016.11.225>.

- (105) Oesterschulze, E.; Kehrbusch, P.; Radzio, B.; Ilin, E. A.; Thyssen, A.; Deitmer, J. W.; Kehrbusch, J. Tailoring the Interface of Hybrid Microresonators in Viscid Fluids Enhances Their Quality Factor by Two Orders of Magnitude. *Lab. Chip* **2012**, *12* (7), 1316–1319. <https://doi.org/10.1039/C2LC21260A>.
- (106) Peiker, P.; Oesterschulze, E. Geometrically Tuned Wettability of Dynamic Micromechanical Sensors for an Improved In-Liquid Operation. *Appl. Phys. Lett.* **2015**, *107* (10), 101903. <https://doi.org/10.1063/1.4930173>.
- (107) Rajagopalan, J.; Saif, M. T. A. MEMS Sensors and Microsystems for Cell Mechanobiology. *J. Micromechanics Microengineering* **2011**, *21* (5), 054002. <https://doi.org/10.1088/0960-1317/21/5/054002>.
- (108) NATARAJAN, A.; CHUN, C.; HICKMAN, J. J.; MOLNAR, P. Growth and Electrophysiological Properties of Rat Embryonic Cardiomyocytes on Hydroxyl- and Carboxyl-Modified Surfaces. *J. Biomater. Sci. Polym. Ed.* **2008**, *19* (10), 1319–1331. <https://doi.org/10.1163/156856208786052399>.
- (109) Ferrell, N.; Woodard, J.; Hansford, D. J. Measurement of Cell Forces Using a Microfabricated Polymer Cantilever Sensor. *Sens. Actuators Phys.* **2011**, *170* (1), 84–89. <https://doi.org/10.1016/j.sna.2011.06.010>.
- (110) Sumbul, F.; Hassanpour, N.; Rodriguez-Ramos, J.; Rico, F. One-Step Calibration of AFM in Liquid. *Front. Phys.* **2020**, *8*.
- (111) Higgins, M. J.; Proksch, R.; Sader, J. E.; Polcik, M.; Mc Endoo, S.; Cleveland, J. P.; Jarvis, S. P. Noninvasive Determination of Optical Lever Sensitivity in Atomic Force Microscopy. *Rev. Sci. Instrum.* **2006**, *77* (1), 013701. <https://doi.org/10.1063/1.2162455>.
- (112) Migliorini, E.; Weidenhaupt, M.; Picart, C. Practical Guide to Characterize Biomolecule Adsorption on Solid Surfaces (Review). *Biointerphases* **2018**, *13* (6), 06D303. <https://doi.org/10.1116/1.5045122>.
- (113) Guha Thakurta, S.; Subramanian, A. Fabrication of Dense, Uniform Aminosilane Monolayers: A Platform for Protein or Ligand Immobilization. *Colloids Surf. Physicochem. Eng. Asp.* **2012**, *414*, 384–392. <https://doi.org/10.1016/j.colsurfa.2012.08.049>.
- (114) Vashist, S. K.; Lam, E.; Hrapovic, S.; Male, K. B.; Luong, J. H. T. Immobilization of Antibodies and Enzymes on 3-Aminopropyltriethoxysilane-Functionalized Bioanalytical Platforms for Biosensors and Diagnostics. *Chem. Rev.* **2014**, *114* (21), 11083–11130. <https://doi.org/10.1021/cr5000943>.
- (115) Saengdee, P.; Promptmas, C.; Thanapitak, S.; Srisuwan, A.; Pankiew, A.; Thornyanadacha, N.; Chairiratanakul, W.; Chaowicharat, E.; Jeamsaksiri, W. Optimization of 3-Aminopropyltriethoxysilane Functionalization on Silicon Nitride Surface for Biomolecule Immobilization. *Talanta* **2020**, *207*, 120305. <https://doi.org/10.1016/j.talanta.2019.120305>.

- (116) Siqueira Petri, D. F.; Wenz, G.; Schunk, P.; Schimmel, T. An Improved Method for the Assembly of Amino-Terminated Monolayers on SiO₂ and the Vapor Deposition of Gold Layers. *Langmuir* **1999**, *15* (13), 4520–4523. <https://doi.org/10.1021/la981379u>.
- (117) Howarter, J. A.; Youngblood, J. P. Optimization of Silica Silanization by 3-Aminopropyltriethoxysilane. *Langmuir* **2006**, *22* (26), 11142–11147. <https://doi.org/10.1021/la061240g>.
- (118) Antoniou, M.; Tsounidi, D.; Petrou, P. S.; Beltsios, K. G.; Kakabakos, S. E. Functionalization of Silicon Dioxide and Silicon Nitride Surfaces with Aminosilanes for Optical Biosensing Applications. *Med. DEVICES Sens.* **2020**, *3* (5), e10072. <https://doi.org/10.1002/mds3.10072>.
- (119) Diao, J.; Ren, D.; Engstrom, J. R.; Lee, K. H. A Surface Modification Strategy on Silicon Nitride for Developing Biosensors. *Anal. Biochem.* **2005**, *343* (2), 322–328. <https://doi.org/10.1016/j.ab.2005.05.010>.
- (120) Rupp, F.; Scheideler, L.; Rehbein, D.; Axmann, D.; Geis-Gerstorfer, J. Roughness Induced Dynamic Changes of Wettability of Acid Etched Titanium Implant Modifications. *Biomaterials* **2004**, *25* (7–8), 1429–1438. <https://doi.org/10.1016/j.biomaterials.2003.08.015>.
- (121) Dohn, S.; Svendsen, W.; Boisen, A.; Hansen, O. Mass and Position Determination of Attached Particles on Cantilever Based Mass Sensors. *Rev. Sci. Instrum.* **2007**, *78* (10), 103303. <https://doi.org/10.1063/1.2804074>.
- (122) Johnson, B. N.; Mutharasan, R. Biosensing Using Dynamic-Mode Cantilever Sensors: A Review. *Biosens. Bioelectron.* **2012**, *32* (1), 1–18. <https://doi.org/10.1016/j.bios.2011.10.054>.
- (123) Łabędź, B.; Wańczyk, A.; Rajfur, Z. Precise Mass Determination of Single Cell with Cantilever-Based Microbiosensor System. *PLoS ONE* **2017**, *12* (11), e0188388. <https://doi.org/10.1371/journal.pone.0188388>.
- (124) Chien, C.-C.; Jiang, J.; Gong, B.; Li, T.; Gaitas, A. AFM Microfluidic Cantilevers as Weight Sensors for Single Cell Mass Measurements. *bioRxiv* February 21, 2022, p 2022.02.21.481347. <https://doi.org/10.1101/2022.02.21.481347>.
- (125) Wu, X.-X.; Yue, G. G.-L.; Dong, J.-R.; Lam, C. W.-K.; Wong, C.-K.; Qiu, M.-H.; Lau, C. B.-S. Actein Inhibits the Proliferation and Adhesion of Human Breast Cancer Cells and Suppresses Migration in Vivo. *Front. Pharmacol.* **2018**, *9*.
- (126) Xie, L.; Sun, Z.; Hong, Z.; Brown, N. J.; Glinskii, O. V.; Rittenhouse-Olson, K.; Meininger, G. A.; Glinsky, V. V. Temporal and Molecular Dynamics of Human Metastatic Breast Carcinoma Cell Adhesive Interactions with Human Bone Marrow Endothelium Analyzed by Single-Cell Force Spectroscopy. *PLOS ONE* **2018**, *13* (9), e0204418. <https://doi.org/10.1371/journal.pone.0204418>.
- (127) Chaudhuri, P. K.; Pan, C. Q.; Low, B. C.; Lim, C. T. Topography Induces Differential Sensitivity on Cancer Cell Proliferation via Rho-

- ROCK-Myosin Contractility. *Sci. Rep.* **2016**, *6* (1), 19672. <https://doi.org/10.1038/srep19672>.
- (128) Balzer, E. M.; Tong, Z.; Paul, C. D.; Hung, W.-C.; Stroka, K. M.; Boggs, A. E.; Martin, S. S.; Konstantopoulos, K. Physical Confinement Alters Tumor Cell Adhesion and Migration Phenotypes. *FASEB J.* **2012**, *26* (10), 4045–4056. <https://doi.org/10.1096/fj.12-211441>.
- (129) Holle, A. W.; Govindan Kutty Devi, N.; Clar, K.; Fan, A.; Saif, T.; Kemkemer, R.; Spatz, J. P. Cancer Cells Invade Confined Microchannels via a Self-Directed Mesenchymal-to-Amoeboid Transition. *Nano Lett.* **2019**, *19* (4), 2280–2290. <https://doi.org/10.1021/acs.nanolett.8b04720>.
- (130) Wolf, K.; Mazo, I.; Leung, H.; Engelke, K.; von Andrian, U. H.; Deryugina, E. I.; Strongin, A. Y.; Bröcker, E.-B.; Friedl, P. Compensation Mechanism in Tumor Cell Migration : Mesenchymal–Amoeboid Transition after Blocking of Pericellular Proteolysis. *J. Cell Biol.* **2003**, *160* (2), 267–277. <https://doi.org/10.1083/jcb.200209006>.
- (131) Yaginuma, T.; Kushiro, K.; Takai, M. Unique Cancer Migratory Behaviors in Confined Spaces of Microgroove Topography with Acute Wall Angles. *Sci. Rep.* **2020**, *10* (1), 6110. <https://doi.org/10.1038/s41598-020-62988-8>.
- (132) Ansardamavandi, A.; Tafazzoli-Shadpour, M.; Shokrgozar, M. A. Behavioral Remodeling of Normal and Cancerous Epithelial Cell Lines with Differing Invasion Potential Induced by Substrate Elastic Modulus. *Cell Adhes. Migr.* **2018**, *12* (5), 472–488. <https://doi.org/10.1080/19336918.2018.1475803>.
- (133) Kushiro, K.; Yaginuma, T.; Ryo, A.; Takai, M. Differences in Three-Dimensional Geometric Recognition by Non-Cancerous and Cancerous Epithelial Cells on Microgroove-Based Topography. *Sci. Rep.* **2017**, *7* (1), 4244. <https://doi.org/10.1038/s41598-017-03779-6>.
- (134) Park, J.; Kim, D.-H.; Kim, H.-N.; Wang, C. J.; Kwak, M. K.; Hur, E.; Suh, K.-Y.; An, S. S.; Levchenko, A. Directed Migration of Cancer Cells Guided by the Graded Texture of the Underlying Matrix. *Nat. Mater.* **2016**, *15* (7), 792–801. <https://doi.org/10.1038/nmat4586>.
- (135) Malandrino, A.; Mak, M.; Kamm, R. D.; Moeendarbary, E. Complex Mechanics of the Heterogeneous Extracellular Matrix in Cancer. *Extreme Mech. Lett.* **2018**, *21*, 25–34. <https://doi.org/10.1016/j.eml.2018.02.003>.
- (136) Papalazarou, V.; Salmeron-Sanchez, M.; Machesky, L. M. Tissue Engineering the Cancer Microenvironment-Challenges and Opportunities. *Biophys. Rev.* **2018**, *10* (6), 1695–1711. <https://doi.org/10.1007/s12551-018-0466-8>.
- (137) Franchi, M.; Piperigkou, Z.; Karamanos, K.-A.; Franchi, L.; Masola, V. Extracellular Matrix-Mediated Breast Cancer Cells Morphological Alterations, Invasiveness, and Microvesicles/Exosomes Release. *Cells* **2020**, *9* (9), 2031. <https://doi.org/10.3390/cells9092031>.

- (138) Wang, J.; Petefish, J. W.; Hillier, A. C.; Schneider, I. C. Epitaxially Grown Collagen Fibrils Reveal Diversity in Contact Guidance Behavior among Cancer Cells. *Langmuir* **2015**, *31* (1), 307–314. <https://doi.org/10.1021/la503254x>.
- (139) Hussey, G. S.; Dziki, J. L.; Badylak, S. F. Extracellular Matrix-Based Materials for Regenerative Medicine. *Nat. Rev. Mater.* **2018**, *3* (7), 159–173. <https://doi.org/10.1038/s41578-018-0023-x>.
- (140) Damborský, P.; Švitel, J.; Katrlík, J. Optical Biosensors. *Essays Biochem.* **2016**, *60* (1), 91–100. <https://doi.org/10.1042/EBC20150010>.
- (141) Morsbach, S.; Gonella, G.; Mailänder, V.; Wegner, S.; Wu, S.; Weidner, T.; Berger, R.; Koynov, K.; Vollmer, D.; Encinas, N.; Kuan, S. L.; Berau, T.; Kremer, K.; Weil, T.; Bonn, M.; Butt, H.-J.; Landfester, K. Engineering Proteins at Interfaces: From Complementary Characterization to Material Surfaces with Designed Functions. *Angew. Chem. Int. Ed.* **2018**, *57* (39), 12626–12648. <https://doi.org/10.1002/anie.201712448>.
- (142) Biacore3000-Sensorsurface.Pdf.
- (143) Mai-Ngam, K.; Kiatpathomchai, W.; Arunrut, N.; Sansatsadeekul, J. Molecular Self Assembly of Mixed Comb-like Dextran Surfactant Polymers for SPR Virus Detection. *Carbohydr. Polym.* **2014**, *112*, 440–447. <https://doi.org/10.1016/j.carbpol.2014.06.022>.
- (144) Tavakoli, J.; Tang, Y. Hydrogel Based Sensors for Biomedical Applications: An Updated Review. *Polymers* **2017**, *9* (8), 364. <https://doi.org/10.3390/polym9080364>.
- (145) Homola, J. Surface Plasmon Resonance Sensors for Detection of Chemical and Biological Species. *Chem. Rev.* **2008**, *108* (2), 462–493. <https://doi.org/10.1021/cr068107d>.
- (146) Saftics, A.; Türk, B.; Sulyok, A.; Nagy, N.; Agócs, E.; Kalas, B.; Petrik, P.; Fried, M.; Khánh, N. Q.; Prósz, A.; Kamarás, K.; Szekacs, I.; Horvath, R.; Kurunczi, S. Dextran-Based Hydrogel Layers for Biosensors. In *Nanobiomaterial Engineering: Concepts and Their Applications in Biomedicine and Diagnostics*; Chandra, P., Prakash, R., Eds.; Springer: Singapore, 2020; pp 139–164. https://doi.org/10.1007/978-981-32-9840-8_8.
- (147) Miksa, D.; Irish, E. R.; Chen, D.; Composto, R. J.; Eckmann, D. M. Dextran Functionalized Surfaces via Reductive Amination: Morphology, Wetting, and Adhesion. *Biomacromolecules* **2006**, *7* (2), 557–564. <https://doi.org/10.1021/bm050601o>.
- (148) Smith, R. K.; Lewis, P. A.; Weiss, P. S. Patterning Self-Assembled Monolayers. *Prog. Surf. Sci.* **2004**, *75* (1), 1–68. <https://doi.org/10.1016/j.progsurf.2003.12.001>.
- (149) Horvath, R.; Cottier, K.; Pedersen, H. C.; Ramsden, J. J. Multidepth Screening of Living Cells Using Optical Waveguides. *Biosens.*

- Bioelectron.* **2008**, *24* (4), 805–810.
<https://doi.org/10.1016/j.bios.2008.06.059>.
- (150) Chen, S.; Liu, L.; Zhou, J.; Jiang, S. Controlling Antibody Orientation on Charged Self-Assembled Monolayers. *Langmuir* **2003**, *19* (7), 2859–2864. <https://doi.org/10.1021/la026498v>.
- (151) Ambrosetti, E.; Bernardinelli, G.; Hoffecker, I.; Hartmanis, L.; Kiriako, G.; de Marco, A.; Sandberg, R.; Högberg, B.; Teixeira, A. I. A DNA-Nanoassembly-Based Approach to Map Membrane Protein Nanoenvironments. *Nat. Nanotechnol.* **2021**, *16* (1), 85–95.
<https://doi.org/10.1038/s41565-020-00785-0>.
- (152) Peppas, N. A.; Van Blarcom, D. S. Hydrogel-Based Biosensors and Sensing Devices for Drug Delivery. *J. Control. Release Off. J. Control. Release Soc.* **2016**, *240*, 142–150.
<https://doi.org/10.1016/j.jconrel.2015.11.022>.

Ringraziamenti

Innanzitutto, vorrei ringraziare il mio supervisor, *Marco Lazzarino*, per avermi dato l'opportunità di fare questa bellissima esperienza, tra le più formative e stimolanti che abbia fatto finora. Grazie per avermi lasciato libera di fare, provare, e sbagliare. Grazie per le stimolanti chiacchierate, per le critiche sempre costruttive, e per i consigli.

Grazie alla mia tutor, *Laura Andolfi*. Grazie per tutto quello che mi hai insegnato, di professionale e non solo. Grazie per avermi aiutata a trovare un metodo per impostare il mio lavoro in questi anni. Grazie per tutte le volte che mi hai supportata, infondendomi coraggio e fiducia. Grazie per esserti fidata di me e avermi lasciato libera di sperimentare. Grazie perché mi hai accompagnata per mano in questo percorso, e non mi sono mai sentita sola. Grazie soprattutto per la passione e la dedizione che metti in tutto quello che fai. Grazie per la cura che hai per le cose e per le persone. Grazie per il tuo tempo e per il tuo sorriso sempre speranzoso. È stato un piacere imparare da te e lavorare con te.

Grazie al mio tutor, *Simone Dal Zilio*. Grazie per avermi guidata in un mondo per me totalmente sconosciuto, quello dei materiali. Grazie per avermi lasciata libera di provare e per aver creduto in me, sempre. Ma soprattutto, grazie per l'immensa passione che metti nel tuo lavoro. È stato un piacere lavorare con te, sperimentare assieme nuove cose, mettere assieme idee, trasformarle in progetti e realizzarli. Grazie per tutte le volte che mi hai messa di buon umore con i tuoi fischiattii di canzoni natalizie (anche in piena estate). Grazie per il tuo tempo, la tua dedizione, la tua pazienza.

Grazie a *Michele e Mauro*, che in questi anni sono sempre stati Casa qui a Trieste. Grazie per il vostro supporto, la vostra allegria, per esserci stati in tutte le occasioni. Grazie per avermi insegnato che l'Amore è Amore e basta.

Grazie a *Jonny e Madda* che ho incontrato in questa città e che sono state uno dei regali più belli che Trieste mi abbia fatto. Siete state un punto di riferimento in questi anni e un porto di comprensione, gioia e fanciullezza, nel quale amo approdare per ritrovare sempre serenità.

Grazie a tutti i colleghi con cui ho condiviso questo percorso, in particolare *Erik, Michele, Marco, Alice, Nicola, Alessia M., Alessia (Mezza), Nicoletta, Beatrice*.

Grazie ad altri colleghi e amici che in questi anni mi hanno supportata e incoraggiata, e con i quali ho vissuto momenti felici, in particolare *Federica V., Sara L., Enrico L., e Dario C.*

Grazie ad *Anna e Francesca*, che sono la dimostrazione che non c'è distanza che possa separare i sentimenti veri. Grazie alle mie amiche che sono sempre lì ad aspettarmi ogni volta che ritorno in terra natia.

Grazie a *Chiara*, che mi ha aiutata a ritrovare me stessa e adesso so che non sarò mai sola.

Grazie ai miei fratelli, *Corrado e Giuseppe*, coi quali ho un rapporto meraviglioso e che sono le persone che amo di più al mondo.

Grazie alle mie nonne, che mi ricordano ogni giorno quanto faticoso sia stato nascere donna. Lotterò per dimostrare che una donna può essere felice solo se ha la possibilità di esprimere al meglio sé stessa e le sue potenzialità. Terrò sempre con me la vostra forza, il vostro coraggio, la voglia immensa di vivere, e tutto l'Amore che mi avete donato.

Grazie a mamma e papà, per avermi sempre supportata, per essere sempre un porto sicuro. E grazie per avermi insegnato ad Amare.